DISSERTATION

REFLECTIVITY RETRIEVAL IN A NETWORKED RADAR ENVIRONMENT

Submitted by

Sanghun Lim

Department of Electrical and Computer Engineering

In partial fulfillment of the requirements

For the Degree of Doctor of Philosophy

Colorado State University

Fort Collins, Colorado

Summer 2006

COLORADO STATE UNIVERSITY

February 15, 2006

WE HEREBY RECOMMEND THAT THE DISSERTATION PREPARED UNDER OUR SUPERVISION BY SANGHUN LIM ENTITLED REFLECTIVITY RETRIEVAL IN A NETWORKED RADAR ENVIRONMENT BE ACCEPTED AS FULFILLING IN PART REQUIREMENTS FOR THE DEGREE OF DOCTOR OF PHILOSOPHY.

Committee on Graduate Work

V.N. Bringi

Anura P. Jayasumana

P.W. Mielke (Statistics)

Adviser: V. Chandrasekar

Department Head

ABSTRACT OF DISSERTATION

REFLECTIVITY RETRIEVAL IN A NETWORKED RADAR ENVIRONMENT

Monitoring of precipitation using a high-frequency radar system such as X-band is becoming increasingly popular due to its lower cost compared to its counterpart at S-band. Networks of meteorological radar systems at higher frequencies are being pursued for targeted applications such as coverage over a city or a small basin. However, at higher frequencies, the impact of attenuation due to precipitation needs to be resolved for successful implementation. In this research, new attenuation correction algorithms are introduced to compensate the attenuation impact due to rain medium.

In order to design X-band radar systems as well as evaluate algorithm development, it is useful to have simultaneous X-band observation with and without the impact of path attenuation. One way to obtain that data set is through theoretical models. Methodologies for generating realistic range profiles of radar variables at attenuating frequencies such as X-band for rain medium are presented here. Fundamental microphysical properties of precipitation, namely size and shape distribution information, are used to generate realistic profiles of X-band starting with S-band observations. Conditioning the simulation from S-band radar measurements maintains the natural distribution of microphysical parameters associated with rainfall. In this research, data taken by the CSU-CHILL radar and the National Center for Atmospheric Research S-POL radar are used to simulate X-band radar variables. Three procedures to simulate the radar variables at X-band and sample applications are presented.

A new attenuation correction algorithm based on profiles of reflectivity, differential reflectivity, and differential propagation phase shift is presented. A solution for specific attenuation retrieval in rain medium is proposed that solves the integral equations for reflectivity and differential reflectivity with cumulative differential propagation phase shift constraint. The conventional rain profiling algorithms that connect reflectivity and specific attenuation can retrieve specific attenuation values along the radar path assuming a constant intercept

parameter of the normalized drop size distribution. However, in convective storms, the drop size distribution parameters can have significant variation along the path. In this research, a dual-polarization rain profiling algorithm for horizontal-looking radars incorporating reflectivity as well as differential reflectivity profiles is developed. The dual-polarization rain profiling algorithm has been evaluated with X-band radar observations simulated from drop size distribution derived from high-resolution S-band measurements collected by the CSU-CHILL radar. The analysis shows that the dual-polarization rain profiling algorithm provides significant improvement over the current algorithms.

A methodology for reflectivity and attenuation retrieval for rain medium in a networked radar environment is described. Electromagnetic waves backscattered from a common volume in networked radar systems are attenuated differently along the different paths. A solution for the specific attenuation distribution is proposed by solving the integral equation for reflectivity. The set of governing integral equations describing the backscatter and propagation of common resolution volume are solved simultaneously with constraints on total path attenuation. The proposed algorithm is evaluated based on simulated X-band radar observations synthesized from S-band measurements collected by the CSU-CHILL radar. Retrieved reflectivity and specific attenuation using the proposed method show good agreement with simulated reflectivity and specific attenuation.

Sanghun Lim
Electrical and Computer Engineering Department
Colorado State University
Fort Collins, Colorado 80523
Summer 2006

ACKNOWLEDGEMENTS

First of all, I would like to express gratitude to my adviser, Dr. V. Chandrasekar, for his inspiring guidance, encouragement, and support during my graduate studies. I am also grateful to Dr. V. N. Bringi for his source of knowledge and keen insight into all complicated problem. Gratitude is extended to Dr. Anura P. Jayasumana and Dr. P. Mielke for serving as my committee members, for their corrections and suggestions to help enhance the dissertation greatly.

Additionally, I would like to thank everyone in our Radar and Communication Group: Dr. Yoong-Goog Cho for his kindness and encouragement, N. Bharadwaj, Dr. C.R. Rose, Dr. W. Li, Dr. Y. Wang, G. Xu and Dr. G.J. Huang for their helpful assistance and friendship.

I am deeply grateful to my parents, Soonim Kim and Taewoo Lim, my parents-in-law, Boksook Lee and Sangyong Kim, and my brothers and sister, Honggul Lim, Jungsu Lim, Hongsu Lim and Kyungeun Lim, for their support and love.

Finally and foremost, I would like to express my deep appreciation to my wife Eunjong Kim, my daughter Jeewoo Lim, and son Junyoung Lim for their love, support, and encouragement, which made this research possible.

The research was supported by the NSF (ERC-0313747, ATM-0313881).

TABLE OF CONTENTS

LIST OF TABLES

LIST OF FIGURES

CHAPTER 1

INTRODUCTION

1.1 Historical Overview of the Attenuation Correction Techniques

Conventional meteorological radars have operated at S-band frequency in order to obtain coverage over long ranges and minimize the attenuation effects due to precipitation. These systems necessitate the use of physically large antennas and high-power transmitters to achieve high resolution at distant ranges. As an alternate solution, higher frequency radars such as X-band have been attracting attention for their low cost, smaller antennas and targeted applications such as coverage over a city or a small basin. However, at frequencies higher than S-band, attenuation effects caused by precipitation can be significant. As a consequence, for any quantitative application that uses reflectivity or (and) differential reflectivity, the radar measurements need to be properly compensated.

Since Hitschfeld and Bordan (1954) proposed the attenuation correction method using the empirical relationship of reflectivity versus specific attenuation, many researchers have studied attenuation correction techniques. With development of dual-polarization radar, reflectivity and differential reflectivity have been used for attenuation correction with iterative approaches (Hildebrand 1978; Aydin et al. 1989; Gorgucci et al. 1996). These methods are very sensitive to calibration errors and unstable for large path-integrated attenuation. In alternative approaches, the use of a differential propagation phase that is linearly proportional to attenuation in typical radar frequencies (3-10 GHz) was introduced (Bringi et al. 1990; Jameson 1992; Smyth and Illingworth 1998; Carey et al. 2000). This method is much better than a reflectivity-attenuation parameterization. A more recent approach to attenuation correction is rain profiling method that uses total path-integrated attenuation as a

constraint. This method was developed for spaceborne radar with path-integrated attenuation derived by surface reference technique (Meneghini and Nakamura 1990; Marzoug and Amayenc 1994). For ground radars with polarimetric capability, a method using path-integrated attenuation derived from differential phase shift as a constraint was proposed (Testud et al. 2000). This algorithm is sensitive to the attenuation-specific differential phase parameterization. To eliminate this problem, a self-consistent algorithm combining differential phase shift and differential reflectivity constraint was proposed by Bringi et al. (2001). One common drawback of the rain profiling algorithm is an assumption that intercept parameter, N_w, of normalized drop size distribution is constant along a path. Overcoming this problem can be a motivation for the development of a new rain profiling algorithm.

For ground radar, an alternative solution of the retrieval technique for specific attenuation and reflectivity was a dual-radar method, which was proposed and evaluated by Srivastava and Tian (1996) and Tian and Srivastava (1997). A solution for specific attenuation and reflectivity was solved by an analytical method. This method has an advantage because it does not need targets of fixed or known cross section. However, this method has many constraints in its use because it is sensitive to initial specific attenuation and distance between radars. This method is also difficult to extend to multiple radar system.

1.2 Problem Statement

One advantage of X-band radar systems over S-band systems in monitoring precipitation events is low cost due to smaller antennas and low power transmitters. X-band radar systems can also provide more precise radar measurements of weak precipitation and larger values of radar measurements for strong precipitation. Therefore, use of X-band radar systems for any quantitative application can provide more accuracy. However, X-band radar measurements can be attenuated significantly due to precipitation. For successful implementation of X-band radar, the radar measurements need

to be properly compensated to minimize the impact of attenuation.

Based on the analysis presented in the previous section, this research proposes improved attenuation correction algorithms. This research attempts to address the impact of attenuation and solutions for radar observation retrieval in an X-band networked radar environment.

1.3 Objectives of the Research

The objectives of this research consist of the simulation of X-band observations, the retrieval of radar observations using dual-polarization rain profiling algorithm, and reflectivity retrieval in a networked radar environment. The following summarizes the objectives of the research.

1.3.1 Simulation of X-band rainfall observations from S-band radar data

In order to evaluate algorithm development, it is useful to have simultaneous radar observation with and without the effects of path attenuation. One way to obtain such data is from dual-polarization radar measurements. This method can provide the realistic scenario of a precipitation event, conceiving the natural distribution of microphysical properties in rain medium. In this research, three different approaches will be studied. The first approach is an empirical conversion method that synthesizes X-band radar observations from high-resolution S-band dual-polarization measurements using the relationship between S- and X-band observations. The relationship can be derived from theoretical simulation of drop size distribution. The second approach is the DSD inversion method, which simulates X-band observations from drop size distribution estimated from dual-polarization radar measurements at S-band. The third approach is the DSD sampling method, which lies between the empirical conversion method and the full DSD inversion method. These three methodologies will be studied extensively.

1.3.2 A dual-polarization rain profiling algorithm

The conventional rain profiling algorithm that connects reflectivity and specific attenuation can retrieve specific attenuation values along the radar path assuming constant intercept parameter, N_w, of the normalized drop size distribution. However, in the convective storm case, the DSD parameters can have significant variation along a path. The differential reflectivity varies with drop size. By inclusion of differential reflectivity in the rain profiling algorithm, we can solve the problem of assuming a constant intercept parameter. A dual-polarization rain profiling algorithm for horizontal-looking radars connecting reflectivity as well as differential reflectivity profiles with total cumulative attenuation will be studied. Specific attenuation retrieval in rain medium can be solved by the integral equations for reflectivity and differential reflectivity with cumulative differential propagation phase constraint. The algorithm will be evaluated with X-band radar observations simulated from drop size distribution derived by high-resolution S-band measurements taken by the CSU-CHILL radar.

1.3.3 Retrieval of reflectivity in a networked radar environment

Electromagnetic waves backscattered from a common volume in networked radar systems are attenuated differently along the different paths. A solution for the specific attenuation distribution in a networked radar system can be provided by solving the integral equation for reflectivity. The set of governing integral equations describing the backscatter and propagation of common volume are solved simultaneously with constraints on total path attenuation. A methodology for reflectivity and attenuation retrieval for rain medium in a networked radar environment will be studied. The algorithm will be evaluated based on simulated X-band radar observations synthesized from S-band measurements collected by the CSU-CHILL radar.

1.4 Overview of the Dissertation

This dissertation is organized as follows:

Chapter 1 - Introduction

Chapter 2 - Theoretical background

Rain model and polarimetric radar observations are described. The concept of the networked radar environment is also presented.

Chapter 3 - Simulation of X-band rainfall observations from S-band radar data

Three procedures for simulating the radar variables at X-band using S-band radar data and sample applications are presented. The comparison of the results of the three methods is also discussed.

Chapter 4 - A dual-polarization rain profiling algorithm

A new attenuation correction algorithm based on profiles of reflectivity, differential reflectivity, and differential propagation phase shift is proposed. The evaluation of the proposed algorithm with X-band radar observations simulated from drop size distribution derived from high-resolution S-band measurements collected by the CSU-CHILL radar is also presented.

Chapter 5 - Retrieval of reflectivity in a networked radar environment

A solution for the specific attenuation distribution in the networked radar environment is proposed by solving the integral equation for reflectivity. Based on X-band radar observations simulated from S-band measurements collected by the CSU-CHILL radar, the evaluation of the algorithm is presented.

Chapter 6 - Summary and future work

The results of this research are summarized and the major contributions of the dissertation are reviewed. Suggestions for future work are proposed.

CHAPTER 2

THEORETICAL BACKGROUND

2.1 Rain Model

Microphysical properties of rain medium can be described by drop size distribution (DSD). Natural variation of drop size distribution can be parameterized adequately by Gamma model as (Ulbrich 1983)

$$N(D) = N_0 D^{\mu} e^{-\Lambda D}; \mu > -1 \tag{2.1}$$

where $N(D)$ is the number of the raindrops per unit volume per unit size interval, D (in mm) is the volume-equivalent spherical diameter, and N_0 ($mm^{-1-\mu}m^{-3}$), Λ (mm^{-1}) and μ are the parameters of the distribution. One disadvantage of the Gamma model is that the unit of N_0 depends on μ. To study the shape of DSD with widely varying rainfall rates, Gamma distribution can be expressed in normalized form as (Sekhon and Srivastava 1971; Willis 1984; Testud et al. 2001; Bringi and Chandrasekar 2001)

$$N(D) = N_w f(\mu) \left(\frac{D}{D_0}\right)^{\mu} exp\left[-(3.67+\mu)\frac{D}{D_0}\right]; \tag{2.2}$$

$$f(\mu) = \frac{6}{(3.67)^4}\frac{(3.67+\mu)^{\mu+4}}{\Gamma(\mu+4)} \tag{2.3}$$

where D_0 is the median volume diameter, μ is a measure of the shape of the DSD, and N_w ($mm^{-1}m^{-3}$) is the intercept parameter of the exponential distribution with same water content and D_0.

Raindrops are shaped by a balance of surface tension and hydrostatic pressure along with aerodynamic constraints. Raindrop shapes can be approximated as oblate spheroids with the axis ratio. The raindrop shapes have been extensively studied. A

useful linear fit to the wind-tunnel data of Pruppacher and Beard (1970) is

$$\frac{b}{a} = 1.03 - 0.062D; \quad 1 \leq D \leq 9mm \tag{2.4}$$

where a and b are the major and minor axes of the spheroid. A polynomial fit to the numerical model of Beard and Chuang (1987) is

$$\frac{b}{a} = 1.0048 + 0.0057\left(\frac{D}{10}\right) - 2.628\left(\frac{D}{10}\right)^2 + 3.682\left(\frac{D}{10}\right)^3 - 1.677\left(\frac{D}{10}\right)^4; \tag{2.5}$$

$0 \leq D \leq 7mm.$

Another polynomial fit of Andsager et al. (1999) is

$$\frac{b}{a} = 1.012 - 0.144\left(\frac{D}{10}\right) - 1.03\left(\frac{D}{10}\right)^2; \quad 1 \leq D \leq 4mm. \tag{2.6}$$

This model synthesizes the effects of raindrop oscillations for drops using both laboratory axis ratio data as well as field measurements.

2.2 Polarimetric Radar Observables

Radar observations in rain medium can be expressed in terms of DSD. Reflectivity factors $Z_{h,v}$ at horizontal (h) and vertical (v) polarizations can be described as

$$Z_{h,v} = \frac{\lambda^4}{\pi^5 |K_w|^2} \int \sigma_{h,v}(D) N(D) dD; \quad (mm^6 m^{-3}) \tag{2.7}$$

where λ is the wavelength of the radar and $\sigma_{h,v}$ represents the radar cross sections at horizontal and vertical polarizations. K_w is the dielectric factor of water defined as $K_w = (\epsilon_r - 1)/(\epsilon_r + 2)$, where ϵ_r is the complex dielectric constant of water. Differential reflectivity can be expressed as the ratio of reflectivity factors at horizontal and vertical polarizations (Seliga and Bringi 1976).

$$10log_{10}(Z_{dr}) = 10log_{10}\left(\frac{Z_h}{Z_v}\right) \tag{2.8}$$

Specific differential phase is proportional to the real part of the difference in the complex forward scatter amplitudes f at horizontal and vertical polarizations. It can be defined as

$$K_{dp} = \frac{180}{\pi}\lambda Re \int [f_h(D) - f_v(D)]N(D)dD; \quad (\deg km^{-1}). \tag{2.9}$$

The two-way differential propagation phase ϕ_{dp} is defined as

$$\phi_{dp} = 2\int K_{dp}(r)dr. \tag{2.10}$$

The measured differential propagation phase can be defined as

$$\psi_{dp} = \phi_{dp} + \delta \tag{2.11}$$

where δ is the backscattering propagation phase that is the difference between arguments of the complex backscattering amplitudes for horizontal and vertical polarizations (Tan et al. 1991). Electromagnetic waves passing through precipitation suffer from the power loss resulting from absorption and scattering. Specific attenuation at two polarization states and differential attenuation are related to DSD as

$$\begin{aligned} \alpha_{h,v} &= 4.343 \times 10^{-3}\int_D \sigma_{ext}(D)N(D)dD; \quad (dBkm^{-1}) \\ \alpha_{dp} &= \alpha_h - \alpha_v \end{aligned} \tag{2.12}$$

where σ_{ext} is the extinction cross section (m^2) derived by the sum of absorption cross section and scattering cross section. At centimeter wavelengths, absorption dominates for all rain rates (Doviak and Zrnić 1993). Two-way cumulative attenuation A_h and differential attenuation A_{dp} can be expressed as

$$\begin{aligned} A_h &= 2\int_{r_0}^{r} \alpha_h(s)ds; \\ A_{dp} &= 2\int_{r_0}^{r} \alpha_{dp}(s)ds \end{aligned} \tag{2.13}$$

where s is range for integration. Attenuation can also be due to atmospheric gases or cloud droplets. For X-band radar with short range, the attenuation effects by atmospheric gases or cloud droplets are negligible compared to attenuation due to rain.

2.3 Networked Radar Environment

The U.S. National Science Foundation recently established an Engineering Research Center titled the Center for Collaborative Adaptive Sensing of the Atmosphere (CASA), formed by a consortium of four universities, the Colorado State University, the University of Massachusetts (lead university), the University of Oklahoma, and the University of Puerto Rico and partnerships with industry and government labs to create the underlying scientific and engineering basis for a new paradigm of networked radars applied to hazardous localized weather detection, tracking, and predicting.

The usefulness of radar to a specific application is heavily dependent on the accuracy and resolution of coverage. A fundamental physical limit imposed by transmission from single radar is the problem of changing resolution as a function of range. In addition, the lowest coverage altitude gets higher with range due to earth curvature (Chandrasekar et al. 2004b). A networked radar environment concept has been proposed (Chandrasekar and Jayasumana 2001; McLaughlin 2001). The concept of a networked radar system is simultaneous observations of the same precipitation event by multiple radars in different locations. The networked radar system is capable of high spatial coverage and temporal resolution. Fig. 2.1 shows a networked radar system. The radars are situated at different locations, operating at the same attenuating frequency and scanning in a low elevation plane. By assimilating observations from the multiple radars, we can retrieve more accurate information of a precipitation event. In order to provide economically viable solutions to this approach, meteorological radars need to change S-band radar to higher-frequency radar such as X-band using small antennas and low power transmitters.

The first generation network node for the first Integrating Project (IP1) will be deployed in Oklahoma with four sensing nodes. The CASA radar is an X-band pulsed Doppler system. The radar consists of a magnetron transmitter and a dual-channel receiver. The characteristics of the CASA radar are detailed in Table 2.1. For

comparison with a typical dual-polarization S-band radar system, the characteristics of the CSU-CHILL radar are listed in Table 2.2.

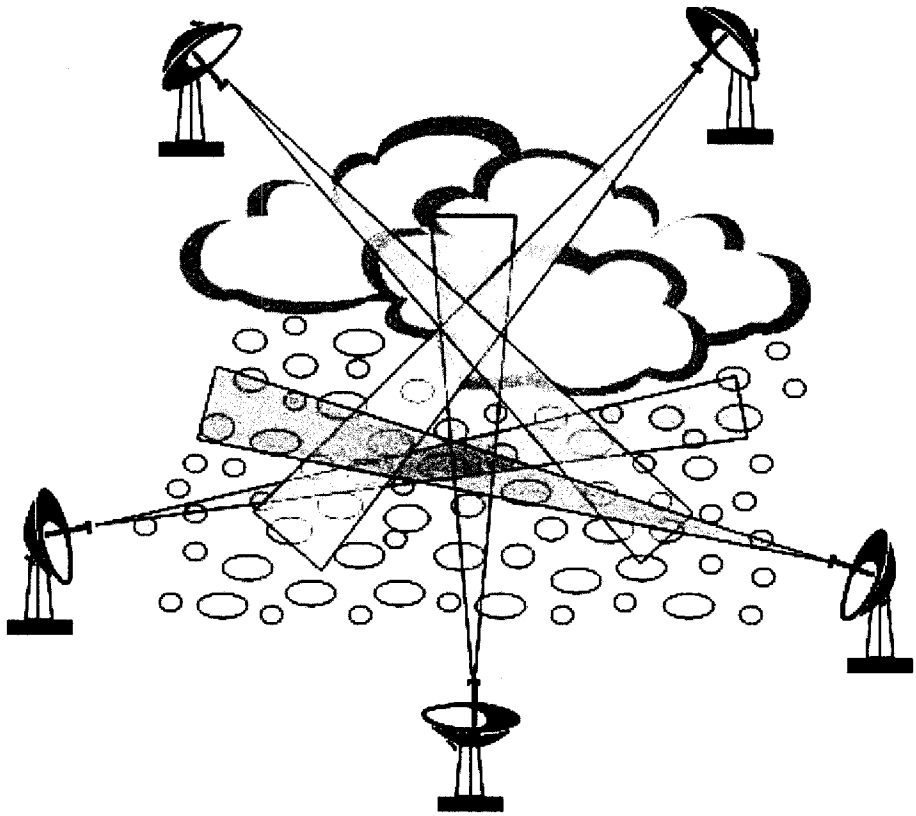

Figure 2.1: A conceptual illustration of a networked radar environment.

Table 2.1: CASA generation 1 - IP1 magnetron dish radar characteristics.

Frequency	9431 ± 30 MHz
Maximum Peak Power	25 kW
Maximum Duty Cycle	0.1 %
Maximum Pulse Length	2 μs
Transmitter Polarization	Elliptical (Hybrid mode)
Receiver Polarization	Dual linear V and H
Receiver Gain	30 dB
Final Dynamic Range referenced at input (BW = 1.5 MHz)	-106.2 dBm to -3 dBm
Antenna Diameter	1.2 m
Antenna Gain	38 dB
Antenna Beamwidth	1.8 deg
Azimuth Scan Rate	120 deg/sec
Elevation Scan Rate	30 deg/sec

Table 2.2: CSU-CHILL radar characteristics.

Antenna	
Shape	Parabolic
Size	8.5 m
Feed type	scalar horn
Gain	43 dB(includes waveguide loss)
3 dB Beamwidth	1.1 deg
Maximum sidelobe	-27 dB(In worst πplane)
Inter-channel isolation	-45 dB(limited by orothomode transducer)
ICPR(two-way)	-34 dB
Transmitters	
Wavelength	11.01 cm
Peak Power	800 $\sim$ 1000 KW
Final PA Type	VA-87B/C(Klystron)
Pulse Width	0.3 $\sim$ 1.0 μs in steps of 0.1 μs
PRT	800 $\sim$ 2500 μs
Available Polarizations	Horizontal, Vertical, slant $45^o/135^o$, right/left circular
Receivers/Digital Signal Processing	
Noise figure	$\sim$ 3.4 dB
Noise Power at SNR=1	$\sim$ -114.0 dBm
Dynamic range	$\sim$ 96 dB
Bandwidth	750 KHz typ. with programmable filter
Output Range Resolution	45 m minimum, adjustable upward in 15 m intervals
Maximum range gates	estimated to be $>$ 3000

CHAPTER 3

SIMULATION OF X-BAND RAINFALL OBSERVATIONS FROM S-BAND RADAR DATA

3.1 Introduction

Monitoring of precipitation using high frequency radar systems such as X-band is becoming increasingly popular due to the systems' lower cost compared to their counterpart at S-band (Chandrasekar et al. 2004b; Park et al. 2005a). For urban or mountain hydrological applications, the X-band radar systems have been implemented in Europe and Japan (Delrieu et al. 1997; Testud et al. 2000; Park et al. 2005b). Meteorological radar systems operating at S-band frequency are mostly not affected by attenuation due to precipitation, except in some regions of wet hail. The S-band radar systems with narrow beams (say one degree beam width) are typically expensive, using large antennas and high power transmitters to cover large areas. Recently, networks of meteorological radar systems at higher frequencies such as X-band have been pursued, especially for low cost and targeted applications such as coverage over a city or a small basin. However, at higher frequencies, the impact of attenuation due to precipitation needs to be resolved for successful implementation.

In order to design the radar systems as well as evaluate algorithm development, it is useful to have simultaneous radar observations with and without the impact of path attenuation. One way to collect such data is from a dual-frequency radar system with matched beams. Chandrasekar et al. (2002, 2004a) studied the relationship between the intrinsic radar variables of S- and X-band in rain medium. Note that "intrinsic" refers to the radar variables that are non-attenuated and obtained by theoretical simulation. Using such a relationship, an alternative solution can be proposed to

obtain radar data of high frequencies from dual-polarization observations at lower frequencies such as S-band. Extensive dual-polarization observations of precipitation at S-band are available today from research radar facilities such as CSU-CHILL and SPOL radars.

This chapter presents three methodologies to simulate X-band radar variables in rain from S-band data. These methodologies can simulate the realistic dual-polarization radar variables while maintaining the natural spatial structure of the rainfall event. The simulated data set with and without attenuation effect can be used effectively in the design of X-band radar system as well as in the evaluation of algorithm development such as attenuation correction (Chandrasekar et al. 2006). This chapter is organized as follows. In Section 3.2, the methods that simulate X-band variables from S-band data are described and the results of the three methodologies are compared in Section 3.3. The important results are summarized in Section 3.4.

3.2 Relationship between X-band and S-band radar variables

Methodologies to simulate realistic radar observations for X-band from S-band measurements were discussed by Chandrasekar et al. (2004a) and Lim et al. (2004). Three different methodologies for the simulation of X-band radar variables from S-band dual-polarization radar measurements will be discussed in the following, namely empirical conversion method, DSD sampling method, and DSD inversion method.

3.2.1 Empirical conversion method

The intrinsic measurements of Z_h and Z_{dr} exhibit a nearly one-to-one relation between S- and X-band. This principle was used by Chandrasekar et al. (2003) to characterize spaceborne radar observations at multiple frequencies. Fig. 3.1 shows a scatter plot of Z_h and Z_{dr} at S- and X-band for widely varying drop size distributions ($0.5 \leq D_0 \leq 3.5\ mm$, $3 \leq log_{10}N_w \leq 5$ and $-1 < \mu \leq 4$ for $R < 300\ mmh^{-1}$ and $Z_h < 55\ dBZ$). The data were obtained by scattering simulation using the shape

model proposed by Bringi et al. (2003), which combines the Andsager et al. (1999) fit and the Beard and Chuang (1987) model at a temperature of $10°C$ (henceforth referred as the ABC model). Under Rayleigh scattering assumptions, reflectivity will not change with frequency. However, Rayleigh scattering assumption is not strictly valid at X-band, as shown in Fig. 3.1(a). The comparison of Z_{dr} in Fig. 3.1(b) shows the non-Rayleigh scattering very well.

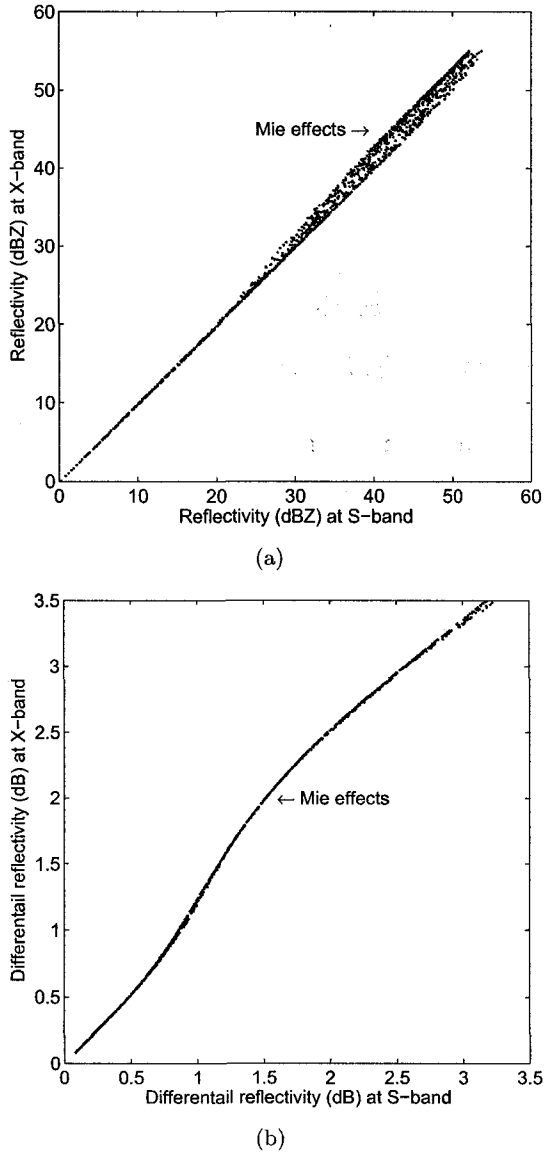

Figure 3.1: (a) Scatter plot of reflectivity and (b) differential reflectivity at S- and X-band for widely varying drop size distributions.

Under the assumption that S-band radar observations are non-attenuated, the empirical conversion method synthesizes the simulated X-band radar variables from high-resolution S-band dual-polarization measurements using the relationship between S- and X-band radar variables, which is derived from scattering simulation with various drop size distributions. The relationship can be defined as

$$\begin{aligned} 10log_{10}(Z_{h,X}) &= f_1(10log_{10}(Z_{h,S}), 10log_{10}(Z_{dr,S})); \\ 10log_{10}(Z_{dr,X}) &= f_2(10log_{10}(Z_{h,S}), 10log_{10}(Z_{dr,S})) \end{aligned} \tag{3.1}$$

and

$$\begin{aligned} \alpha_{h,X} &= f_3(10log_{10}(Z_{h,S}), 10log_{10}(Z_{dr,S})); \\ \alpha_{dp,X} &= f_4(10log_{10}(Z_{h,S}), 10log_{10}(Z_{dr,S})) \end{aligned} \tag{3.2}$$

where subscripts X and S indicate simulated radar variables at X-band and measured (assumed non-attenuated) radar measurements at S-band, respectively. The relationship between X- and S-band radar data can be obtained by regression. The data are obtained from the theoretical simulation using DSD parameters. This method is simple and reliable for reflectivity and differential reflectivity simulation. Using data based on the ABC model at a temperature of $10°C$ for widely varying DSD, the relationship can be expressed as

$$\begin{aligned} 10log_{10}(Z_{h,X}) &= a_1 + b_1[10log_{10}(Z_{h,S})]^{c_1} + d_1[10log_{10}(Z_{dr,S})]^{e_1}; \\ 10log_{10}(Z_{dr,X}) &= a_2[10log_{10}(Z_{h,S})]^{b_2}[10log_{10}(Z_{dr,S})]^{c_2}; \\ \alpha_{h,X} &= 10^{a_3+b_3[10log_{10}(Z_{h,S})]^{c_3}+d_3[10log_{10}(Z_{dr,S})]^{e_3}}; \\ \alpha_{dp,X} &= 10^{a_4+b_4[10log_{10}(Z_{h,S})]^{c_4}+d_4[10log_{10}(Z_{dr,S})]^{e_4}}. \end{aligned} \tag{3.3}$$

The parameters of (3.3) are listed in Table 3.1. Fig. 3.2 shows the scatter plot of intrinsic radar data obtained by theoretical simulation using widely varying DSD parameters versus radar data simulated by (3.3). From the results shown in Fig. 3.2, we can see that the proposed method works reasonably well. Fig. 3.3 shows the comparison of intrinsic and simulated for Z_h versus Z_{dr}, Z_h versus α_h and Z_h versus

Table 3.1: The parameters of relationship of S- and X-band radar variables obtained by ABC model at a temperature of $10°C$.

	Parameters	Condition
$Z_{h,X}$	$a_1 = -0.19,\ b_1 = 1,\ c_1 = 1,\ d_1 = 0,\ e_1 = 0$	$Z_{h,S} < 25dBZ$
	$a_1 = 0,\ b_1 = 0.768,\ c_1 = 1.056,\ d_1 = 2.813,\ e_1 = 0.553$	$Z_{h,S} \geq 25\ dBZ$
$Z_{dr,X}$	$a_2 = 1.067,\ b_2 = 0.002,\ c_2 = 1.039$	$Z_{dr,S} < 0.5\ dB$
	$a_2 = 1.27,\ b_2 = 0.006,\ c_2 = 1.294$	$0.5 \leq Z_{dr,S} < 1.25\ dB$
	$a_2 = 1.479,\ b_2 = -0.004,\ c_2 = 0.777$	$1.25 \leq Z_{dr,S} < 2.5\ dB$
	$a_2 = 1.569,\ b_2 = -0.004,\ c_2 = 0.701$	$Z_{dr,S} \geq 2.5\ dB$
$\alpha_{h,X}$	$a_3 = 1.579,\ b_3 = 0.884,\ c_3 = 1.07,\ d_3 = -6.922,\ e_3 = 0.054$	$Z_{h,S} < 40\ dBZ$
	$a_3 = -4.19,\ b_3 = 0.892,\ c_3 = 1.044,\ d_3 = -1.819,\ e_3 = 0.875$	$Z_{h,S} \geq 40\ dBZ$
$\alpha_{dp,X}$	$a_4 = 1.156,\ b_4 = 1.034,\ c_4 = 0.982,\ d_4 = -6.593,\ e_4 = -0.016$	$Z_{h,S} < 40\ dBZ$
	$a_4 = -4.546,\ b_4 = 1.216,\ c_4 = 0.925,\ d_4 = -1.532,\ e_4 = 0.02$	$Z_{h,S} \geq 40\ dBZ$

α_{dp}. The results of Fig. 3.3 indicate that the simulated radar data are properly related to each other. The attenuated reflectivity $Z'_{h,X}$ and attenuated differential reflectivity $Z'_{dr,X}$ can be generated with respect to radar variables simulated by (3.1) - (3.2) as

$$\begin{aligned} 10log_{10}(Z'_{h,X}) &= 10log_{10}(Z_{h,X}) - 2\int_{r_0}^{r} \alpha_{h,X}(s)ds; \\ 10log_{10}(Z'_{dr,X}) &= 10log_{10}(Z_{dr,X}) - 2\int_{r_0}^{r} \alpha_{dp,X}(s)ds \end{aligned} \tag{3.4}$$

where r_0 is the range corresponding to the first resolution volume with precipitation and r is the range of echo ($r_0 < r$). Note that attenuation due to clouds and gases are not considered in (3.4) because attenuation from clouds and gases is negligible compared to attenuation due to rain.

The simulation procedure of the empirical conversion method is shown in Fig. 3.4. An example of the simulation of attenuated X-band reflectivity is shown in Fig. 3.5. Fig. 3.5 (a) and (b) show S-band radar observations, whereas Fig. 3.5 (c) and (d) show the simulated X-band radar variables obtained by (3.1) and (3.2) using the S-band data set in Fig. 3.5 (a) and (b). Fig. 3.5 (e) shows the attenuated X-band reflectivity obtained by (3.4) using simulated X-band variables in Fig. 3.5 (c) and (d).

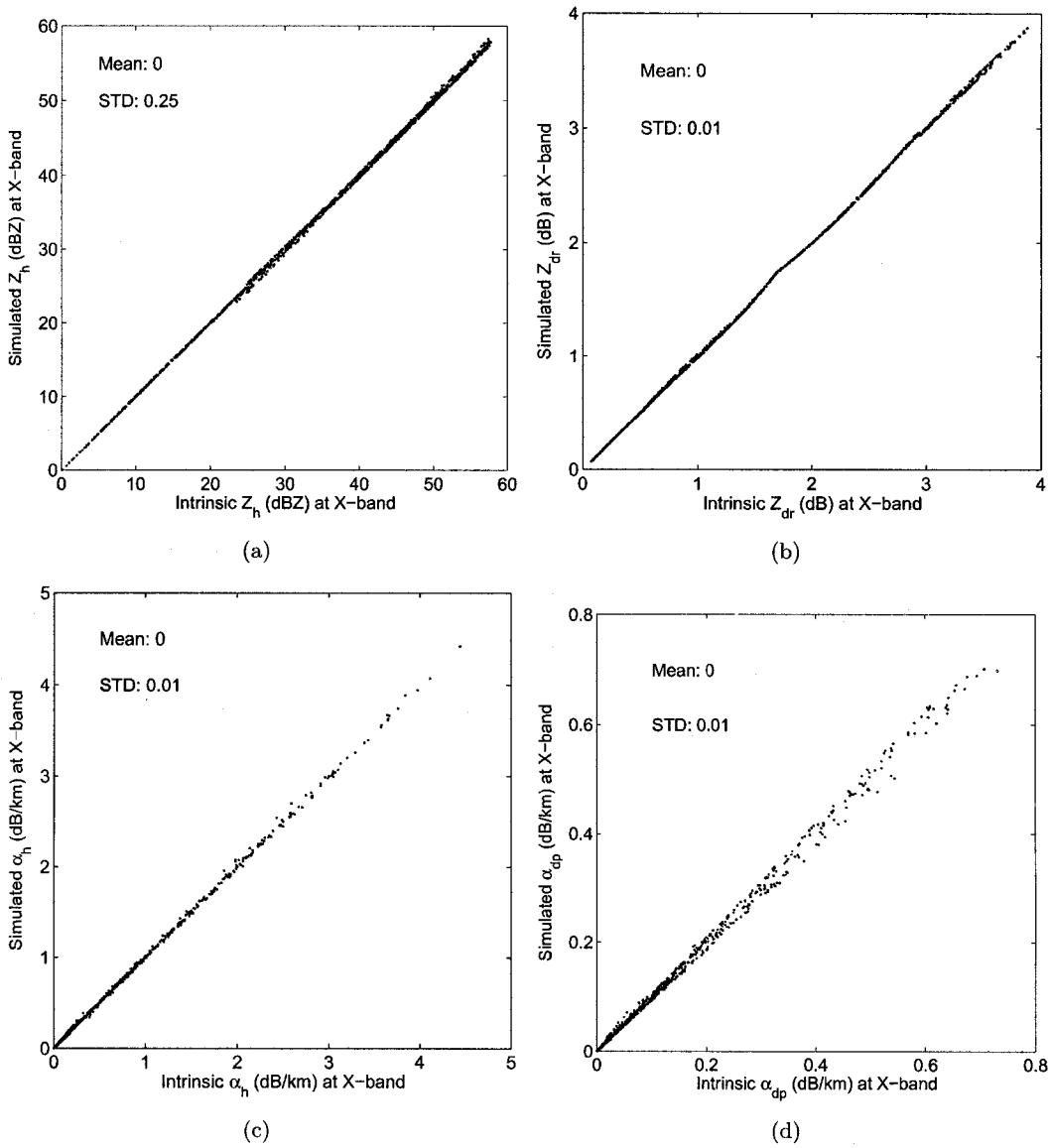

Figure 3.2: Scatter plot of (a) intrinsic reflectivity obtained by theoretical simulation using widely varying DSD versus simulated reflectivity by (3.1), (b) intrinsic differential reflectivity obtained by theoretical simulation using widely varying DSD versus simulated differential reflectivity by (3.1), (c) intrinsic specific attenuation versus simulated specific attenuation by (3.2), and (d) intrinsic differential attenuation versus simulated differential attenuation by (3.2) for X-band.

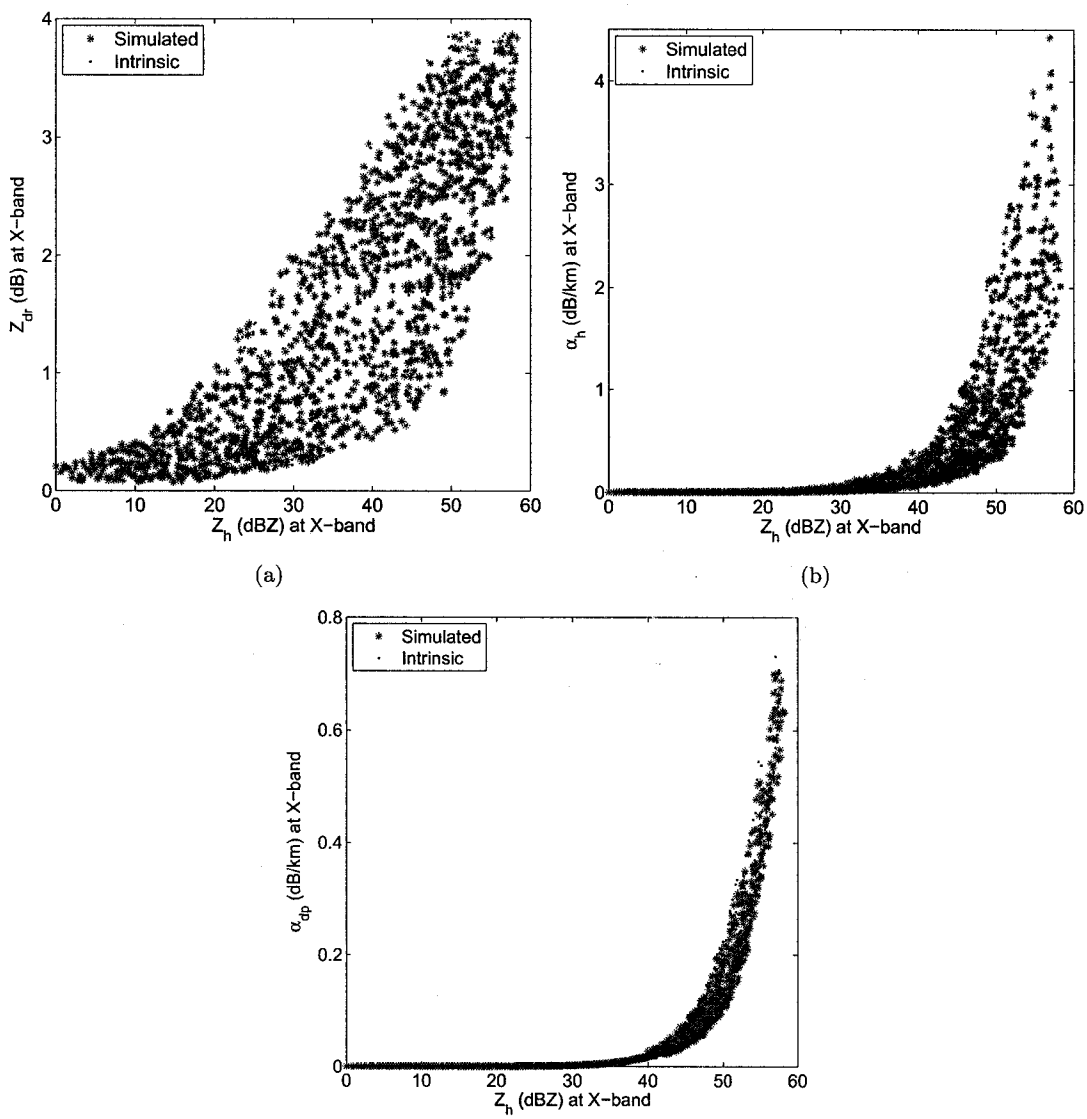

Figure 3.3: Comparison of intrinsic and simulated date for (a) reflectivity versus differential reflectivity, (b) reflectivity versus specific attenuation, and (c) reflectivity versus differential attenuation for X-band.

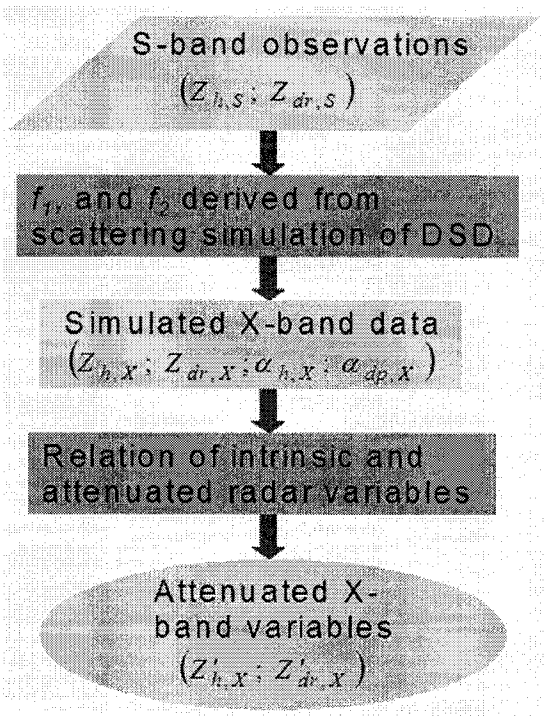

Figure 3.4: The block diagram of the empirical conversion method.

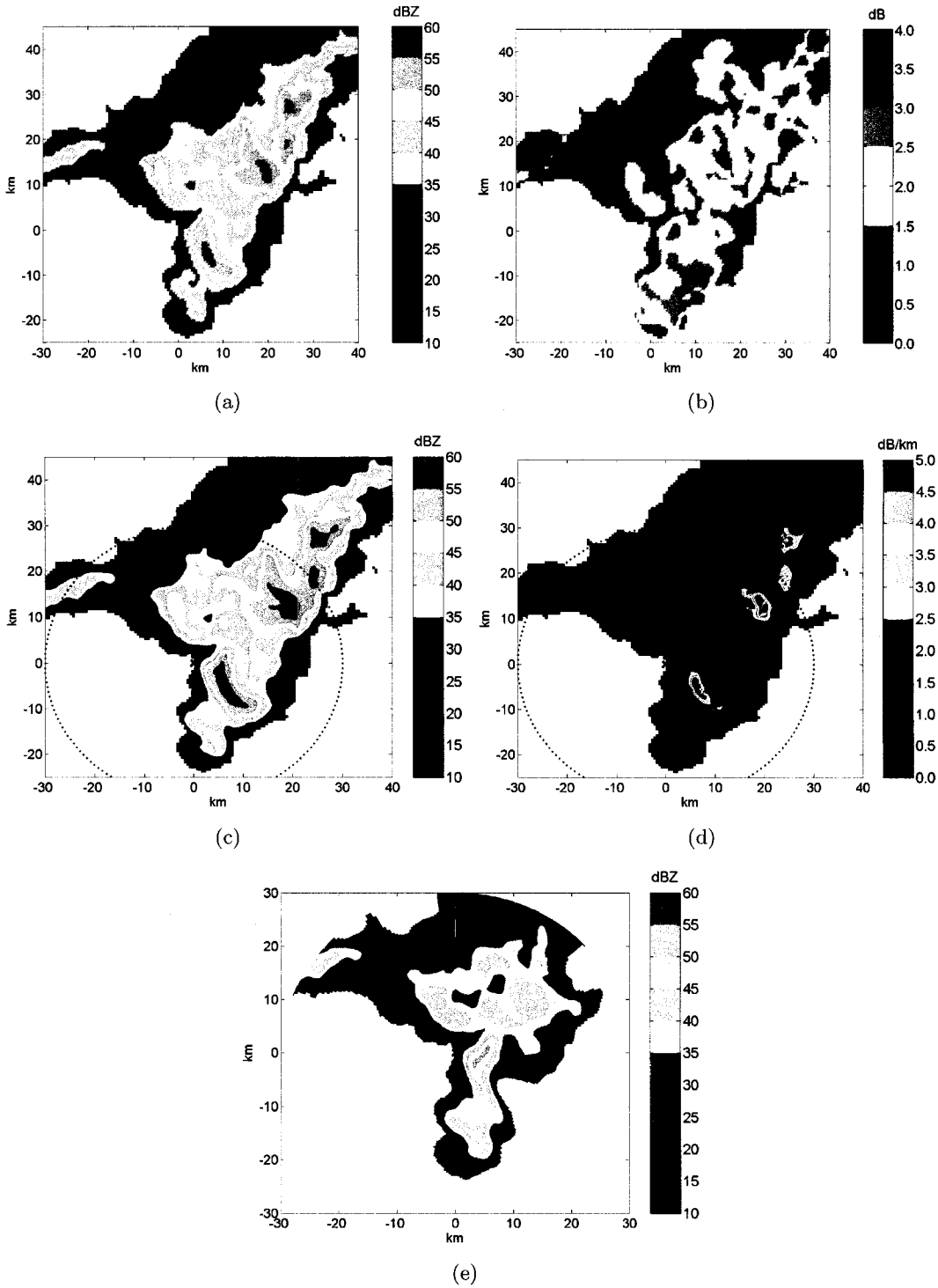

Figure 3.5: (a) Reflectivity at S-band, (b) differential reflectivity at S-band, (c) simulated reflectivity at X-band by (3.1), (d) simulated specific attenuation at X-band by (3.2), and (e) attenuated reflectivity at X-band by (3.4). "x" indicates the X-band radar location.

3.2.2 DSD sampling method

It was shown by Scarchilli et al. (1996) that the triplet of measurements Z_h, Z_{dr} and K_{dp} nearly lie on a three-dimensional surface. Fig. 3.6 shows the three-dimensional scatter plot of Z_h, Z_{dr} and K_{dp} obtained with widely varying DSD. Once Z_h and Z_{dr} are specified, the choice of possible K_{dp} falls in a narrow range. As a result, if we choose a value of K_{dp} at S-band corresponding to Z_h and Z_{dr}, then the K_{dp} value at X-band can be obtained by direct frequency scaling because K_{dp} is linearly proportional to frequency as (2.9). This procedure for choosing K_{dp} at S-band avoids the problem of direct K_{dp} estimation (Gorgucci et al. 2000) that can suppress peaks due to the slope estimation process that is used to derive K_{dp} from ϕ_{dp}. The above principle is implemented in a detailed manner as described in the following.

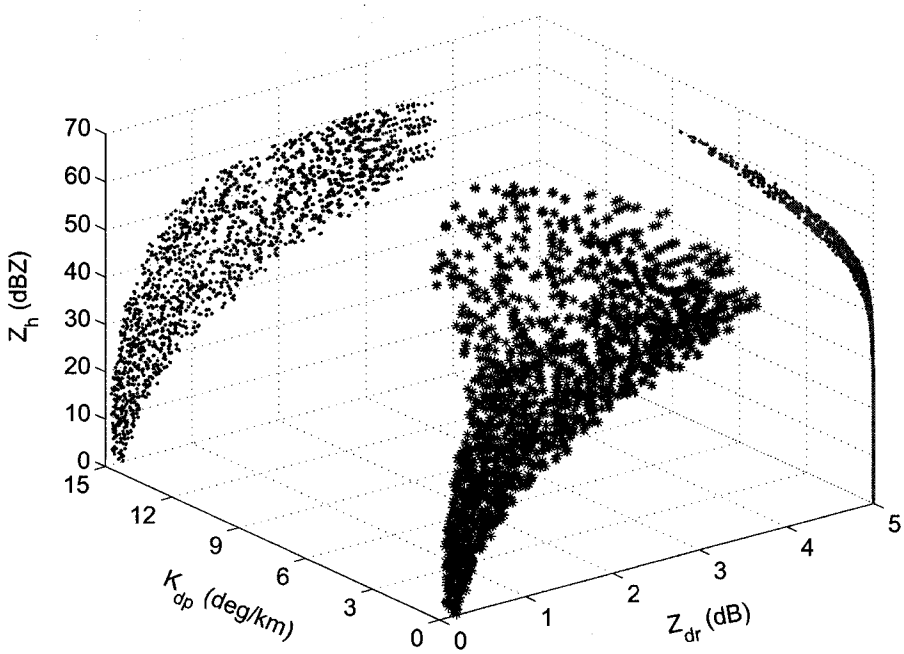

Figure 3.6: Three-dimensional scatter plot of Z_h, Z_{dr} and K_{dp} at S-band.

A large data set of Z_h, Z_{dr} and K_{dp} values at S-band are generated by the ABC model corresponding to a wide range of DSD parameters ($0.5 \leq D_0 \leq 3.5$ mm,

$3 \leq log_{10}N_w \leq 5$, $-1 < \mu \leq 4$) under the constraints of $Z_h < 55\ dB$ and $R < 300\ mmh^{-1}$. For a given set of Z_h and Z_{dr}, a search of this database provides possible choices of DSDs that satisfy the radar variables Z_h and Z_{dr}. One of those DSDs is randomly chosen to compute the X-band radar variables. Since the process is structured on DSD, the observed reflectivity and differential reflectivity can be computed according to (3.4). The block diagram in Fig. 3.7 provides a description of the simulation procedure. Fig. 3.8(a) shows the range profile of reflectivity and differential reflectivity from S-band (NCAR SPOL) polarimetric radar observed over central Florida. The simulated X-band profiles of $Z'_{h,X}(r)$, $Z_{h,X}(r)$ as well as $Z'_{dr,X}(r)$, $Z_{dr,X}(r)$ are shown in Fig. 3.8(b) and (c), whereas the profiles of ϕ_{dp} at S and X-band are shown in Fig. 3.8(d). A cursory glance at Fig. 3.8 shows that the simulation procedure produces reasonable range profiles of X-band radar variables. Once again, the purpose of this process is to simulate realistic range profiles of X-band dual-polarization variables in order to maintain the spatial correlation structure of the naturally occurring rainfall. It should be noted that the procedure is not to simulate the "exact" observation but to simulate profiles that fall within the range of observations.

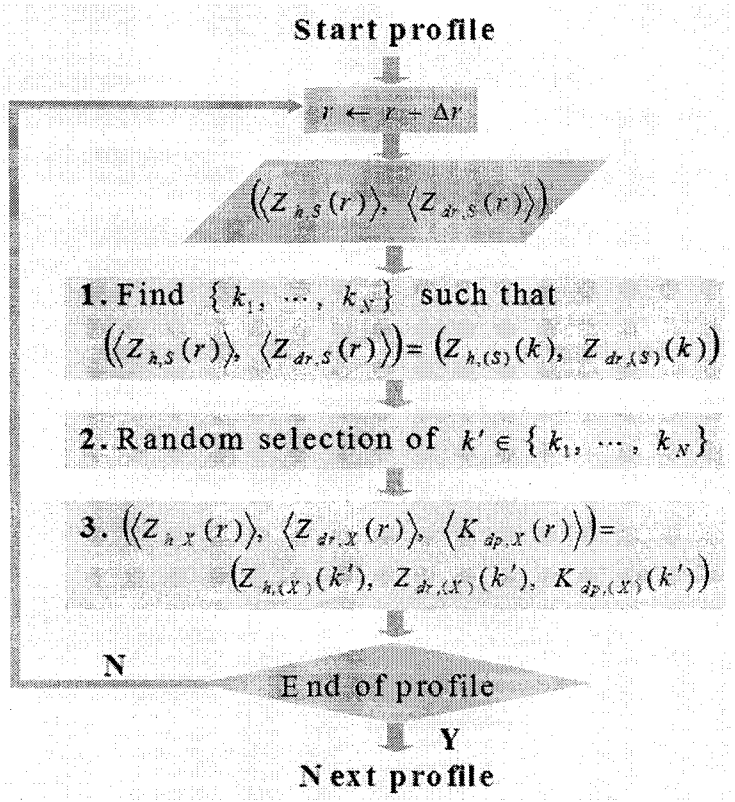

Figure 3.7: The block diagram of the DSD sampling method.

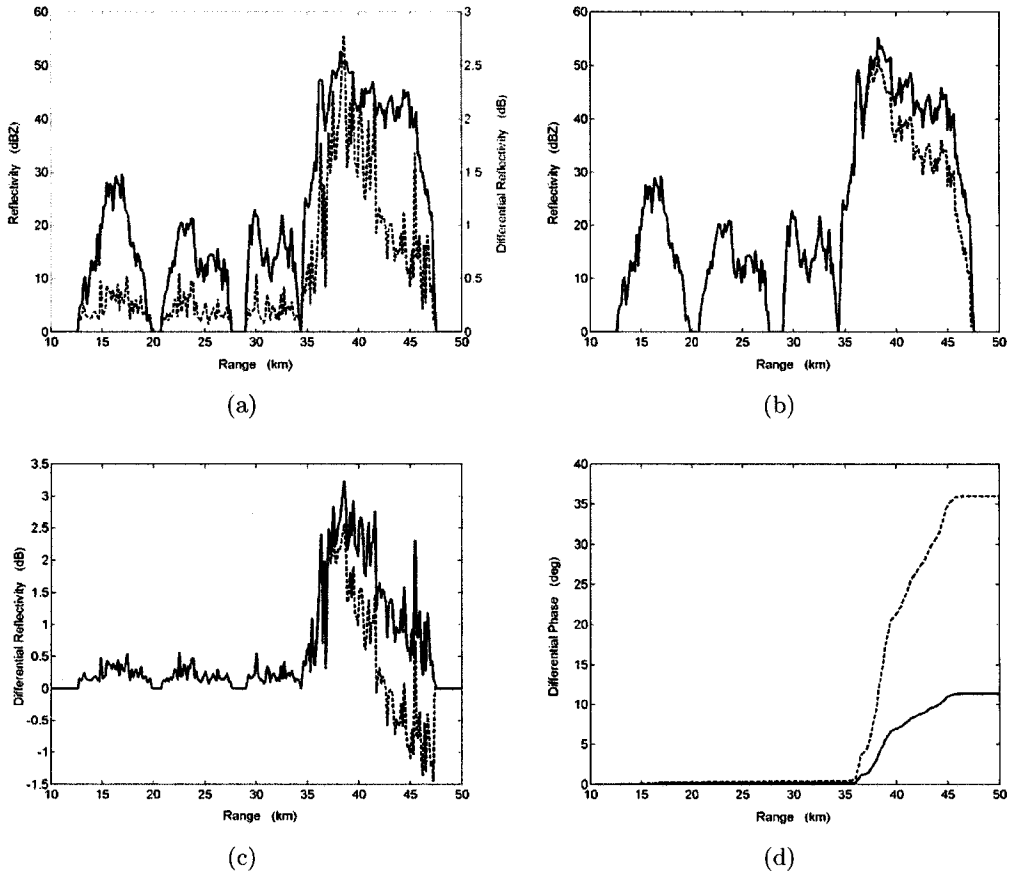

Figure 3.8: (a) Range profile of reflectivity and differential reflectivity from S-band polarimetric radar collected over central Florida, (b) simulated range profile of reflectivity at X-band (solid line) and the corresponding attenuated profile (dashed line), (c) simulated range profile of differential reflectivity at X-band (solid line) and the corresponding attenuated profile (dashed line), (d) differential phase profile at S-band (solid line) and the corresponding at X-band (dashed line).

3.2.3 DSD inversion method

The third method for simulating the X-band radar variables is to explicitly invert the DSD for each resolution volume and then compute the X-band radar variables. Gorgucci et al. (2002) and Bringi et al. (2002, 2003) proposed the method to retrieve the parameters of Gamma drop size distribution for rain medium from S-band dual-polarization observations ($Z_{h,S}$, $Z_{dr,S}$, and $K_{dp,S}$). The method is based on the concept of an effective mean axis ratio versus diameter model, which is a linear relationship ($r = 1 - \beta D$). They developed an algorithm for estimating β (magnitude of the slope of the shape-size relationship) using radar measurements at S-band. For $10log_{10}(Z_{h,S}) \geq 35dBZ$, $10log_{10}(Z_{dr,S}) \geq 0.2dB$ and $K_{dp,S} \geq 0.3km^{-1}$, D_0 and N_w are retrieved as,

$$\begin{aligned}
&\beta = 2.08 Z_{h,S}^{-0.365} K_{dp,S}^{0.38} Z_{dr,S}^{0.965};\\
&D_0 = a_1 Z_{h,S}^{b_1} Z_{dr,S}^{c_1};\\
&a_1 = 0.56; \quad b_1 = 0.064; \quad c_1 = 0.024\beta^{-1.42}\\
&log_{10} N_w = a_2 Z_{h,S}^{b_2} Z_{dr,S}^{c_2};\\
&a_2 = 3.29; \quad b_2 = 0.058; \quad c_2 = -0.023\beta^{-1.389}.
\end{aligned} \tag{3.5}$$

For cases where K_{dp} is noisy and $10log_{10}Z_h$ is below 35 dBZ, the retrieval method of D_0 and N_w proposed by Bringi et al. (2002) is applied.

Using this technique, X-band radar variables ($Z_{h,X}$, $Z_{dr,X}$, $\alpha_{h,X}$, $\alpha_{dp,X}$ and $K_{dp,X}$) with a realistic scenario of precipitation event are simulated from a convective event data set observed by the CSU-CHILL radar. $Z'_{h,X}$ and $Z'_{dr,X}$ are generated by (3.4), whereas $\psi_{dp,X}$ is obtained from $K_{dp,X}$ and δ using (2.11). The simulation procedure of the DSD inversion method is shown in Fig. 3.9. Fig. 3.10 shows the S-band observations ($Z_{h,S}$, $Z_{dr,S}$) and parameters (D_0 and N_w) of DSD retrieved from S-band observations. Simulated X-band radar variables and attenuated radar variables corresponding to S-band radar measurements in Fig. 3.10 are shown in Fig. 3.11. The results show that this method can produce reasonable X-band radar variables.

Though only one type of DSD retrieval is shown, this procedure can be applied with any DSD retrieval algorithm using dual-polarization radar data.

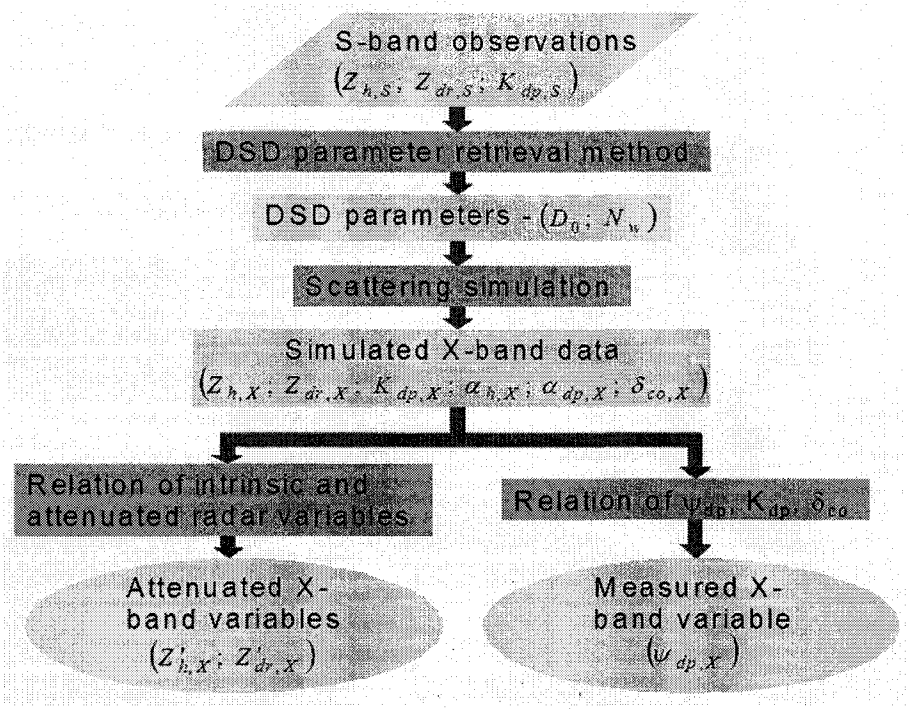

Figure 3.9: The block diagram of the DSD inversion method.

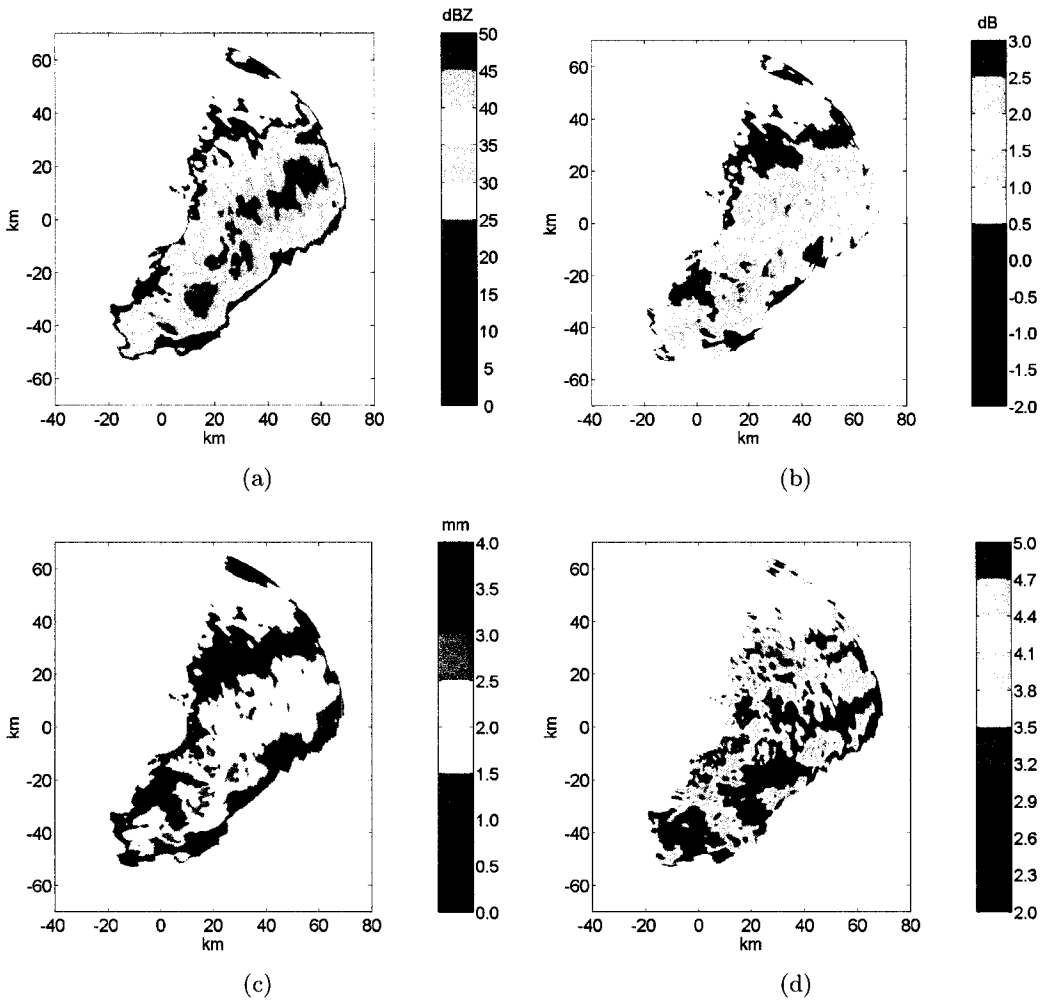

Figure 3.10: (a) Reflectivity, (b) differential reflectivity at S-band, (c) retrieved median volume diameter, and (d) retrieved normalized intercept parameter.

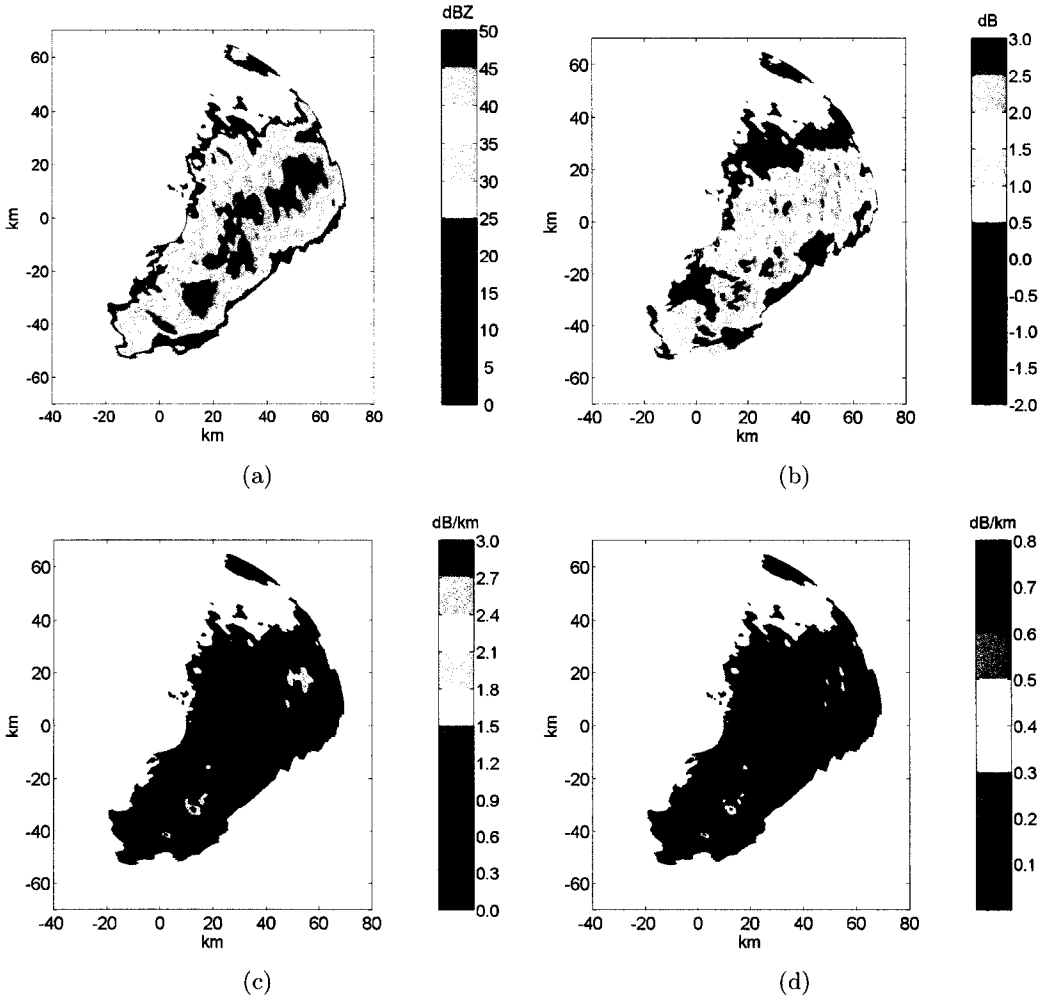

Figure 3.11: (a) Simulated reflectivity, (b) simulated differential reflectivity, (c) simulated specific attenuation, (d) simulated differential attenuation corresponding to Fig. 3.10, (e) attenuated reflectivity, (f) attenuated differential reflectivity obtained by (3.4), (g) simulated specific differential phase, and (h) differential propagation phase obtained by (2.11) at X-band.

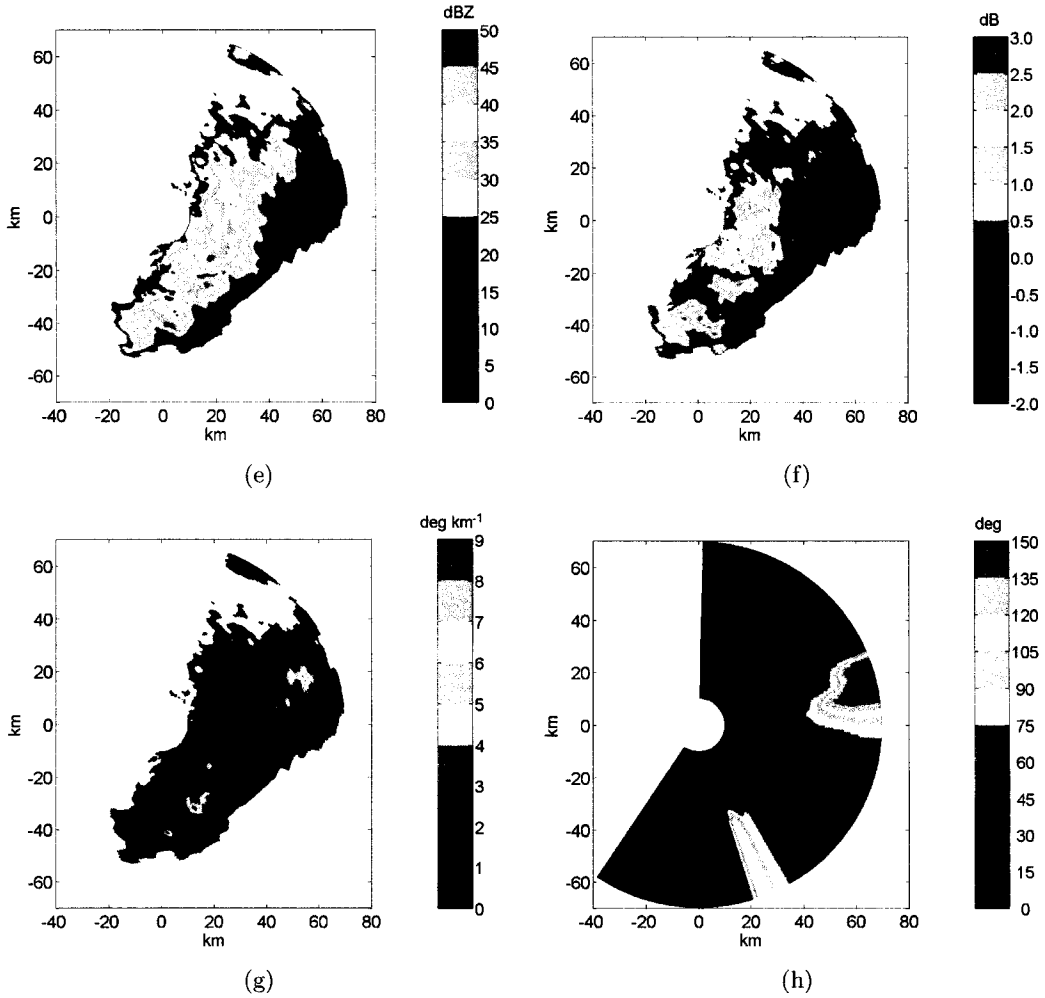

Figure 3.11: (Continued) (a) Simulated reflectivity, (b) simulated differential reflectivity, (c) simulated specific attenuation, (d) simulated differential attenuation corresponding to Fig. 3.10, (e) attenuated reflectivity, (f) attenuated differential reflectivity obtained by (3.4), (g) simulated specific differential phase, and (h) differential propagation phase obtained by (2.11) at X-band.

3.3 Comparison of three methodologies

In order to compare the proposed methodologies, radar variables at X-band are simulated using a ray profile observed by CSU-CHILL radar. Observed reflectivity, differential reflectivity, and differential phase at S-band are shown in Fig. 3.12(a), (c) and (e) as solid line, whereas simulated reflectivity, differential reflectivity, and differential phase at X-band are shown in Fig. 3.12(a), (c) and (e) according to the three methodologies. Note that the ψ_{dp} observations are filtered to remove measurements error. The corresponding attenuated reflectivity and differential reflectivity are shown in Fig. 3.12(b) and (d). From the results shown in Fig. 3.12, we can see that all of the proposed methods can simulate reasonable radar variable profiles at X-band falling within the range of observed S-band radar measurements. The empirical conversion method is based on a nearly one-to-one relation of the intrinsic radar measurements between S- and X-band. The method is simple and reliable, particularly for reflectivity and differential reflectivity. If the simulated K_{dp} or ϕ_{dp} is needed, the DSD sampling method or DSD inversion method will be useful. The DSD inversion method connects X-band variables and DSDs retrieved from S-band radar measurements. This method is more sophisticated because of the DSD inversion procedure. The DSD sampling method lies between the empirical conversion method and the full DSD inversion method.

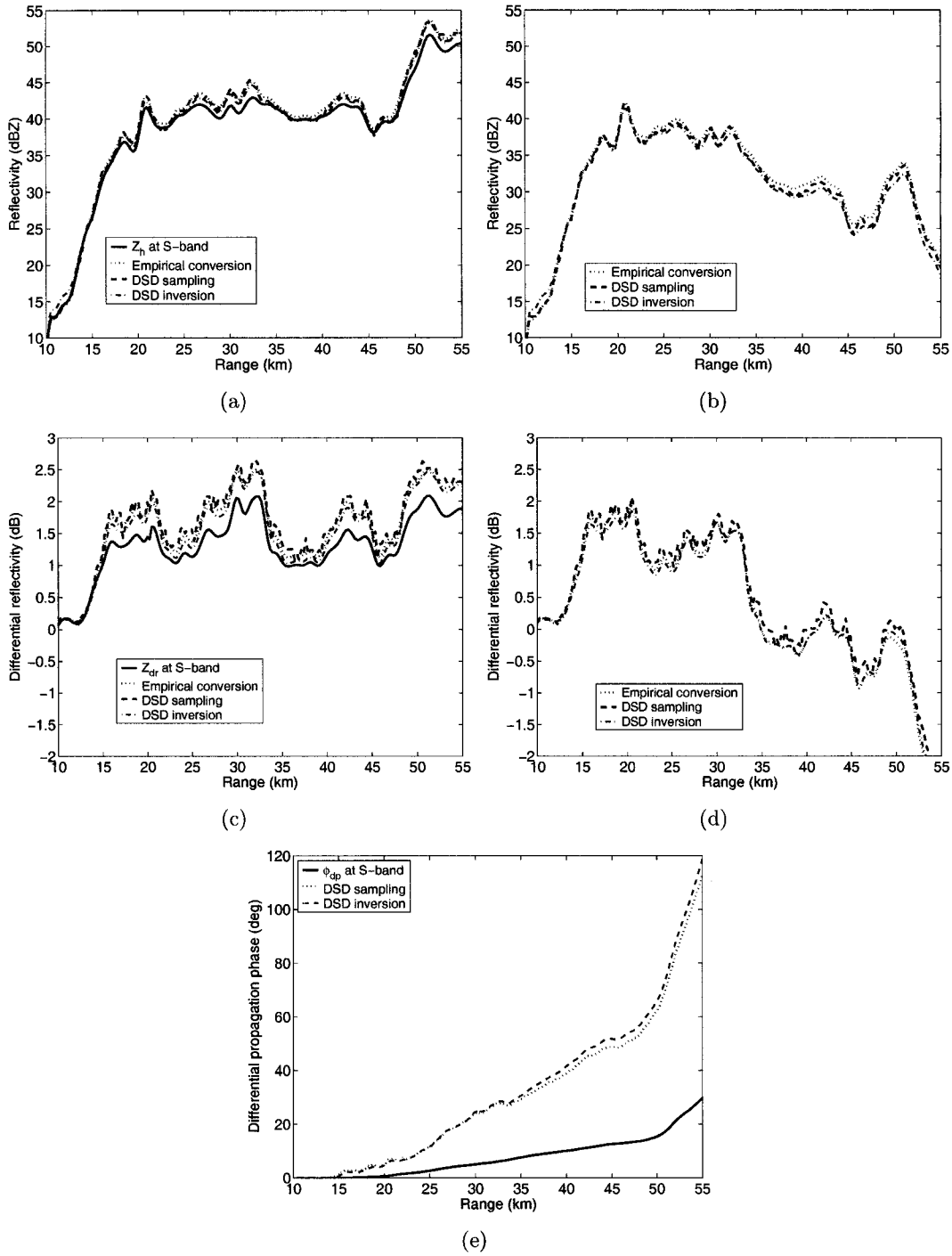

Figure 3.12: (a) Range profile of reflectivity at S-band (solid line) and simulated reflectivity at X-band using proposed methodologies, (b) corresponding attenuated reflectivity at X-band using proposed methodologies, (c) range profile of differential reflectivity at S-band (solid line) and simulated differential reflectivity at X-band, (d) attenuated differential reflectivity at X-band, and (e) differential phase profile at S-band (solid line) and the corresponding differential phase profile at X-band.

3.4 Summary and Discussion

Owing to the success of the dual-polarization methodology for attenuation correction in rain (Testud et al. 2000; Delrieu et al. 2000; Anagnostou et al. 2004; Matrosov et al. 2005; Park et al. 2005b), X-band radars are becoming more viable for targeted short-range applications. In order to validate the performance of a radar retrieval algorithm during the test phase of algorithm development, it is necessary to use empirical data based on actual precipitation events. One way to obtain that data set for higher frequencies is to simulate it from radar observations of non-attenuated or low attenuated frequencies such as S-band. This chapter presents three such methodologies to simulate "realistic" dual-polarization radar variables at X-band. The conversion methods start from S-band dual-polarization radar observations and use the fundamental microphysical properties of rainfall, namely size and shape distribution, to transform S-band into X-band variables. As a result, these methods maintain the connection between the realistic scenarios of rain events with the natural distribution of rainfall microphysical properties. The simulated X-band radar variables can give a possible scenario with a widely varying drop size distribution. These simulations have been used in evaluating the performance of X-band radar designs and algorithms in our research.

CHAPTER 4

A DUAL-POLARIZATION RAIN PROFILING ALGORITHM

4.1 Introduction

Propagation of electromagnetic waves is affected by attenuation due to rain medium. It is well known that attenuation effect caused by rain medium can be significant at frequencies higher than S-band. For quantitative applications that use reflectivity or (and) differential reflectivity, they need to be compensated for attenuation effects due to precipitation. Since Hitschfeld and Bordan (1954) proposed the attenuation correction method using the empirical relationship of reflectivity versus specific attenuation, many researchers have developed attenuation correction algorithms.

With the development of dual-polarization radar, reflectivity and differential reflectivity have been used for attenuation correction with iterative approaches (Aydin et al. 1989; Gorgucci et al. 1996). These methods are sensitive to calibration errors and unstable with large path-integrated attenuation. As an alternative approach, differential propagation phase (ϕ_{dp}) is used for attenuation correction, which is nearly linearly proportional to cumulative attenuation in typical radar frequencies (3-10 GHz) (Bringi et al. 1990). The parameterization between specific attenuation (α) and specific differential phase (K_{dp}) varies slightly with drop median diameter (D_o) or temperature resulting in errors in the ϕ_{dp} based method. This procedure is still much better than reflectivity-attenuation parameterization.

A more recent approach to attenuation correction is the rain profiling method using total path-integrated attenuation as a constraint. This method was originally

developed for spaceborne radar with path-integrated attenuation obtained by surface reference technique (Meneghini and Nakamura 1990; Marzoug and Amayenc 1994). For ground radars with dual-polarization capability, this method uses the path-integrated attenuation derived from differential phase shift as a constraint (Testud et al. 2000). This algorithm is sensitive to the α-K_{dp} parameterization. To eliminate this problem, a self-consistent algorithm combining differential phase shift and differential reflectivity constraint was proposed by Bringi et al. (2001). One disadvantage of the rain profiling algorithm is that it assumes that intercept parameter (N_w) of drop size distribution is constant along a path. In this chapter, a general dual-polarization rain profiling algorithm (referred henceforth as DRPA) is proposed. Reflectivity and differential reflectivity together can successfully track variabilities in D_0 and N_w (Lim and Chandrasekar 2006). Therefore, the proposed algorithm can eliminate the assumption that N_w is constant along a path. In addition, a new self-consistent method corresponding to the proposed dual-polarization rain profiling algorithm is also developed.

This chapter is organized as follows. In Section 4.2, the rain profiling algorithm and self-consistent method are described briefly. The new DRPA is presented in Section 4.3 and the corresponding self-consistent method is outlined in Section 4.4. The evaluation of these algorithms is described in Section 4.5 and the important results are summarized in Section 4.6.

4.2 Background

4.2.1 Rain profiling algorithm (RPA) and self-consistent method (SC-RPA)

Rain profiling algorithms are based on the principle of coupling the specific attenuation and reflectivity proposed by Hitschfeld and Bordan (1954). The specific attenuation at horizontal polarization ($\alpha_h(r); dBkm^{-1}$) can be approximately parameterized in terms of reflectivity at horizontal polarization ($Z_h(r); mm^6m^{-3}$) by a

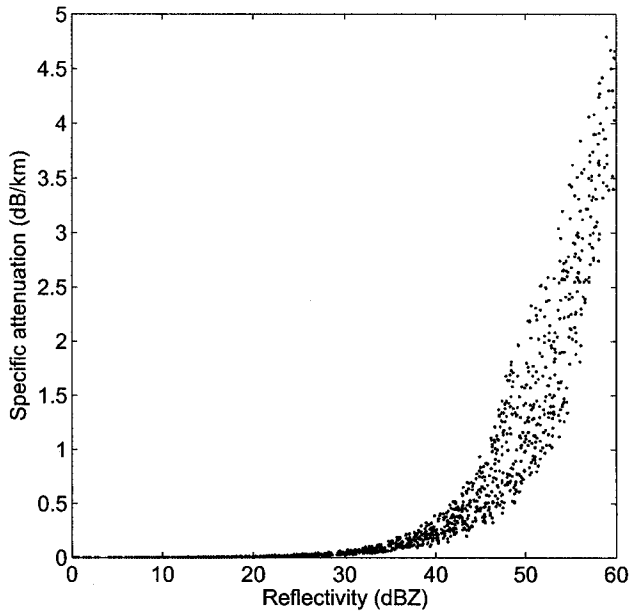

Figure 4.1: A scatter plot of reflectivity versus specific attenuation at X-band.

power law as

$$\alpha_h(r) = a[Z_h(r)]^b. \tag{4.1}$$

Fig. 4.1 shows the scatter plot of reflectivity versus specific attenuation at X-band. Similarly, attenuation correction procedures are also based on a linear parameterization between α_h and $K_{dp}(\deg km^{-1})$ introduced by Bringi et al. (1990) as

$$\alpha_h(r) = \gamma K_{dp}(r). \tag{4.2}$$

Fig. 4.2 shows the scatter plot of specific differential phase versus specific attenuation at X-band. In the presence of attenuation, measured reflectivity ($Z'_h(r)$) can be defined in terms of intrinsic reflectivity (unattenuated) and specific attenuation as

$$Z'_h(r) = Z_h(r)e^{-0.46\int_0^r \alpha_h(s)ds}. \tag{4.3}$$

A governing integral equation for reflectivity profile can be formed from (4.1) - (4.3) with the assumption that a and b are constant along a path. After modest algebraic

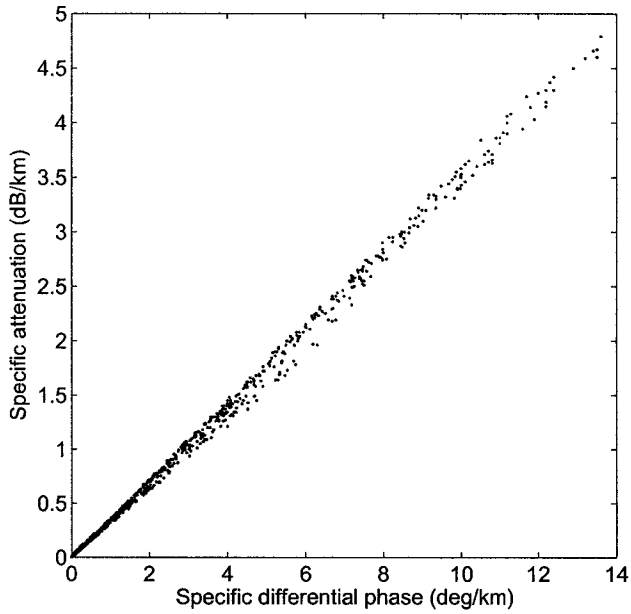

Figure 4.2: A scatter plot of specific differential phase versus specific attenuation at X-band.

manipulation, a solution of specific attenuation from starting range (r_0) of precipitation echo to last range (r_m) is obtained as (Bringi and Chandrasekar 2001)

$$\begin{aligned} \hat{\alpha}_h(r) &= \frac{[Z'_h(r)]^b (10^{0.1b\hat{A}_h(r_0;r_m)} - 1)}{I(r_0;r_m) + (10^{0.1b\hat{A}_h(r_0;r_m)} - 1) I(r;r_m)}; \\ I(r_0;r_m) &= 0.46b \int_{r_0}^{r_m} [Z'_h(r)]^b dr; \end{aligned} \tag{4.4}$$

where $\hat{A}_h(r_0;r_m)$ is the two-way cumulative attenuation from range r_0 to r_m and $\hat{\alpha}_h(r)$ indicates the retrieved specific attenuation (henceforth variables with "^" indicate retrieved estimates). For horizontal-looking radars, this two-way cumulative attenuation can be obtained from differential propagation phase (ϕ_{dp}) as

$$\hat{A}_h(r_0;r_m) = 2\int_{r_0}^{r_m} \alpha_h(r)dr = \gamma(\phi_{dp}(r_m) - \phi_{dp}(r_0)). \tag{4.5}$$

Using $\hat{\alpha}_h(r)$, differential attenuation ($\hat{\alpha}_{dp}(r)$) can be retrieved by the linear relation between $\hat{\alpha}_h$ and $\hat{\alpha}_{dp}$ as

$$\hat{\alpha}_{dp}(r) = \kappa\hat{\alpha}_h(r). \tag{4.6}$$

One of the potential limitations of the rain profiling method is the assumption of a constant γ. To overcome this problem, the self-consistent solution was proposed by Bringi et al. (2001). The optimal value of γ corresponding to each ray profile can be obtained by comparing the measured differential propagation phase profile ($\psi_{dp}(r)$) and integrated retrieved specific attenuation as

$$\chi(\gamma) = \sum_{j=1}^{N} \left| \psi_{dp}(r_j) - 2 \sum_{i=1}^{j} \frac{\hat{\alpha}_h(r_i;\gamma)}{\gamma} dr \right| \tag{4.7}$$

where i and j indicate range bin and dr is the range of resolution volume. After reflectivity correction with optimal value of γ, κ is optimized with a relation between Z_h and differential reflectivity (Z_{dr}) derived from scattering simulation based on drop size distribution (DSD). The details of the self-consistent method are described by Bringi et al. (2001).

4.2.2 The impact of backscatter differential phase

For the use of the rain profiling algorithm and the self-consistent method constrained by ϕ_{dp}, backscatter differential phase (δ) should be considered, especially at higher frequencies such as X-band. The measured differential propagation phase (ψ_{dp}) is the combination of backscatter differential phase and intrinsic differential propagation phase (ϕ_{dp}) as (Bringi and Chandrasekar 2001)

$$\psi_{dp} = \phi_{dp} + \delta. \tag{4.8}$$

At lower frequencies such as S-band, δ is negligible. However, at higher frequencies such as X-band, δ can be significant. Fig. 4.3 shows the scatter plot of D_0 versus δ at X-band. From Fig. 4.3, we can recognize that δ at X-band can be of the order of 4-12 degrees in moderate and heavy rain.

The most commonly used method to separate δ and ϕ_{dp} from ψ_{dp} is the iterative filtering technique proposed by Hubbert and Bringi (1995). This method estimates

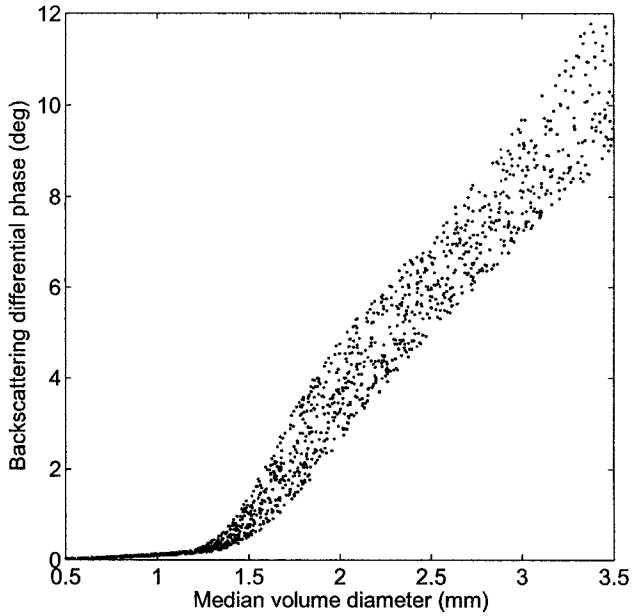

Figure 4.3: A scatter plot of median volume diameter (D_o) versus backscatter differential phase (δ), at X-band.

non-zero δ superposed on a monotonic increasing ϕ_{dp} range profile. However this procedure may not be able to filter out gradually varying δ in rain paths.

4.3 Dual-Polarization Rain Profiling Algorithm (DRPA)

Specific attenuation at horizontal polarization ($\alpha_h(r)$; $dBkm^{-1}$) and at vertical polarization ($\alpha_v(r)$; $dBkm^{-1}$) can be parameterized with reflectivity at horizontal polarization ($Z_h(r)$; mm^6m^{-3}), reflectivity at vertical polarization ($Z_v(r)$; mm^6m^{-3}), and differential reflectivity ($Z_{dr}(r)$) by means of a power law as

$$\begin{aligned} \alpha_h(r) &= a_1[Z_h(r)]^{b_1}[Z_{dr}(r)]^{c_1}; \\ \alpha_v(r) &= a_2[Z_v(r)]^{b_2}[Z_{dr}(r)]^{c_2}. \end{aligned} \tag{4.9}$$

From the theoretical computations for widely varying drop size distribution, it can be shown that b_1, b_2, c_1, and c_2 are nearly constant whereas a_1 and a_2 depend on temperature. The scatter plot of intrinsic specific attenuation and retrieved specific attenuation given by (4.9) is shown in Fig. 4.4 for widely varying DSD ($0.5 \leq D_0 \leq 3.5\ mm$, $3 \leq log_{10}N_w \leq 5$ and $-1 < \mu \leq 4$ for $R < 300\ mmh^{-1}$ and $Z_h < 60$

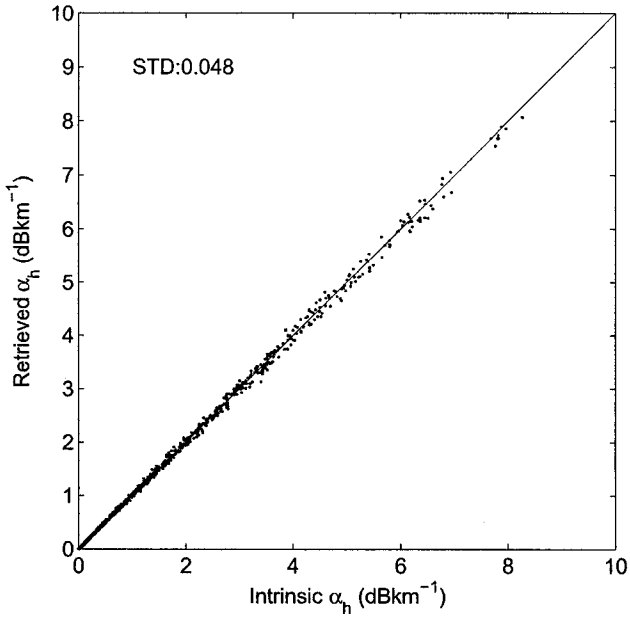

Figure 4.4: A scatter plot of intrinsic specific attenuation versus retrieved specific attenuation by (4.9).

dBZ). The data were obtained by scattering simulation using the ABC model at a temperature of $10°C$. For comparison with a power law relationship of α_h - Z_h, the scatter plot of intrinsic specific attenuation and retrieved specific attenuation by $\alpha_h = a(N_w)^{(1-b)}(Z_h)^b$ is shown in Fig. 4.5. The results of Fig. 4.4 show that (4.9) provides a good estimate of specific attenuation. A linear relationship between $\alpha_h(r)$ and $K_{dp}(r)$ can be assumed with coefficient, γ as

$$\alpha_h(r) = \gamma K_{dp}(r). \tag{4.10}$$

Similarly $\alpha_h(r)$ and $\alpha_{dp}(r)$ can be parameterized with coefficient, κ as

$$\alpha_{dp}(r) = \kappa \alpha_h(r). \tag{4.11}$$

The scatter plot of α_h versus α_{dp} is shown in Fig. 4.6. Note that a power law relationship can reduce the variability of the α_h - α_{dp} relation. However a linear relationship can adequately express the α_h - α_{dp} relationship with reliable confidence. Fig. 4.7 shows the scatter plot of intrinsic α_{dp} versus retrieved α_{dp} using a linear

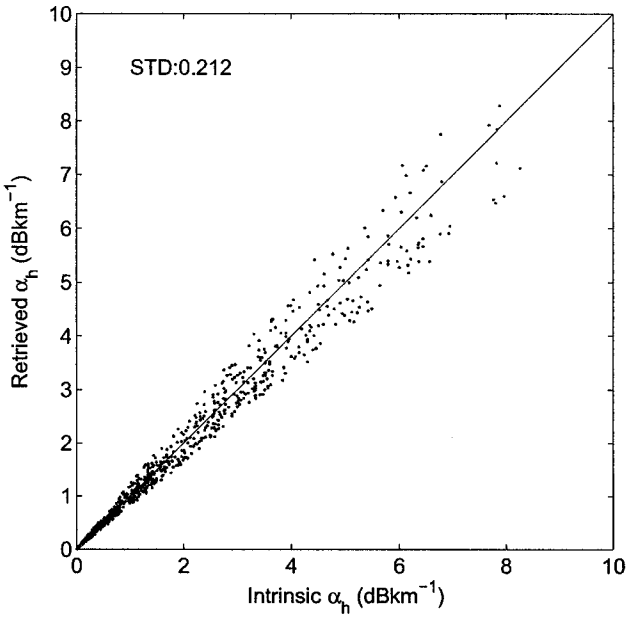

Figure 4.5: A scatter plot of intrinsic specific attenuation versus retrieved specific attenuation by power law relationship.

relationship as (4.11), whereas Fig. 4.8 shows the scatter plot of intrinsic α_{dp} versus retrieved α_{dp} using a power law relationship as $\alpha_{dp} = p(N_w)^{(1-q)}(\alpha_h)^q$. From the results of Fig. 4.7, we can see that a linear relation of α_h - α_{dp} is reasonable. For an inhomogeneous rain path, attenuated reflectivity at horizontal polarization ($Z'_h(r)$), attenuated reflectivity at vertical polarization ($Z'_v(r)$), and attenuated differential reflectivity ($Z'_{dr}(r)$) can be expressed as

$$\begin{aligned} Z'_h(r) &= Z_h(r)e^{-0.46\int_0^r \alpha_h(s)ds}; \\ Z'_v(r) &= Z_v(r)e^{-0.46\int_0^r \alpha_v(s)ds}; \\ Z'_{dr}(r) &= Z_{dr}(r)e^{-0.46\int_0^r \alpha_{dp}(s)ds}. \end{aligned} \tag{4.12}$$

After modest algebraic manipulation with (4.9)-(4.12) assuming that a_1, a_2, b_1, b_2, c_1, and c_2 are constant along a path, solutions for integral equations relating specific attenuation at horizontal and vertical polarization can be expressed as (for detailed

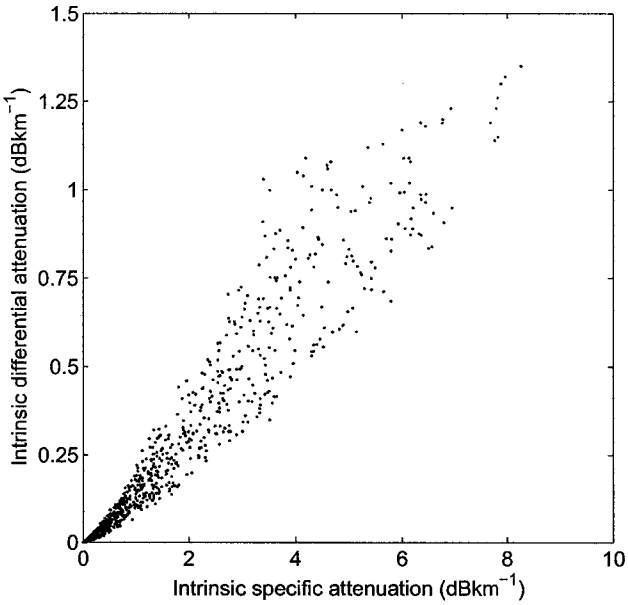

Figure 4.6: A scatter plot of intrinsic specific attenuation versus intrinsic differential attenuation.

derivation, please see Appendix A),

$$\begin{aligned}\hat{\alpha}_h(r) &= \frac{[Z'_h(r)]^{b_1}[Z'_{dr}(r)]^{c_1}(10^{0.1\gamma(b_1+\kappa c_1)\Delta\phi_{dp}(r_0;r_m)}-1)}{I_h(r_0;r_m)+(10^{0.1\gamma(b_1+\kappa c_1)\Delta\phi_{dp}(r_0;r_m)}-1)I_h(r;r_m)};\\ I_h(r_0;r_m) &= 0.46(b_1+\kappa c_1)\int_{r_0}^{r_m}[Z'_h(r)]^{b_1}[Z'_{dr}(r)]^{c_1}dr\end{aligned} \tag{4.13}$$

and

$$\begin{aligned}\hat{\alpha}_v(r) &= \frac{[Z'_v(r)]^{b_2}[Z'_{dr}(r)]^{c_2}(10^{0.1\gamma(1-\kappa)(b_2+\frac{\kappa}{1-\kappa}c_2)\Delta\phi_{dp}(r_0;r_m)}-1)}{I_v(r_0;r_m)+(10^{0.1\gamma(1-\kappa)(b_2+\frac{\kappa}{1-\kappa}c_2)\Delta\phi_{dp}(r_0;r_m)}-1)I_v(r;r_m)};\\ I_v(r_0;r_m) &= 0.46(b_2+\frac{\kappa}{1-\kappa}c_2)\int_{r_0}^{r_m}[Z'_v(r)]^{b_2}[Z'_{dr}(r)]^{c_2}dr.\end{aligned} \tag{4.14}$$

From the specific attenuation at horizontal and vertical polarization, we can obtain differential attenuation as

$$\hat{\alpha}_{dp} = \hat{\alpha}_h - \hat{\alpha}_v. \tag{4.15}$$

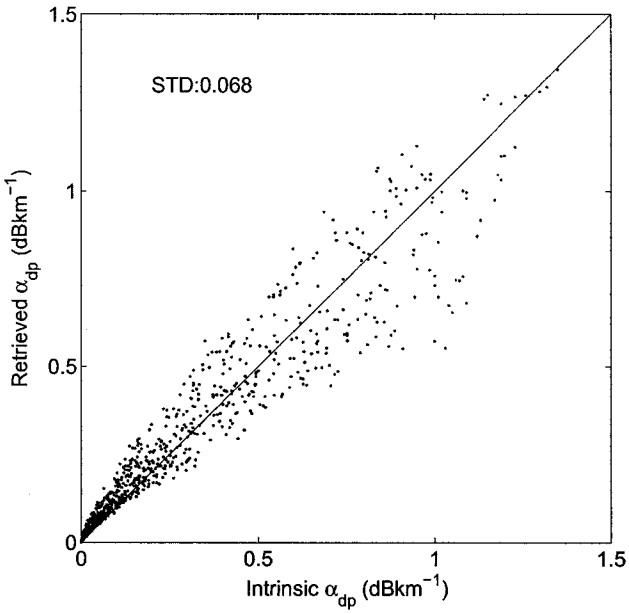

Figure 4.7: A scatter plot of intrinsic differential attenuation versus retrieved differential attenuation by (4.11).

Once $\hat{\alpha}_h(r)$ and $\hat{\alpha}_{dp}$ are calculated at each range from r_0 to r_m, the $\hat{Z}_h(r)$ and $\hat{Z}_{dr}(r)$ can be corrected as

$$\begin{aligned} 10log_{10}[\hat{Z}_h(r)] &= 10log_{10}[Z'_h(r)] + 2\int_{r_0}^{r} \hat{\alpha}_h(s)ds; \\ 10log_{10}[\hat{Z}_h(r)] &= 10log_{10}[Z'_h(r)] + 2\int_{r_0}^{r} \hat{\alpha}_h(s)ds; \\ 10log_{10}[\hat{Z}_{dr}(r)] &= 10log_{10}[Z'_{dr}(r)] + 2\int_{r_0}^{r} \hat{\alpha}_{dp}(s)ds. \end{aligned} \qquad (4.16)$$

Similar to [illegible] path to obtain total two-way cumulative attenuation from range r_0 to r_m. However, by introducing Z'_{dr} in the attenuation correction procedure, DRPA can distribute specific attenuation more properly from total cumulative attenuation along a ray.

4.4 Self-Consistent DRPA Method for Attenuation Correction

In DRPA, six coefficients (b_1, b_2, c_1, c_2, γ, κ) are used to estimate the specific attenuation and differential attenuation. From theoretical simulations, it is clear that b_1, b_2, c_1, and c_2 can be assumed to be constant for a given frequency. However γ and κ may be sensitive to temperature and drop axis ratio versus diameter relation.

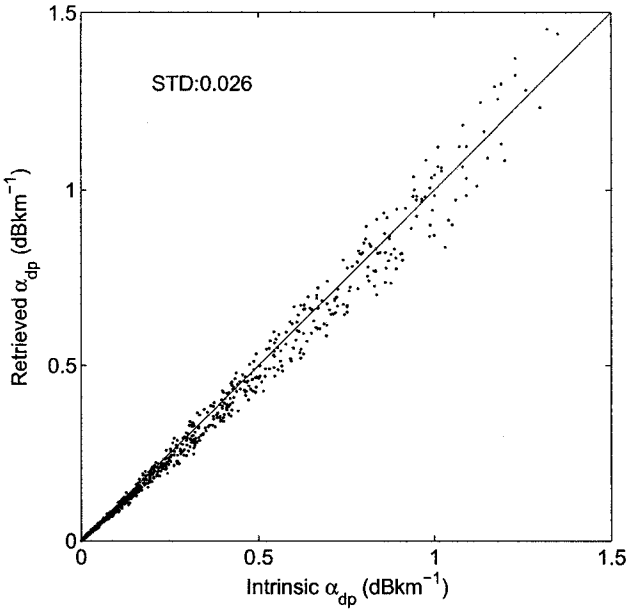

Figure 4.8: A scatter plot of intrinsic differential attenuation versus retrieved differential attenuation by power law relationship.

This section presents the optimization procedure to obtain coefficients, γ and κ. For rain profiling algorithm, Bringi et al. (2001) proposed a self-consistent method to optimize γ and κ. In this method, first γ is optimized to estimate $\hat{\alpha}_h(r)$ with ϕ_{dp} constraint and then κ is optimized to estimate $\hat{\alpha}_{dp}(r)$ with Z_{dr} constraint. In the proposed attenuation correction algorithm, γ and κ are optimized simultaneously by two comparison processes to fine tune the values of γ and κ. One of the comparison processes is to use retrieved $\hat{\alpha}_h$ and the other is to use retrieved $\hat{\alpha}_v$. In addition, application of this procedure at high frequency such as X-band needs to pay attention to δ. To use the self-consistent method, the impact of δ superposed on ϕ_{dp} needs to be considered. From the theoretical analysis, δ is nearly linearly related to Z_{dr} (linear scale) as shown in Fig. 4.9.

A differential phase profile (ψ^t_{dp}) can be built from ϕ_{dp} estimated from integrated attenuation and backscatter differential phase retrieved from $\hat{Z}_{dr}$. For each γ and κ,

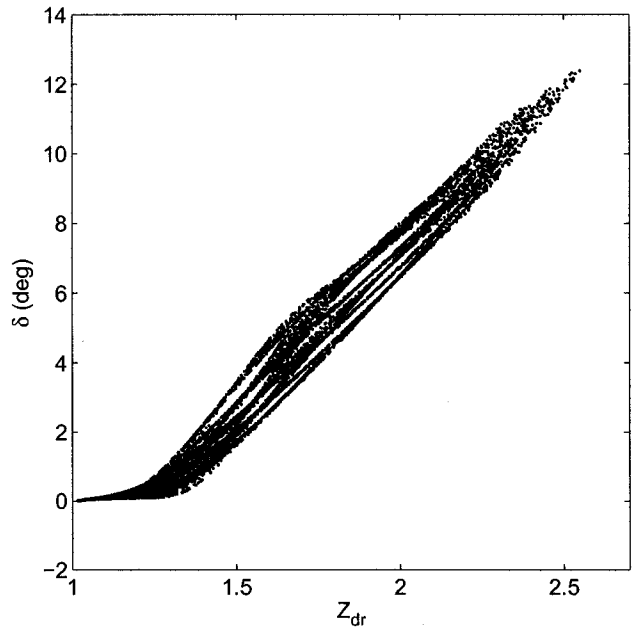

Figure 4.9: Scatter plot of differential reflectivity (linear scale) versus backscatter differential phase.

a reconstructed differential phase profile ($\psi^t_{dp}(r;\gamma;\kappa)$) can be computed as

$$\begin{aligned}
\psi^{t_1}_{dp}(r;\gamma;\kappa) &= 2\int_{r_0}^{r} \frac{\hat{\alpha}_h(s;\gamma;\kappa)}{\gamma} ds + \hat{\delta}; \\
\psi^{t_2}_{dp}(r;\gamma;\kappa) &= 2\int_{r_0}^{r} \frac{\hat{\alpha}_v(s;\gamma;\kappa)}{\gamma_{\frac{\kappa}{1-\kappa}}} ds + \hat{\delta}; \\
\gamma_{min} \leq \gamma \leq \gamma_{max}; &\quad \kappa_{min} \leq \kappa \leq \kappa_{max}
\end{aligned} \tag{4.17}$$

and

$$\begin{aligned}
\hat{\delta} &= 0; && \hat{Z}_{dr} < 1.25 \\
&= -11.5 + 9.35\hat{Z}_{dr}; && \hat{Z}_{dr} \geq 1.25.
\end{aligned} \tag{4.18}$$

$\hat{\alpha}_h(s;\gamma;\kappa)$ and $\hat{\alpha}_v(s;\gamma;\kappa)$ are obtained from (4.13)-(4.14) respectively for each value of γ and κ. The reconstructed differential phase profile is compared against the measured differential phase profile to optimize γ and κ. The bounds (γ_{min}, γ_{max}, κ_{min}, and κ_{max}) can be obtained from theoretical considerations. The variability of γ and κ was evaluated for various shape models as well as temperatures between $0 - 20°C$.

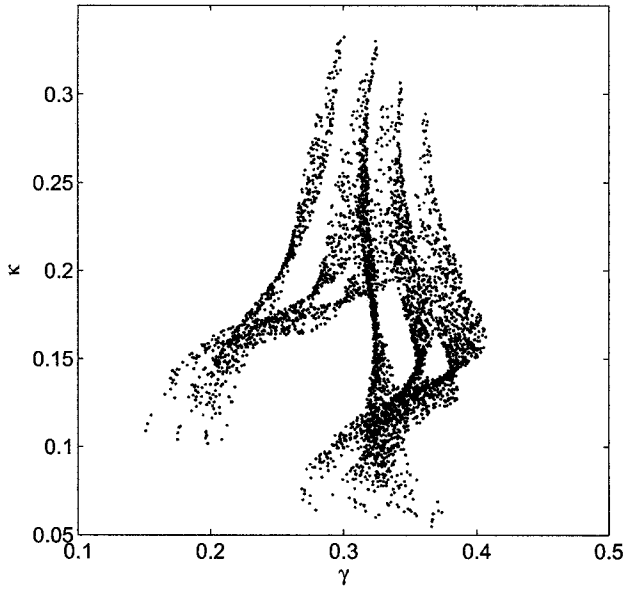

Figure 4.10: A scatter plot of γ versus κ.

This analysis yielded $\gamma \in [0.15, 0.4]$ and $\kappa \in [0.050.35]$. Fig 4.10 shows scatter plot of γ versus κ corresponding to various shape models as well as temperatures between $0 - 20°C$. After computing the differential phase from retrieved attenuation and $\hat{\delta}$, the reconstructed differential propagation phase is compared with observed ψ_{dp}. The two processes to compare ψ_{dp} and ψ_{dp}^{t} can be described as

$$\begin{aligned} \chi_1 &= \frac{1}{N}\sum_{j=1}^{N} |\psi_{dp}(r_j) - \psi_{dp}^{t_1}(r_j;\gamma;\kappa)|; \\ \chi_2 &= \frac{1}{N}\sum_{j=1}^{N} |\psi_{dp}(r_j) - \psi_{dp}^{t_2}(r_j;\gamma;\kappa)|; \end{aligned} \tag{4.19}$$

where $r_1 \equiv r_0$ and $r_N \equiv r_m$. Fig. 4.12(a) and (b) show an example of χ_1 and χ_2 along a ray, respectively. In Fig. 4.12 "o"s indicate the optimal values of κ and γ.

It is well known that reflectivity and differential reflectivity are located in a limited region in a $Z_h - Z_{dr}$ plane. Therefore, we can bound the region where $\hat{Z}_h(r_m)$ and

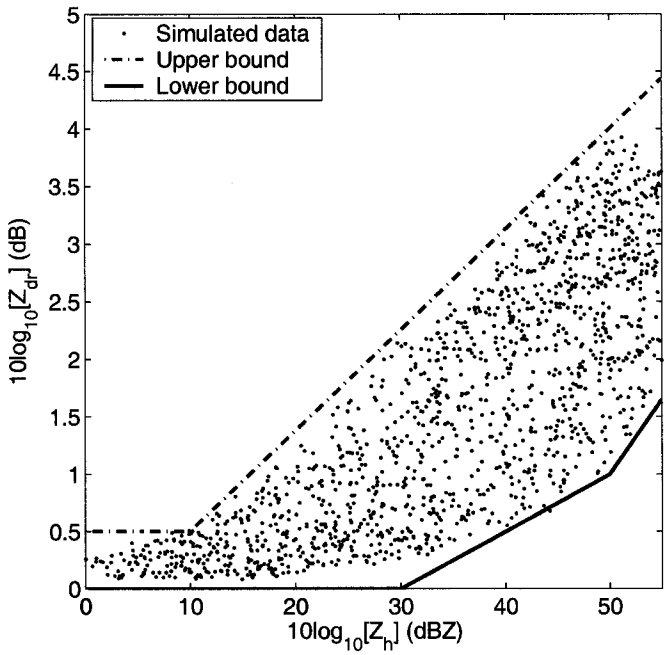

Figure 4.11: Boundary condition of differential reflectivity according to reflectivity.

$\hat{Z}_{dr}(r_m)$ can lie as shown in Fig. 4.11. The boundary condition can be expressed as

$$
\begin{aligned}
&10log_{10}(\hat{Z}_{dr}^{lb}(r_m)) \\
&\quad = 0 && 10log_{10}(\hat{Z}_h(r_m)) \leq 30dBZ \\
&\quad = 0.05(10log_{10}(\hat{Z}_h(r_m)) - 30); && 30 < 10log_{10}(\hat{Z}_h(r_m)) \leq 50dBZ \\
&\quad = 0.13(10log_{10}(\hat{Z}_h(r_m)) - 50) + 1; && 10log_{10}(\hat{Z}_h(r_m)) > 50dBZ
\end{aligned}
\tag{4.20a}
$$

$$
\begin{aligned}
&10log_{10}(\hat{Z}_{dr}^{ub}(r_m)) \\
&\quad = 0.5; && 10log_{10}(\hat{Z}_h(r_m)) \leq 10dBZ \\
&\quad = 0.0875(10log_{10}(\hat{Z}_h(r_m)) - 10) + 0.5; && 10log_{10}(\hat{Z}_h(r_m)) > 10dBZ
\end{aligned}
\tag{4.20b}
$$

where lb indicates the lower boundary and ub is the upper boundary. Using the boundary condition, the choice of γ and κ can be limited. From the constrained γ and κ, the mean values of γ and κ can be selected as optimal values of γ and κ (γ_1, γ_2, κ_1, and κ_2) for the two processes from those that remain within the boundary.

Finally, the optimal value of γ_{opt} and κ_{opt} can be selected by the mean values of γ and κ obtained from the comparison processes. Fig. 4.12 shows the difference of

ϕ_{dp} and ϕ^t_{dp} applied with boundary condition. In Fig. 4.12, the white lines indicate the boundary condition and "x"s indicate the optimal value of γ and κ in terms of χ_1 and χ_2. Once the optimal values of γ and κ are estimated, the reflectivity and the differential reflectivity can be retrieved as,

$$\begin{aligned} 10log_{10}(\hat{Z}_h(r;\gamma_{opt};\kappa_{opt})) &= 10log_{10}(Z'_h(r)) + 2\int_{r_0}^{r}\hat{\alpha}_h(s;\gamma_{opt};\kappa_{opt})ds; \\ 10log_{10}(\hat{Z}_{dr}(r;\gamma_{opt};\kappa_{opt})) &= 10log_{10}(Z'_{dr}(r)) + 2\int_{r_0}^{r}\hat{\alpha}_{dp}(s;\gamma_{opt};\kappa_{opt})ds. \end{aligned} \tag{4.21}$$

Fig. 4.13 shows an example of results retrieved by the SC-DRPA with the optimal values of γ_{opt} and κ_{opt}. It can be seen from Fig. 4.13 that SC-DRPA provides an improvement over the SC-RPA algorithm.

4.5 Evaluation

Attenuation correction algorithms can be evaluated by two methods. One is to use internal validity such as plotting K_{dp} against corrected and uncorrected radar observations (Bringi et al. 2001). The other method is based on simulation, where the profiles of X-band observations are simulated. Chandrasekar et al. (2004a) have developed a method to simulate X-band observations based on S-band measurements. One of the main advantages of this method is that the natural variability of DSD in precipitation is maintained in the process, as opposed to using synthetic profiles. This method also provides an ability to quantify the performance metrics.

In this section, the proposed DRPA as well as SC-DRPA algorithms are evaluated by using data simulated by the DSD inversion method from S-band radar observations. The X-band radar observations with realistic scenario of precipitation event are simulated from a convective event data set observed by CSU-CHILL radar on July 19, 2000 during the Severe Thunderstorm Electrification and Precipitation Study (STEPS). The simulated data set is generated by the shape model proposed by Bringi et al. (2003), which combines the Andsager et al. (1999) fit for region of $1 \leq D \leq 4mm$ and the Beard and Chuang (1987) model for the region of $D < 1$ and

$D > 4mm$. The attenuated observations can be obtained from simulated data by (3.4). Simulated and attenuated X-band radar observations are shown in Fig. 3.11.

The evaluation is primarily done by comparing the attenuation estimates. This is done by comparing the intrinsic and attenuation corrected profiles. The evaluation process is carried out under three scenarios. The first one corresponds to radar observations, which do not include the impact of δ and signal fluctuations (Case I). Case I primarily evaluates the "physics" of the algorithm.

DRPA uses Z_{dr} measurements in addition to Z_h. Each measurement comes with its errors. Therefore, the improvement accomplished by using Z_{dr} must overcome the errors brought by the Z_{dr} measurement to be useful. The performance of the attenuation correction algorithm can be affected by random signal fluctuation errors. Typically, in a well-maintained radar, the signal fluctuation errors can be less than 1 dBZ standard deviation for Z_h, 0.2 dB standard deviation for Z_{dr} and 3 deg standard deviation for ϕ_{dp}. For the performance evaluation in the presence of signal fluctuation errors, Gaussian random errors with a standard deviation of 1 dBZ and zero mean are introduced to the measured reflectivity, while for measured differential reflectivity, random errors with a standard deviation of 0.2 dB and zero mean are added. Gaussian random errors with a standard deviation of 3 deg and zero mean are also introduced for measured differential phase. These measurements, along with their simulated measurement errors, are used for evaluation in this second scenario (Case II).

Attenuation correction algorithms constrained by ψ_{dp} can be affected by random signal fluctuation errors as well as δ. As shown in (4.8), the measured differential phase ψ_{dp} is the combination of backscatter differential phase δ and intrinsic differential propagation phase ϕ_{dp}. In higher frequencies such as X-band, the impact of δ can be significant. Therefore, it is necessary to test the impact of δ for the performance evaluation and those are presented in the third scenario (Case III). The impact of δ is introduced according to Fig. 4.3 and ϕ_{dp} is perturbed by δ in the range profiles.

The performance of the attenuation correction algorithm can be evaluated in terms of a standard deviation and mean bias of difference between retrieved observations and intrinsic observations along the profiles. The errors can be defined as

$$\begin{aligned} \varepsilon_A(r) &= A_h(r) - \hat{A}_h(r); \\ \varepsilon_{DA}(r) &= A_{dp}(r) - \hat{A}_{dp}(r) \end{aligned} \tag{4.22}$$

where $A_h(r)$ is two-way cumulative attenuation and A_{dp} is two-way cumulative differential attenuation.

4.5.1 Performance comparison of RPA and DRPA

For evaluation of DRPA, the values of γ and κ need to be selected. γ and κ are sensitive to the temperature and drop shape model. From the ABC model, the values of γ and κ are obtained as 0.345 and 0.14, at a temperature of $10°C$. For Case I, the scatter plots of intrinsic α_h versus retrieved $\hat{\alpha}_h$ using RPA with fixed γ and DRPA with fixed γ and κ, are shown in Fig. 4.14(a) and (b), whereas the scatter plot of intrinsic α_{dp} versus retrieved $\hat{\alpha}_{dp}$ using RPA and DRPA are shown in Fig. 4.14(c) and (d), respectively. The results of Fig. 4.14 show that DRPA can retrieve specific attenuation more properly than RPA. The average standard deviation error and mean bias of $\varepsilon_A(r)$ and $\varepsilon_{DA}(r)$ using RPA and DRPA are shown in Fig. 4.15 as a function of range for Cases I, II and III. From the results of Fig. 4.15, we can see that DRPA retrieves radar observations better than RPA, uniformly for all situations.

Radar design specifications are typically provided such that the error in reflectivity should be within 1 dB, and differential reflectivity stays within 0.2 dB. If the 1 dB error limit is the criterion, then the percentage of time attenuation corrected reflectivity stays within 1 dB can be evaluated as a metric. The percentages for which $|A_h - \hat{A}_h| < 1$ dB are shown as a function of range in Fig. 4.16(a), whereas the percentages for which $|A_{dp} - \hat{A}_{dp}| < 0.2$ dB are shown as a function of range in Fig. 4.16(b). The results of Fig. 4.16 show that DRPA performs better than RPA, specially at a distance farther than 20 km from the radar (note that high-intensity

echoes are from 20 km from radar). Attenuation correction is done to reduce the reflectivity retrieval errors.

The percentages for which $|A_h - \hat{A}_h| < 1\ dB$ and $|A_{dp} - \hat{A}_{dp}| < 0.2\ dB$ under the conditions that $A_h > 10\ dB$ and $A_{dp} > 2\ dB$ are listed in Table 4.1. The 10 dB threshold for attenuation and 2 dB threshold for differential attenuation are used to correspond to 10% errors with 1 dB and 0.2 dB accuracy requirement for Z_h and Z_{dr}. By comparing the results of Table 4.1, we can see that for the storm studied, the RPA is able to maintain 84% of the attenuation corrected data within 1 dB, whereas the DRPA improves that figure to 97%. However, when the influence of the backscattering phase shift and measurement errors are included in the simulation, this number falls to 68% for RPA and 85% for DRPA. Both algorithms use the ψ_{dp} constrained method at the last range. Therefore, performance of both algorithms is affected by the impact of δ only at the last range. It is clear from the results of Table 4.1 that both RPA and DRPA are not strongly affected by δ. The performance of RPA and DRPA can be affected more by signal fluctuations than δ.

Table 4.1: Comparison of performance between RPA and DRPA: Case I - with radar observations without measurement error, Case II - with the signal fluctuations, and Case III - with the impact of δ and signal fluctuations. The percentages for which $|A_h - \hat{A}_h| < 1$ dB and $|A_{dp} - \hat{A}_{dp}| < 0.2\ dB$ under the conditions that $A_h > 10\ dB$ and $A_{dp} > 2\ dB$. Fixed values of γ and κ obtained from the ABC model are used.

Case	RPA		DRPA	
	$f(\varepsilon_A)$	$f(\varepsilon_{DA})$	$f(\varepsilon_A)$	$f(\varepsilon_{DA})$
Case I	84.0	53.6	96.7	63.1
Case II	68.2	51.5	84.8	64.2
Case III	68.2	51.8	85.2	62.7

4.5.2 Performance comparison of SC-RPA and SC-DRPA

RPA and DRPA assume the fixed values of γ and κ to retrieve radar observations. However, in convective storms the values of γ and κ may vary slightly. Deviation in γ and κ values can worsen the performance of RPA and DRPA. A self-consistency

algorithm is used to correct for the deviation in γ and κ. The self-consistency algorithms are evaluated as the following. The data set was simulated by the ABC model, whereas the RPA and DRPA were built by fixed γ and κ values obtained from the Beard and Chuang model ($\gamma = 0.3$ and $\kappa = 0.16$). The average standard deviation error and mean bias of $\varepsilon_A(r)$ and $\varepsilon_{DA}(r)$ by RPA and DRPA are shown in Fig. 4.17 as a function of range for Case I. The results of Fig. 4.17 show clearly that if γ and κ values are not chosen properly, retrieved observations from both RPA and DRPA can be biased. From these results, we can see that self-consistent methods are needed to improve the attenuation correction. SC-RPA and SC-DRPA are evaluated for all situations (Cases I-III). SC-RPA and SC-DRPA are applied when the difference of ψ_{dp} over a rain cell is greater than 10 *deg*. Otherwise, fixed values obtained from Beard and Chuang model are used. The average standard deviation error and mean bias of $\varepsilon_A(r)$ and $\varepsilon_{DA}(r)$ using SC-RPA and SC-DRPA are shown in Fig. 4.18 as a function of range for Case I. From the results of Fig. 4.18, we can see that SC-DRPA can reduce standard deviation error and bias significantly, and works better than SC-RPA. For all cases, the percentages for which $|A_h - \hat{A}_h| < 1\ dB$ and $|A_{dp} - \hat{A}_{dp}| < 0.2\ dB$ under the conditions that $A_h > 10\ dB$ and $A_{dp} > 2\ dB$ are listed in Table 4.2. From the results of Table 4.2, we can see that both SC-RPA and SC-DRPA work better than RPA and DRPA for Cases I and II. This means that a self-consistent method can be used to obtain the best estimates of parameters κ and γ in situations of temperature or drop axis ratio variations. SC-DRPA provides the best performance and is significantly better than all other algorithms considered here.

4.5.3 Impact of bias in Z_h and Z_{dr} on algorithm performance

Just as with RPA, DRPA is not affected by a reflectivity bias or a differential reflectivity bias. If a reflectivity bias of δZ_h and a differential reflectivity bias of δZ_{dr} are imposed in (4.13), a solution for specific attenuation at horizontal polarization

Table 4.2: Comparison of performance between RPA, DRPA, SC-RPA and SC-DRPA: Case I - with radar observations without measurement error, Case II - with the signal fluctuations, and Case III - with the impact of δ and signal fluctuations. The percentages for which $|A_h - \hat{A}_h| < 1\ dB$ and $|A_{dp} - \hat{A}_{dp}| < 0.2\ dB$ under the conditions that $A_h > 10\ dB$ and $A_{dp} > 2\ dB$. Fixed values of γ and κ obtained from the Beard and Chuang model are used.

Case	RPA		DRPA		SC-RPA		SC-DRPA	
	$f(\varepsilon_A)$	$f(\varepsilon_{DA})$	$f(\varepsilon_A)$	$f(\varepsilon_{DA})$	$f(\varepsilon_A)$	$f(\varepsilon_{DA})$	$f(\varepsilon_A)$	$f(\varepsilon_{DA})$
Case I	14.2	44.3	20.5	52.3	44.3	65.7	96.4	80.1
Case II	22.8	48.3	26.4	48.3	33.1	58.0	87.2	64.4
Case III	22.6	48.2	26.4	46.4	23.9	47.1	75.2	61.5

can be expressed as

$$\hat{\alpha}_h(r) = \frac{[Z'_h(r)\delta Z_h(r)]^{b_1}[Z'_{dr}(r)\delta Z_{dr}(r)]^{c_1}(10^{0.1\gamma(b_1+\kappa c_1)\Delta\phi_{dp}(r_0;r_m)} - 1)}{I_h(r_0;r_m) + (10^{0.1\gamma(b_1+\kappa c_1)\Delta\phi_{dp}(r_0;r_m)} - 1)I_h(r;r_m)};$$
$$I_h(r_0;r_m) = 0.46(b_1+\kappa c_1)\int_{r_0}^{r_m}[Z'_h(r)\delta Z_h(r)]^{b_1}[Z'_{dr}(r)\delta Z_{dr}(r)]^{c_1}dr. \tag{4.23}$$

δZ_h and δZ_{dr} are constant according to range. Therefore (4.23) can be rewritten as

$$\hat{\alpha}_h(r) = \frac{[Z'_h(r)]^{b_1}[Z'_{dr}(r)]^{c_1}(\delta Z_h(r)^{b_1}\delta Z_{dr}(r)^{c_1})(10^{0.1\gamma(b_1+\kappa c_1)\Delta\phi_{dp}(r_0;r_m)} - 1)}{I_h(r_0;r_m) + (10^{0.1\gamma(b_1+\kappa c_1)\Delta\phi_{dp}(r_0;r_m)} - 1)I_h(r;r_m)};$$
$$I_h(r_0;r_m) = 0.46(b_1+\kappa c_1)(\delta Z_h(r)^{b_1}\delta Z_{dr}(r)^{c_1})\int_{r_0}^{r_m}[Z'_h(r)]^{b_1}[Z'_{dr}(r)]^{c_1}dr. \tag{4.24}$$

δZ_h and δZ_{dr} are canceled out between the numerator and denominator of the above equation. Finally, a solution of $\hat{\alpha_h}$ is the same as (4.13). We can see clearly that the impact of Z_h and Z_{dr} bias is canceled out between the numerator and denominator of (4.13) and (4.14).

SC-RPA is not affected by reflectivity bias for $A_h(r)$ retrieval, whereas SC-RPA is affected by reflectivity and differential reflectivity bias for $A_{dp}(r)$ retrieval. However, SC-DRPA can be affected by Z_h and Z_{dr} bias for both $A_h(r)$ and $A_{dp}(r)$ because SC-DRPA uses the Z_h - Z_{dr} relationship to obtain optimal values of γ and κ. SC-DRPA is evaluated for system biases. The percentages for which $|A_h - \hat{A}_h| < 1\ dB$ and $|A_{dp} - \hat{A}_{dp}| < 0.2\ dB$ under the conditions that $A_h > 10\ dB$ and $A_{dp} > 2\ dB$ are shown in Fig. 4.19. The results from Fig. 4.19 show that SC-DRPA is not much

affected by Z_h bias. However, SC-DRPA is sensitive to Z_{dr} bias because SC-DRPA uses the $Z_h - Z_{dr}$ relationship to find the optimal values of γ and κ. SC-DRPA performs well within $\pm 0.3\ dB$ of Z_{dr} bias. If Z_{dr} bias is greater than $0.3\ dB$, it will be better to use DRPA instead of the self-consistency algorithm.

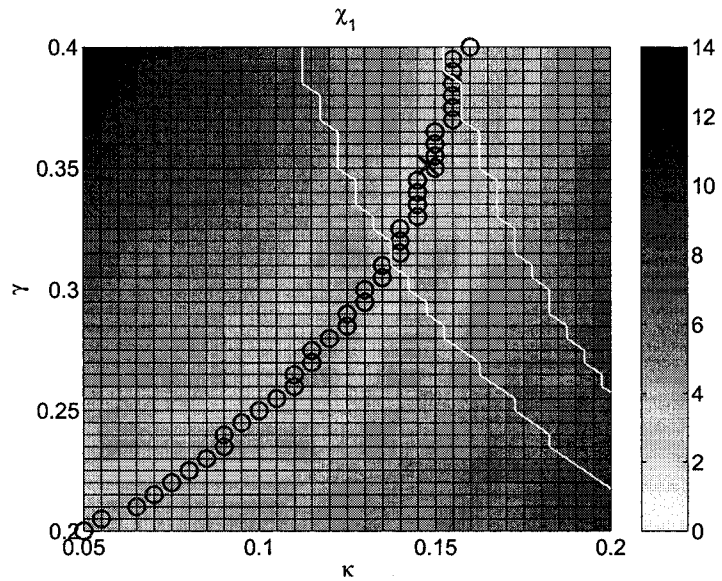

(a)

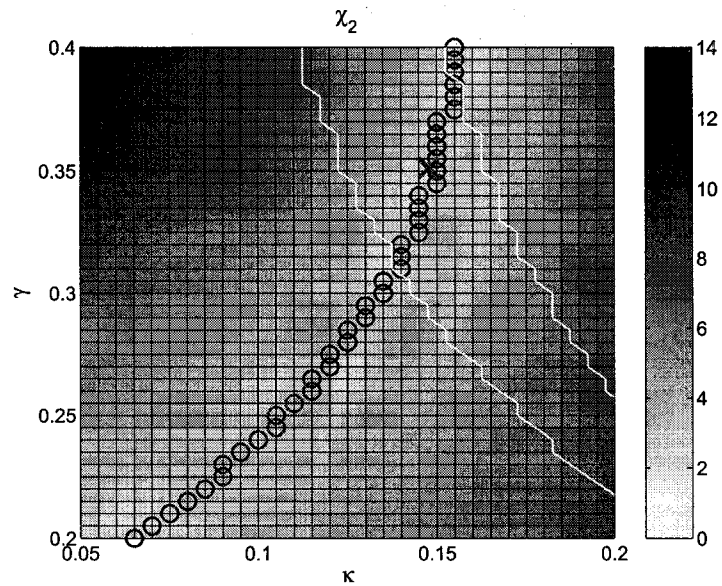

(b)

Figure 4.12: An example of (a) χ_1 and (b) χ_2 obtained by (4.19). "o"s indicate the optimal values of κ according to γ. The white lines indicate the boundary condition. "x"s indicate the optimal value of γ and κ in terms of χ_1 and χ_2.

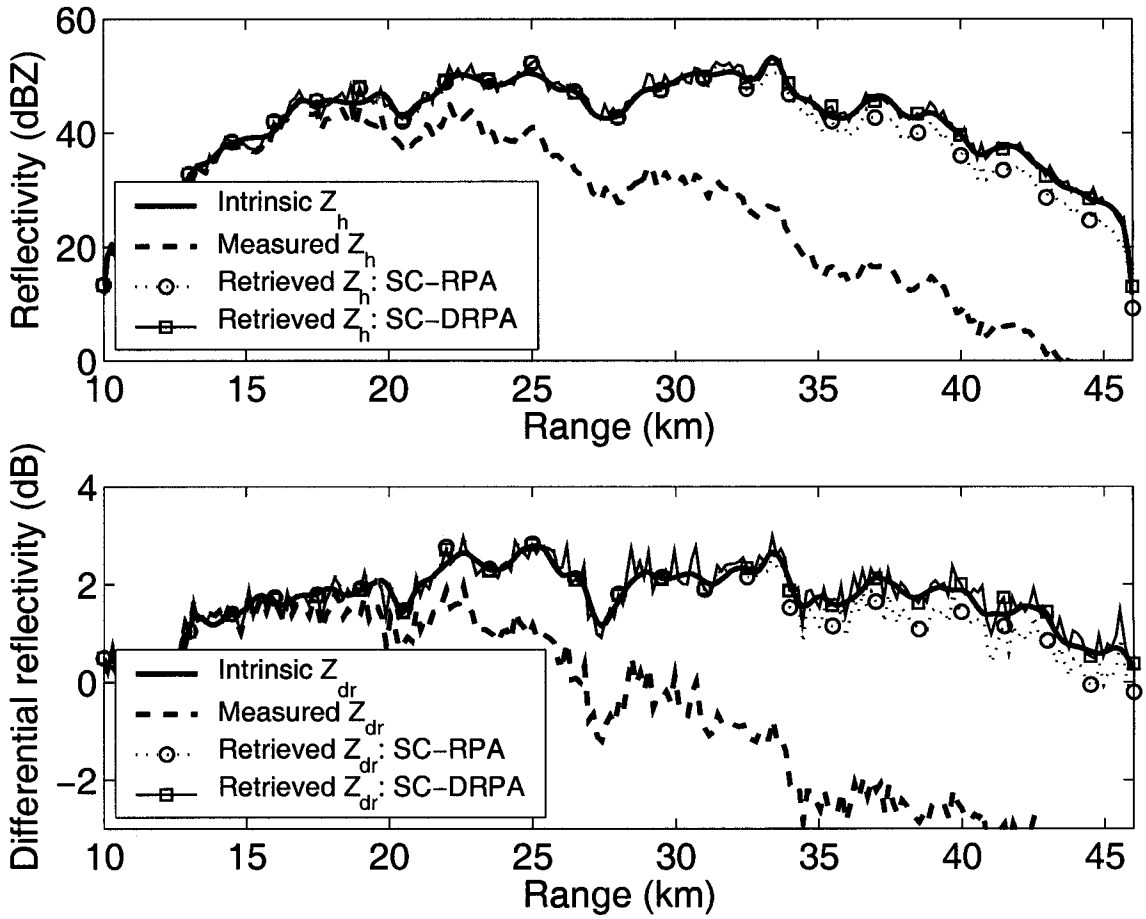

Figure 4.13: An example of retrieved observations by the SC-DRPA with the optimal values of γ_{opt} and κ_{opt}.

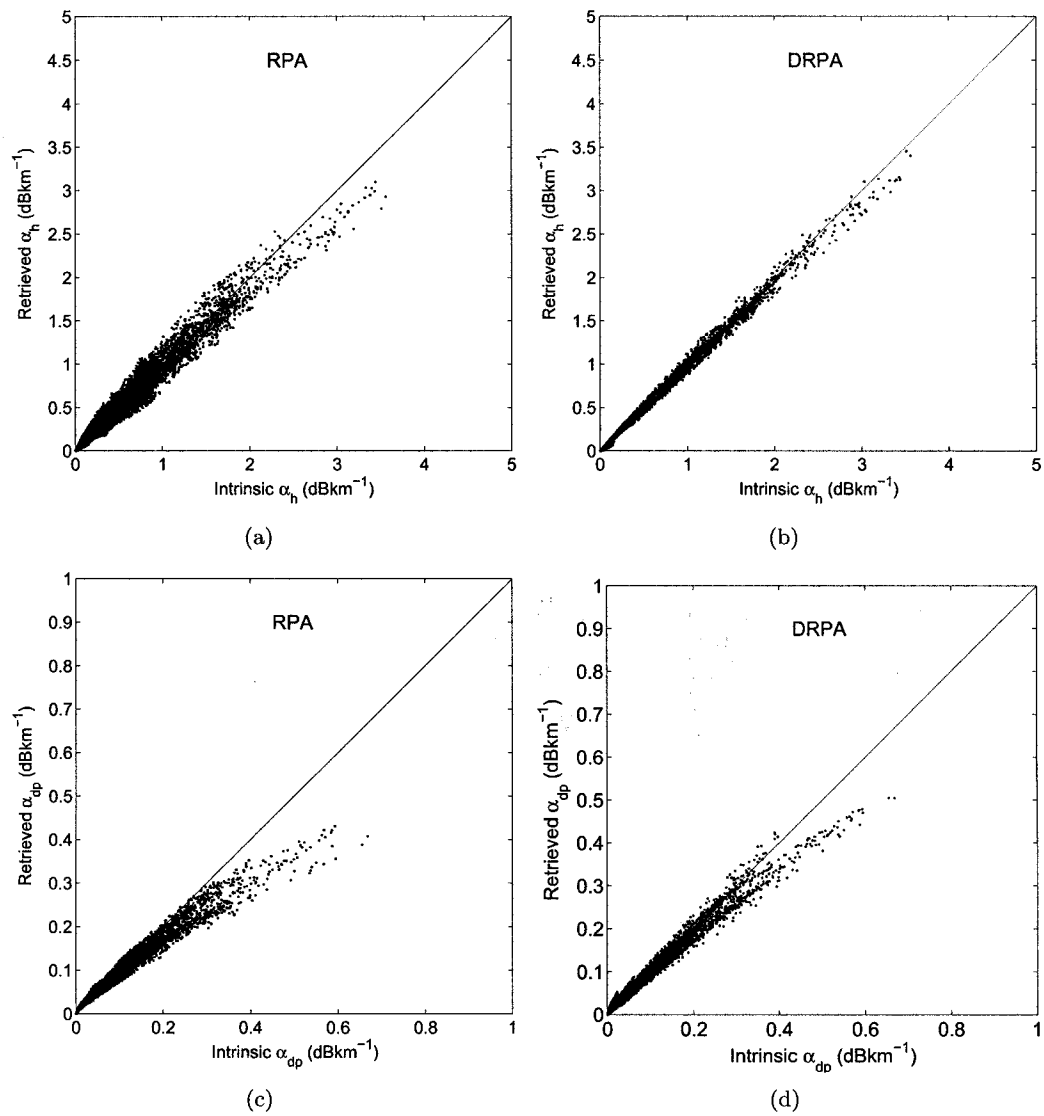

Figure 4.14: Scatter plot of (a) intrinsic specific attenuation vs. retrieved specific attenuation at horizontal polarization using RPA with the fixed value of γ, (b) intrinsic specific attenuation vs. retrieved specific attenuation at horizontal polarization using DRPA with the fixed values of γ and κ, (c) intrinsic differential attenuation vs. retrieved differential attenuation using RPA with the fixed value of κ, and (d) intrinsic differential attenuation vs. retrieved differential attenuation using DRPA with the fixed values of γ and κ obtained from the ABC model.

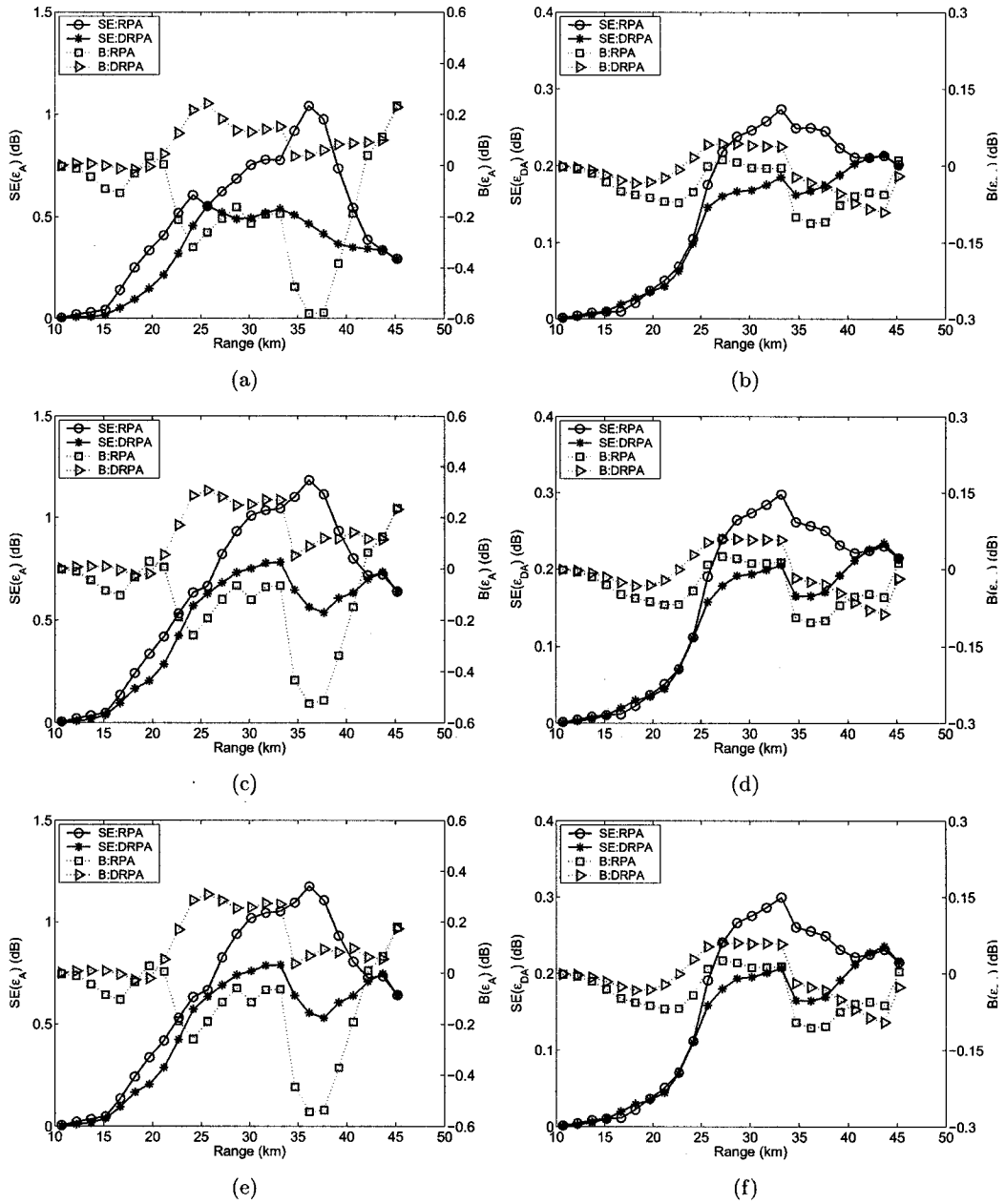

Figure 4.15: (a) Standard error (left axis) and bias (right axis) of difference between intrinsic A_h and retrieved $\hat{A}_h$ as a function of range, (b) standard error and bias of difference between intrinsic A_{dp} and retrieved $\hat{A}_{dp}$ as a function of range for Case I, (c) and (d) same as for Case II, (e) and (f) same as for Case III. The estimated observations are obtained by using RPA and DRPA with the fixed values of γ and κ obtained from the ABC model.

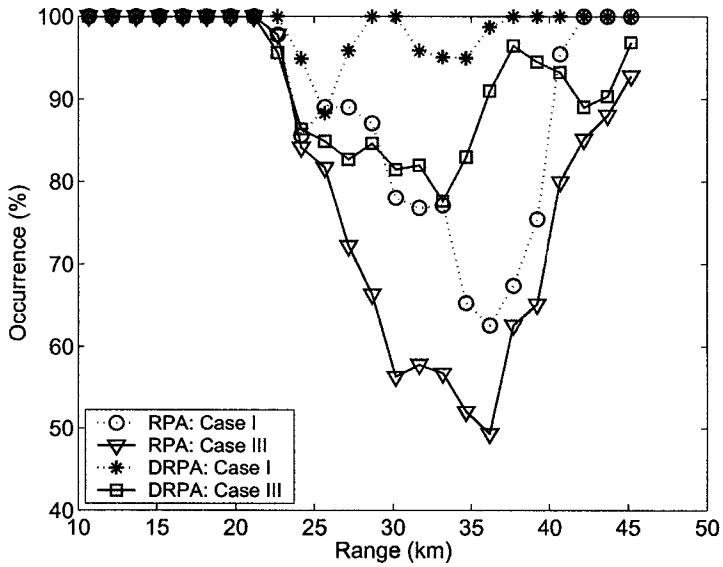

(a)

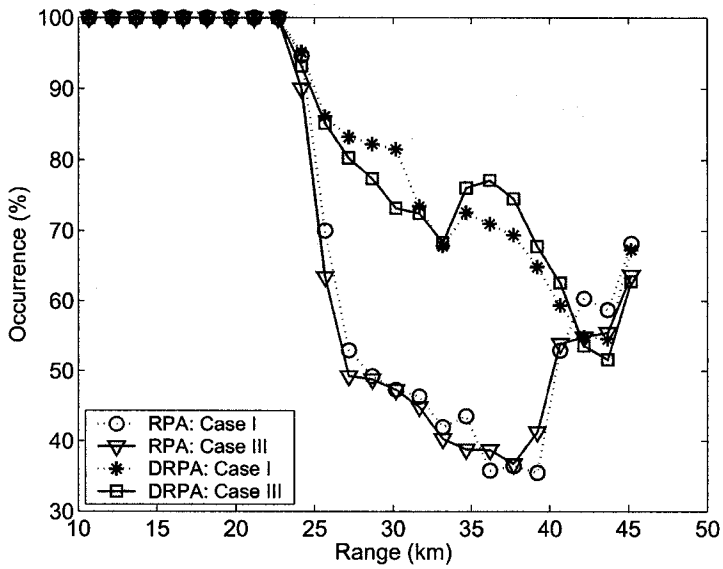

(b)

Figure 4.16: (a) Percentages for which $|A_h - \hat{A}_h| < 1\ dB$, (b) percentages for which $|A_{dp} - \hat{A}_{dp}| < 0.2\ dB$ as a function of range for Cases I and III. The estimated observations are retrieved by RPA and DRPA with the fixed values of γ and κ obtained from the ABC model.

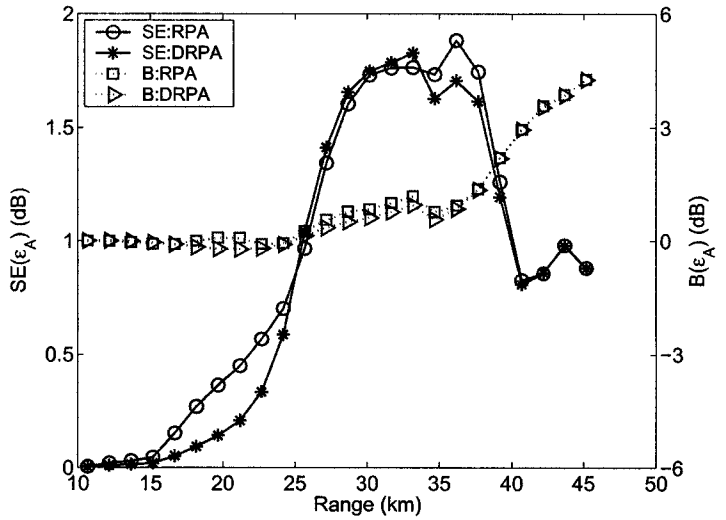

(a)

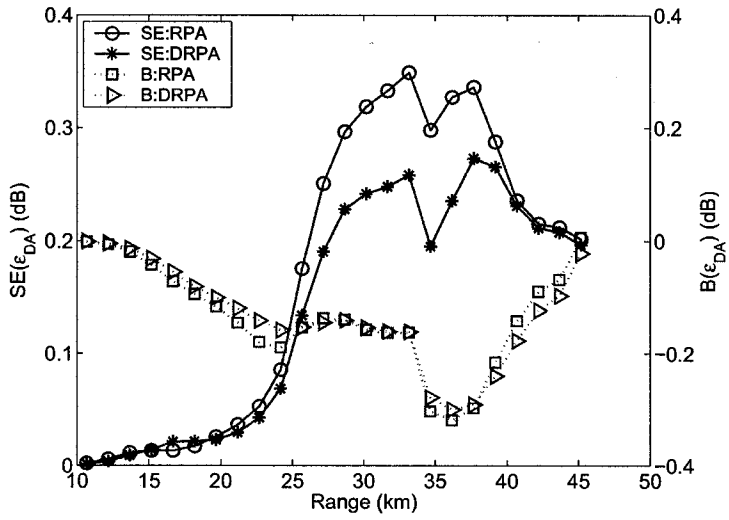

(b)

Figure 4.17: (a) Standard error (left axis) and bias (right axis) of difference between intrinsic A_h and retrieved $\hat{A}_h$ as a function of range, (b) standard error and bias of difference between intrinsic A_{dp} and retrieved $\hat{A}_{dp}$ as a function of range for Case I. The estimated observations are retrieved by using RPA and DRPA with the fixed values of γ and κ obtained from the Beard and Chuang model.

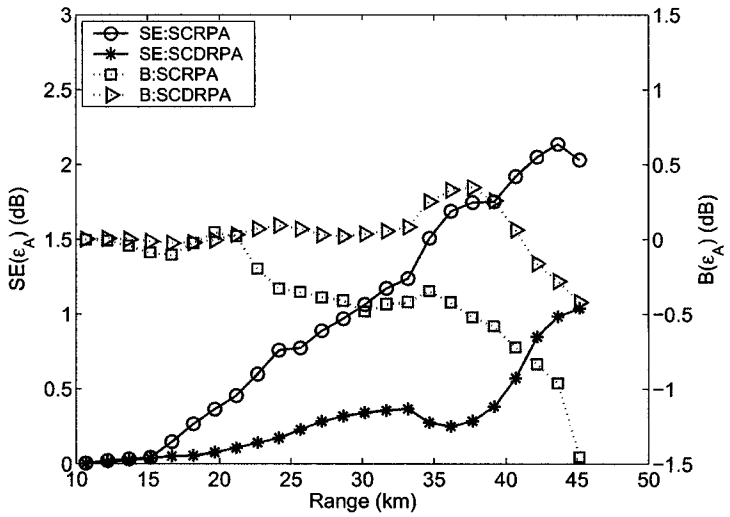

(a)

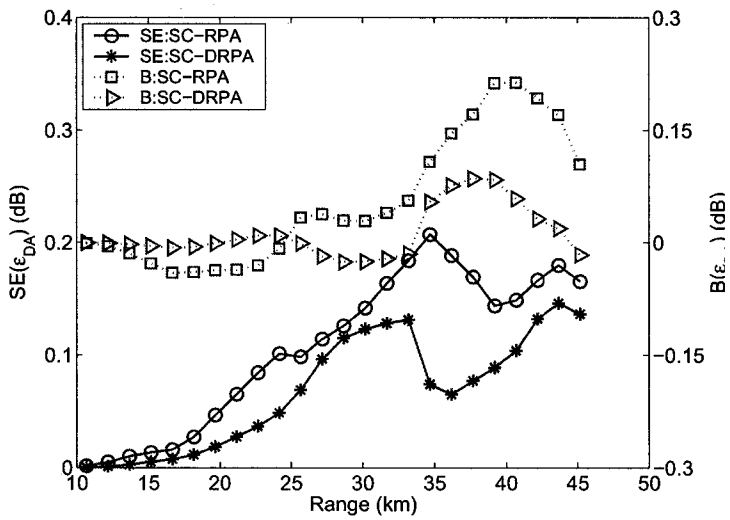

(b)

Figure 4.18: (a) Standard error (left axis) and bias (right axis) of difference between intrinsic A_h and retrieved $\hat{A}_h$ as a function of range, (b) standard error and bias of difference between intrinsic A_{dp} and retrieved $\hat{A}_{dp}$ as a function of range for Case I. The estimated observations are retrieved by using SC-RPA and SC-DRPA.

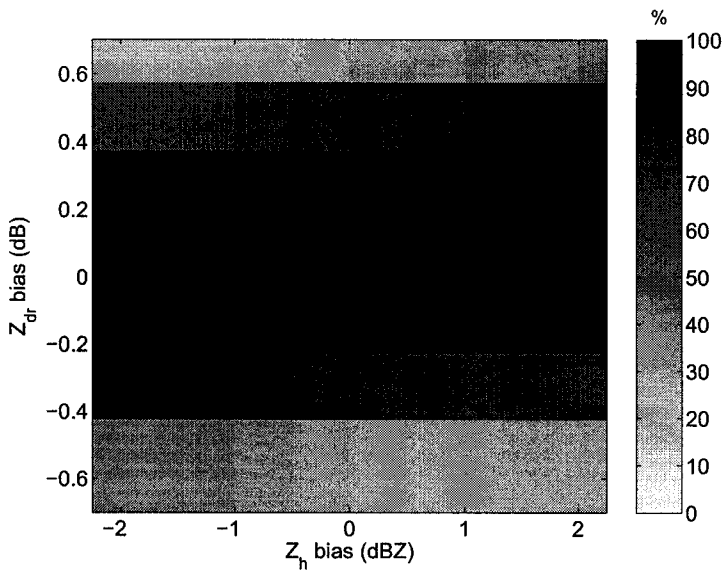

(a)

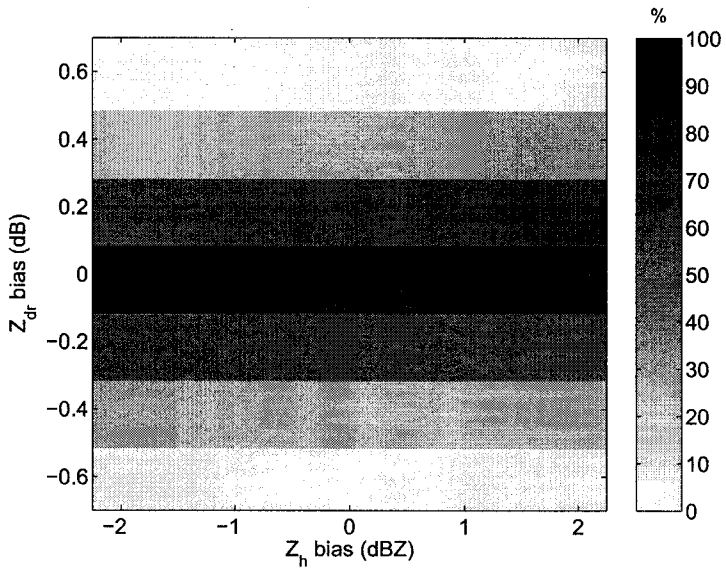

(b)

Figure 4.19: (a) Percentages for which $|A_h - \hat{A}_h| < 1\ dB$ given that $A_h > 10\ dB$, (b) percentages for which $|A_{dp} - \hat{A}_{dp}| < 0.2\ dB$ under the condition that $A_{dp} > 2\ dB$ for Case III according to Z_h and Z_{dr} biases. The estimated observations are retrieved by SC-DRPA.

4.6 Summary and Discussion

Attenuation correction is an important step for radar observations to be used for quantitative applications at higher frequencies such as X-band. Differential propagation phase ϕ_{dp} is unaffected by attenuation due to precipitation. The introduction of ϕ_{dp} (Testud et al. 2000) and Z_{dr} constraint (Smyth and Illingworth 1998; Bringi et al. 2001) for attenuation correction stabilized the process, whereas the self-consistency method brought in a new level of accuracy. This section introduced a dual-polarization rain profiling algorithm further improving the attenuation correction process, relating Z_h and Z_{dr} with attenuation and cumulative attenuation along the path. The introduction of Z_{dr} in the retrieval procedure removes the assumptions such as constant N_w along a path in the algorithm formulation. Subsequently, it can retrieve attenuation better. A new self-consistent method corresponding to the proposed attenuation correction algorithm has also been presented. This method can derive the optimal value of the coefficients to convert ϕ_{dp} to specific attenuation and differential attenuation simultaneously. The algorithms proposed were evaluated using radar observations simulated from data observed by the CSU-CHILL radar. The evaluation results show that the proposed dual-polarization attenuation correction algorithm and self-consistent method work better than previous techniques available in the literature, significantly increasing the percentage of attenuation corrected data to satisfy measurement requirements.

CHAPTER 5

RETRIEVAL OF REFLECTIVITY IN A NETWORKED RADAR ENVIRONMENT

5.1 Introduction

Conventional meteorological radars provide coverage over long ranges (often hundreds of kilometers) and support weather surveillance and hydrological monitoring applications by using high-power transmitters and mechanically scanned antennas. These systems operate at wavelengths in the 5-10 centimeter range in order to penetrate precipitation, and necessitate the use of physically large antennas to achieve high resolution at the distant ranges. As an alternate solution, a networked radar system concept has been recently proposed (Chandrasekar and Jayasumana 2001; McLaughlin 2001). The basic principle of the networked radar environment is to be able to provide good coverage, in terms of accuracy and resolution, to a focused area through a network of radars. In order to be able to provide economically viable solutions to this approach, meteorological radar operation must change from the "preferred" S-band operation to higher frequencies (just as spaceborne weather radar systems) so that physically smaller antennas can be deployed. However, at higher frequencies, the impact of attenuation due to precipitation needs to be resolved for successful implementation.

In order to investigate the attenuation impact as well as evaluate the algorithm development, it is useful to have simultaneous X-band observations with and without the impact of path attenuation. The X-band observations with realistic range profiles can be generated from high-resolution observations of S-band dual-polarization radar. From the S-band data, the X-band data can be synthesized based on fundamental

microphysical properties of precipitation such as drop size and shape distribution (Chandrasekar et al. 2004a). In this chapter, to investigate the impact of attenuation at X-band as well as evaluate the retrieval algorithm for a networked radar system, X-band observations are simulated by the empirical conversion method as described in Chapter 3.

The concept of a dual-radar method for reflectivity and specific attenuation retrieval was studied by Srivastava and Tian (1996) and Tian and Srivastava (1997). They used an analytical method to retrieve specific attenuation and reflectivity. In this chapter, a new reflectivity and specific attenuation retrieval method in a networked radar environment is presented. The specific attenuation distribution can be solved by the integral equation for reflectivity, in a manner similar to that used with a differential phase constraint (Testud et al. 2000; Bringi and Chandrasekar 2001). Reflectivity and specific attenuation along each beam are obtained by the combined back scatter and forward scatter equations of the precipitation medium with total path attenuation constraints. The proposed retrieval method is described in Section 5.2. The implementation and evaluation of the method is presented in Section 5.3 and important results are discussed in Section 5.4.

5.2 Retrieval Method of Reflectivity and Specific Attenuation in the Networked Radar Environment

The basis of a networked radar system is simultaneous observations of the same event by multiple radars in different locations. A three-radar network system is used for illustration as shown in Fig. 5.1. Three radars are located at A, B and C, operating at the same attenuating frequency and scanning in a low elevation plane. In the absence of attenuation, the reflectivity in a common volume for each radar should be the same. However, the measured reflectivity in a common volume is different because of the difference of the integrated attenuation along the paths from each radar.

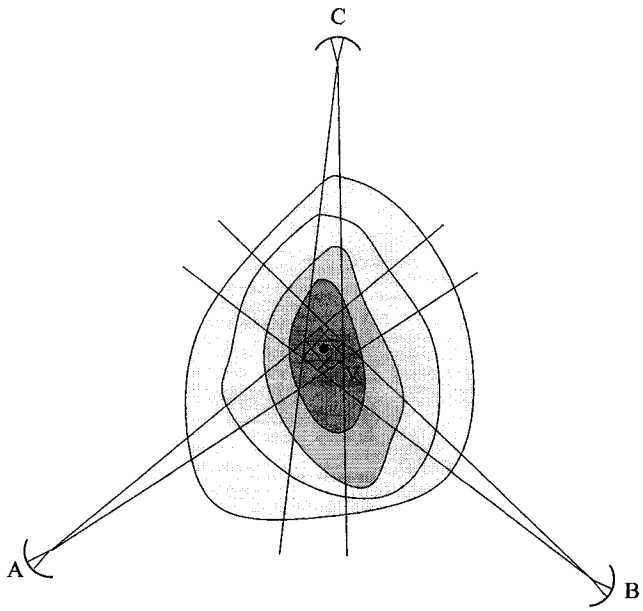

Figure 5.1: Schematic of the conceptual arrangement for reflectivity and specific attenuation retrieval with networked radars.

5.2.1 A solution of specific attenuation retrieval

The specific attenuation (α_h;dB/km) can be approximately parameterized with respect to reflectivity (Z_h;mm^6m^{-3}) by means of a power law as

$$\alpha_h(r) = a[Z_h(r)]^b. \tag{5.1}$$

Measured reflectivity ($Z'_h(r)$) at range r can be defined in terms of intrinsic reflectivity (unattenuated) and specific attenuation as

$$Z'_h(r) = Z_h(r)e^{-0.46\int_0^r \alpha_h(s)ds}. \tag{5.2}$$

The concept of normalized drop size distribution can be used to provide interpretation of a, b (Testud et al. 2000; Bringi and Chandrasekar 2001). The integrated path attenuation can be expressed in terms of intrinsic reflectivity Z_h and attenuated reflectivity Z'_h as

$$2\int_{r_0}^{r} \alpha_h(s)ds = 10log_{10}(Z_h(r)) - 10log_{10}(Z'_h(r)) \tag{5.3}$$

where r_0 is the range corresponding to the first resolution volume with precipitation. After modest algebraic manipulation using (5.1) - (5.3), the specific attenuation along the path can be retrieved as (for detailed derivation, refer Appendix B)

$$\begin{aligned} \Delta Z(r_m) &= 10log_{10}(Z_h(r_m)) - 10log_{10}(Z'_h(r_m)) = 2\int_{r_0}^{r} \alpha_h(s)ds; \\ \hat{\alpha}_h(r) &= \frac{[Z'_h(r)]^b(10^{0.1b\Delta Z(r_m)} - 1)}{I(r_0; r_m) + (10^{0.1b\Delta Z(r_m)} - 1)I(r; r_m)}; \\ I(r_0; r_m) &= 0.46b\int_{r_0}^{r_m} [Z'_h(s)]^b ds \end{aligned} \tag{5.4}$$

where $\Delta Z(r_m)$ is the difference between intrinsic reflectivity and attenuated reflectivity, namely two-way cumulative attenuation, and parameter b corresponds to the $\alpha - Z$ relation. The retrieved reflectivity ($\hat{Z}_h(r)$) can be expressed with respect to attenuated reflectivity and retrieved specific attenuation ($\hat{\alpha}_h$) at range r as

$$10log_{10}(\hat{Z}_h(r)) = 10log_{10}(Z'_h(r)) + 2\int_{r_0}^{r} \hat{\alpha}_h(s)ds. \tag{5.5}$$

If the intrinsic reflectivity at range r_m is known, then we can obtain the specific attenuation distribution and reflectivity along a path r_0 to r_m using (5.4) and (5.5). The problem of how to find the intrinsic reflectivity at range r_m still remains unsolved. A networked radar approach is proposed to find the intrinsic reflectivity at range r_m.

5.2.2 Reflectivity retrieval in the networked radar environment

The intrinsic reflectivity at a common volume of the three radars can be obtained by a networked radar approach. Note that a hypothesis is made that the intrinsic reflectivities at common volumes observed by each of the radars are the same. This means that $Z_{h,AN} = Z_{h,BN} = Z_{h,CN} = Z_{hN}$, where $Z_{h,AN}$ indicates the intrinsic reflectivity at a common volume observed by radar A at range N. The optimal retrieved reflectivity at a common volume V_N can be obtained by making an initial seed value of reflectivity and iteratively solving for it.

An example of reflectivity retrieval result is shown in Fig. 5.2. In top panel, the dotted line indicates measured (attenuated) reflectivity that is observed by one

radar. The dotted-dashed line indicates the intrinsic reflectivity, while the solid line is the retrieved reflectivity by the networked radar technique. In bottom panel, The dotted-dashed line indicates the intrinsic specific attenuation, while the solid line is the retrieved specific attenuation.

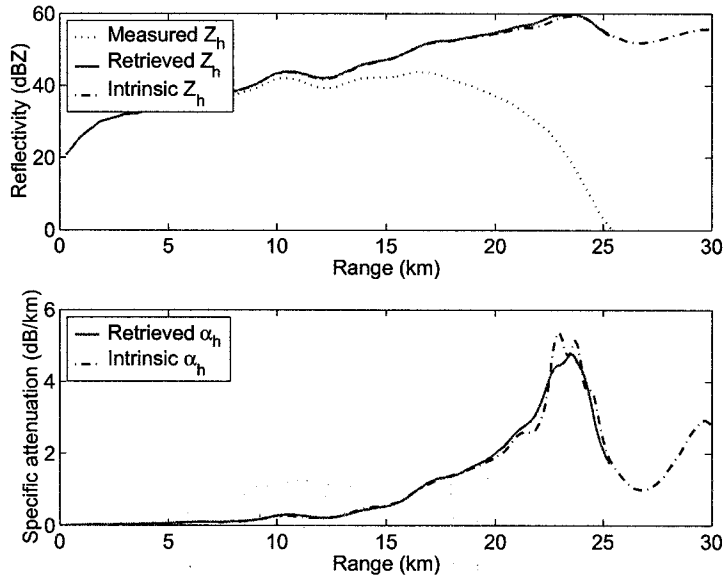

Figure 5.2: An example of reflectivity retrieval in a networked radar system.

5.2.3 Error factors of the reflectivity retrieval technique in networked radar system

For evaluation of the reflectivity retrieval technique in a networked radar system, the possible error factors need to be considered. The errors can be caused by range resolution volume, pointing mismatch for common volume, and system errors due to signal fluctuations and system bias.

5.2.3.1 Range resolution volume and pointing mismatch for common volume

As mentioned in the previous section, it is assumed that reflectivity of the common volume is the same for all the radars. If radars with very narrow beam widths are used, the hypothesis is true. However, typical radars use antennas with 1-2 degree beam width. Therefore, the reflectivity retrieval technique in networked radar systems

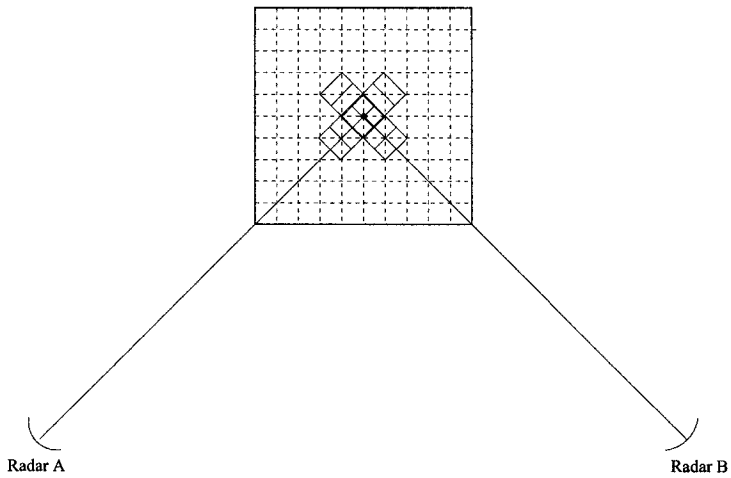

Figure 5.3: An illustration of the range resolution volume problem.

needs evaluation for differences of intrinsic reflectivity due to range resolution volume. The range resolution problem is shown in Fig. 5.3. The range resolution problem can be caused by nonuniform distribution of rainfall at common volumes. The error in reflectivity at common volume due to range resolution volume can be defined as

$$Z_{h,N} = Z_{h,AN} + \delta Z^V_{h,AN} = Z_{h,BN} + \delta Z^V_{h,BN} = Z_{h,CN} + \delta Z^V_{h,CN} \tag{5.6}$$

where $\delta Z^V_{h,AN}$ indicates a reflectivity error due to range resolution volume by radar A at common volume N.

Another error factor of reflectivity at common volume can be a pointing mismatch error. Fig. 5.4 shows how the pointing mismatch error can be generated. The error in reflectivity at common volume due to a pointing mismatch can be defined as

$$Z_{h,N} = Z_{h,AN} + \delta Z^P_{h,AN} = Z_{h,BN} + \delta Z^P_{h,BN} = Z_{h,CN} + \delta Z^P_{h,CN} \tag{5.7}$$

where $\delta Z^V_{h,AN}$ indicates reflectivity error due to a pointing mismatch by radar A at common volume N. Fig. 5.5 shows an example of error in reflectivity due to range resolution volume and a pointing mismatch. From the results of Fig. 5.5, we can see that reflectivity values at common volume are different.

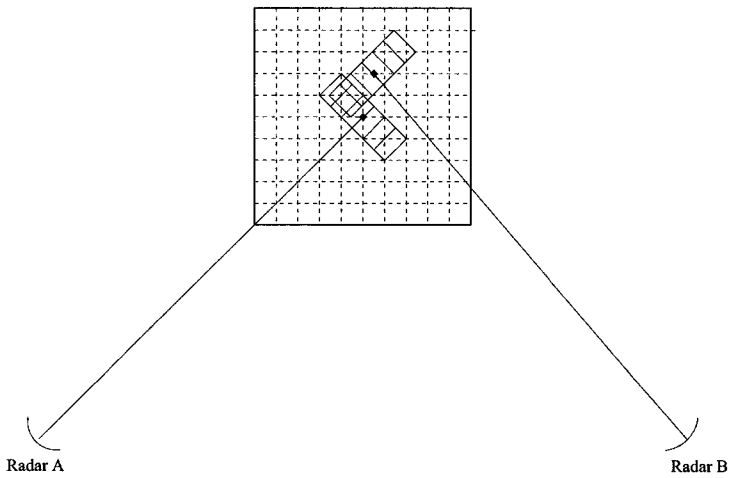

Figure 5.4: An illustration of pointing mismatch problem.

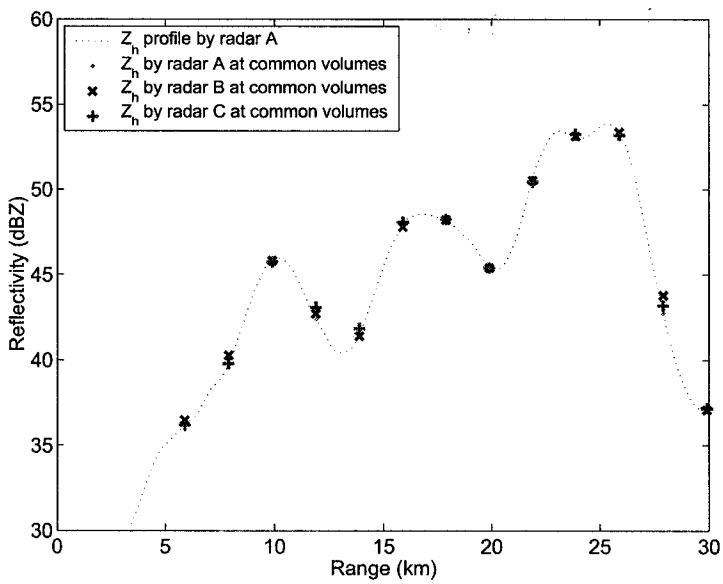

Figure 5.5: An example of error in reflectivity at common volumes due to range resolution volume and pointing mismatch.

5.2.3.2 System errors

The performance of the reflectivity retrieval technique in a networked radar system can be affected by signal fluctuations and system bias. The error factor in reflectivity at common volume due to system error can be defined as

$$\begin{aligned} Z_{h,N} &= Z_{h,AN} + \delta Z^F_{h,AN} + \delta Z^B_{h,AN} \\ &= Z_{h,BN} + \delta Z^F_{h,BN} + \delta Z^B_{h,BN} \\ &= Z_{h,CN} + \delta Z^F_{h,CN} + \delta Z^B_{h,CN} \end{aligned} \tag{5.8}$$

where $\delta Z^F_{h,AN}$ indicates a reflectivity error due to signal fluctuation and $\delta Z^B_{h,AN}$ indicates a reflectivity error due to system bias by radar A at common volume N.

5.3 Evaluation

The reflectivity and specific attenuation retrieval method is evaluated using X-band data simulated by the empirical conversion method. For evaluation, a network of three radar systems scanning at a low elevation plane is considered here. The attenuated reflectivity is generated for each radar location with respect to intrinsic reflectivity and specific attenuation. Three cases are studied here; 000204-000607 UTC; 013006-013707 UTC on July 19, 2000; and 201245-201348 UTC on July 23, 2004. These cases are convective events with heavy rain.

5.3.1 Evaluation for range resolution volume and pointing mismatch

For evaluation of range resolution volume and pointing mismatch, a network of three radar systems operating at X-band with antenna beam width of 2 degree is considered here. Note that CASA radar operates at X-band with antenna beam width of 1.8 degree.

5.3.1.1 Case I: July 19, 2000, 000204-000607 UTC

Fig. 5.6 shows intrinsic reflectivity and intrinsic specific attenuation. Fig. 5.7 shows attenuated reflectivity for radars A, B, and C at X-band. Fig. 5.7 clearly

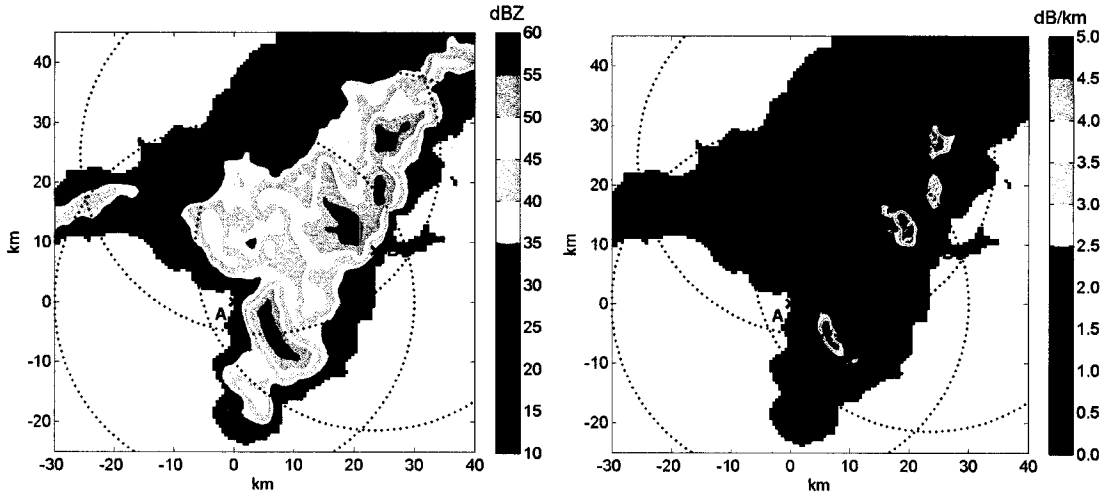

Figure 5.6: Case I: (a) intrinsic reflectivity and (b) intrinsic specific attenuation at X-band; "x"s indicate the location of radars A, B, and C. The dotted rings are maximum unambiguous range.

shows the impact of attenuation according to radar location and beam path. Using attenuated reflectivity from each radar and (5.4)−(5.5), reflectivity for each radar is retrieved as shown in Fig. 5.8. For comparison of reflectivity retrieval for each radar, intrinsic cumulative attenuation and retrieved cumulative attenuation are shown in Fig. 5.9. The retrieved reflectivity and specific attenuation are shown in Figs. 5.10 and 5.11. For comparison, the distribution of the difference between intrinsic reflectivity and retrieved reflectivity and between intrinsic specific attenuation and retrieved specific attenuation are shown in Fig. 5.12. The standard deviation of the difference between intrinsic reflectivity and retrieved reflectivity is 0.74 dBZ with negligible bias, whereas the standard deviation of the difference between intrinsic specific attenuation and retrieved specific attenuation is 0.18 dB/km. The results show that the retrieval algorithm works reasonably well.

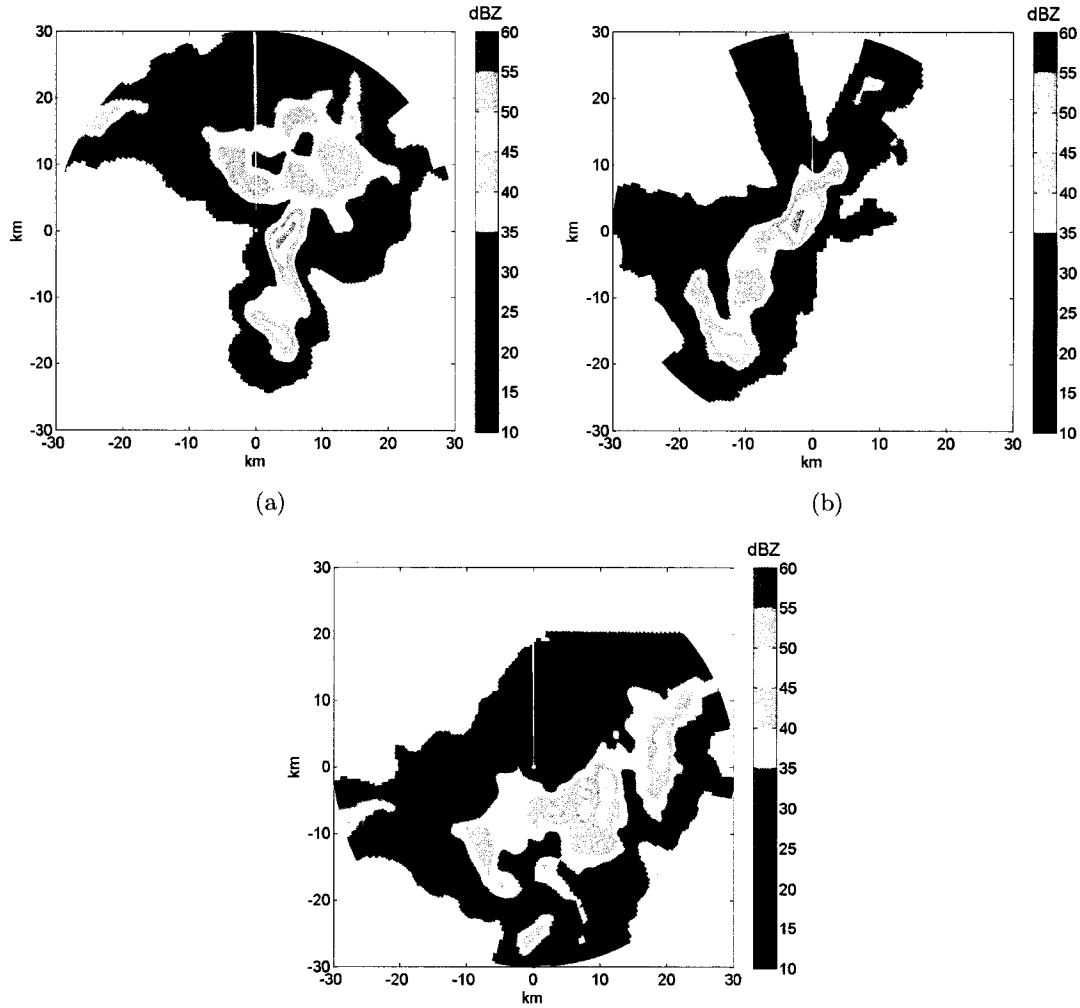

Figure 5.7: Case I: Attenuated reflectivity for radar (a) A, (b) B, and (c) C at X-band.

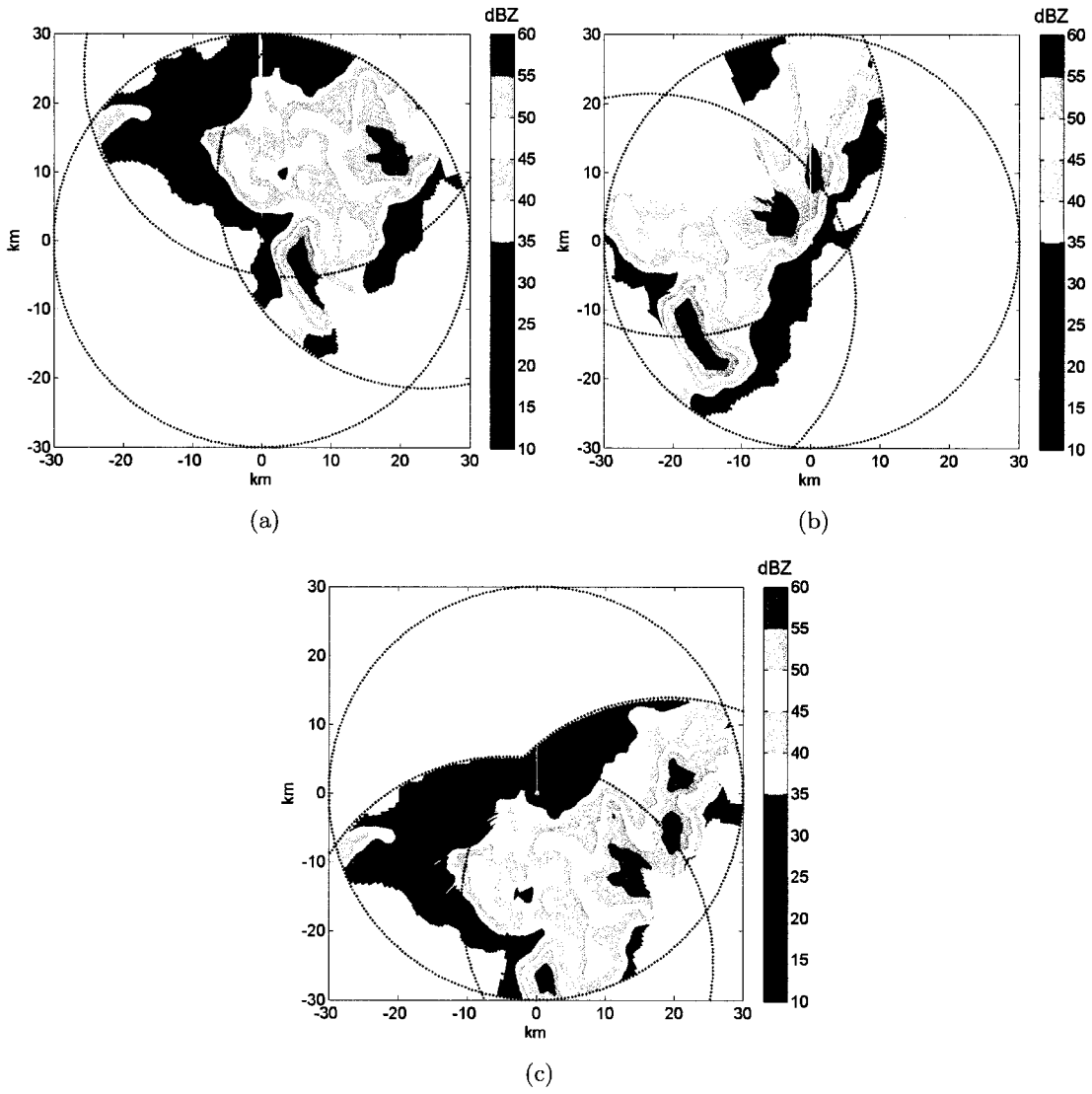

Figure 5.8: Case I: Retrieved reflectivity for radar (a) A, (b) B, and (c) C.

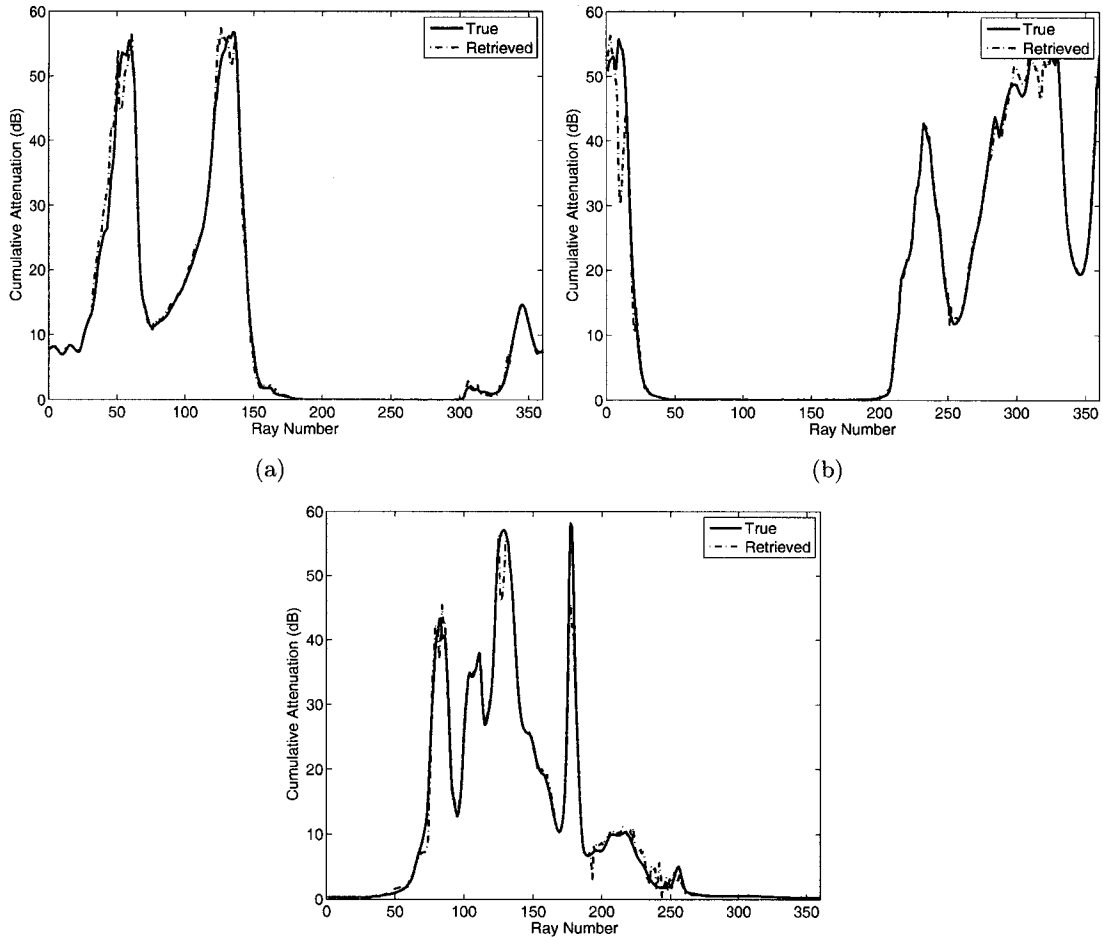

Figure 5.9: Case I: Comparison between intrinsic cumulative attenuation and retrieved cumulative attenuation for radar (a) A, (b) B, and (c) C.

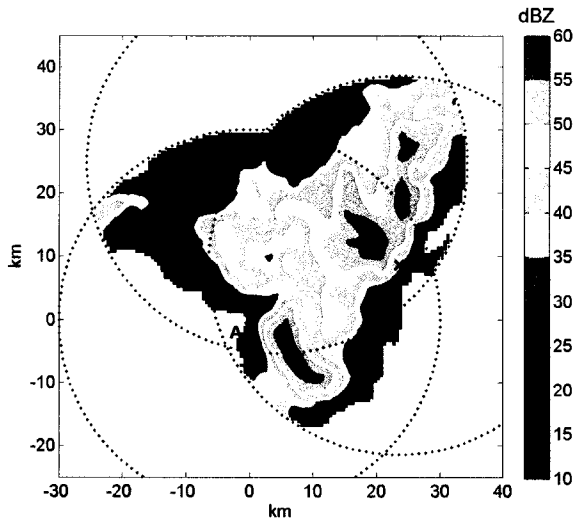

Figure 5.10: Case I: Retrieved reflectivity.

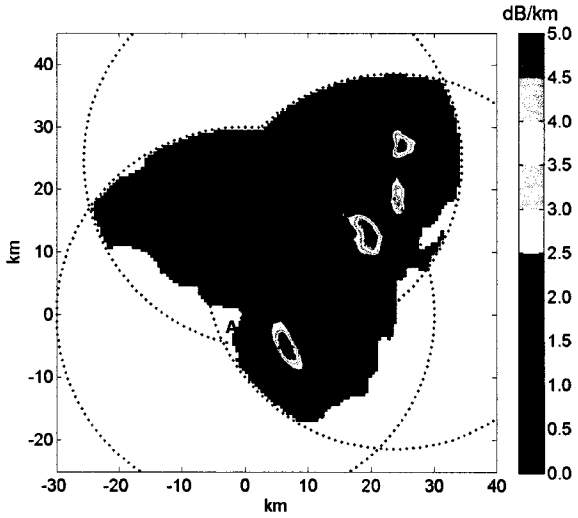

Figure 5.11: Case I: Retrieved specific attenuation.

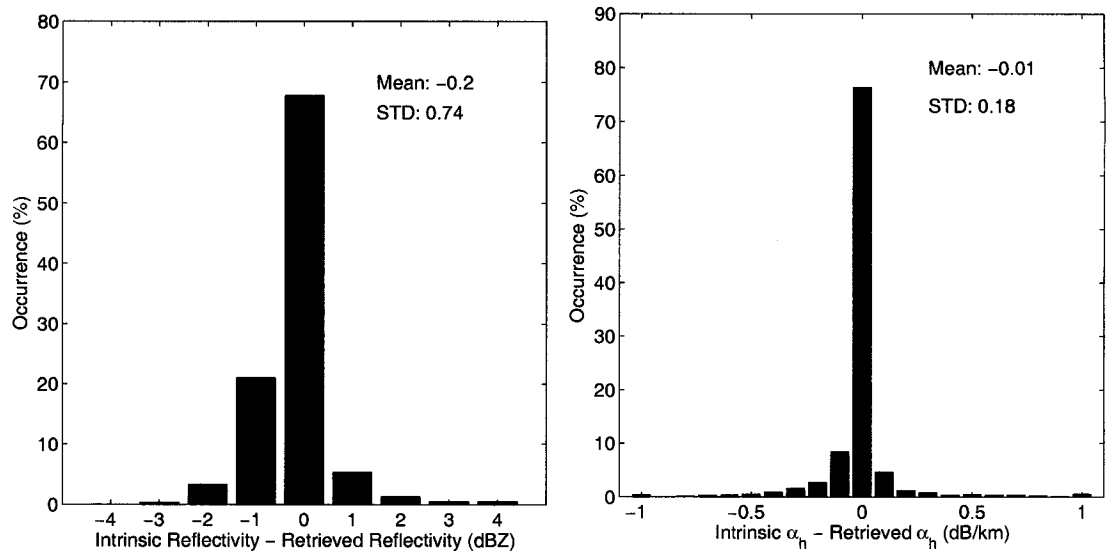

(a) (b)

Figure 5.12: Case I: Distribution of (a) the difference between intrinsic reflectivity and retrieved reflectivity, (b) the difference between intrinsic specific attenuation and retrieved specific attenuation.

5.3.1.2 *Case II: July 19, 2000, 013006-013707 UTC*

Fig. 5.13 shows the intrinsic reflectivity and specific attenuation, while attenuated reflectivities for radars A, B, and C are shown in Fig. 5.14. For comparison of reflectivity retrieval for each radar, intrinsic cumulative attenuation and retrieved cumulative attenuation are shown in Fig. 5.15. Retrieved reflectivity and specific attenuation are shown in Figs. 5.16 and 5.17. For comparison, the distribution of the difference between intrinsic reflectivity and retrieved reflectivity and between intrinsic specific attenuation and retrieved specific attenuation are shown in Fig. 5.18. The standard deviation of the difference between intrinsic reflectivity and retrieved reflectivity is 0.78 dBZ, while the standard deviation of the difference between intrinsic specific attenuation and retrieved specific attenuation is 0.07 dB/km.

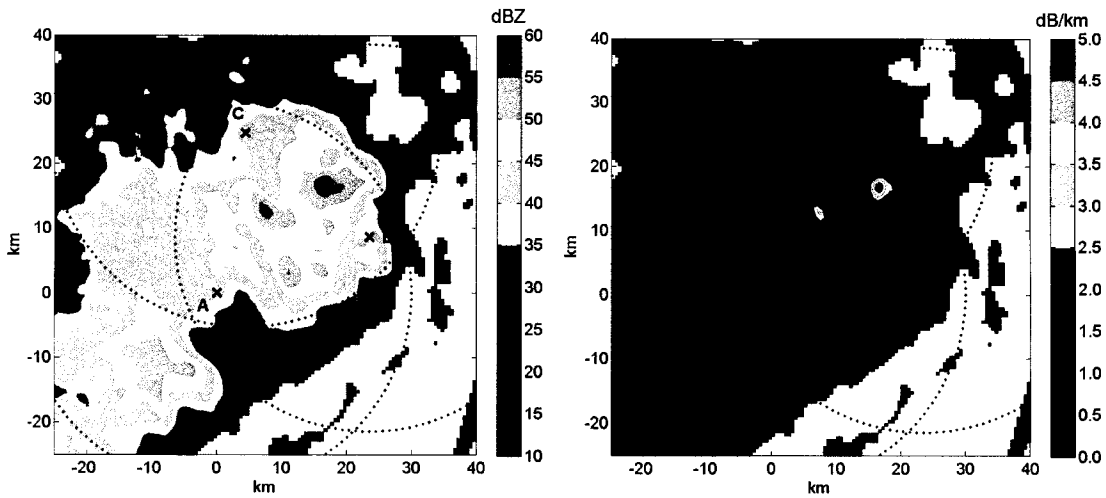

Figure 5.13: Case II: (a) intrinsic reflectivity and (b) intrinsic specific attenuation at X-band; "x"s indicate the location of radars A, B, and C. The dotted rings are maximum unambiguous range.

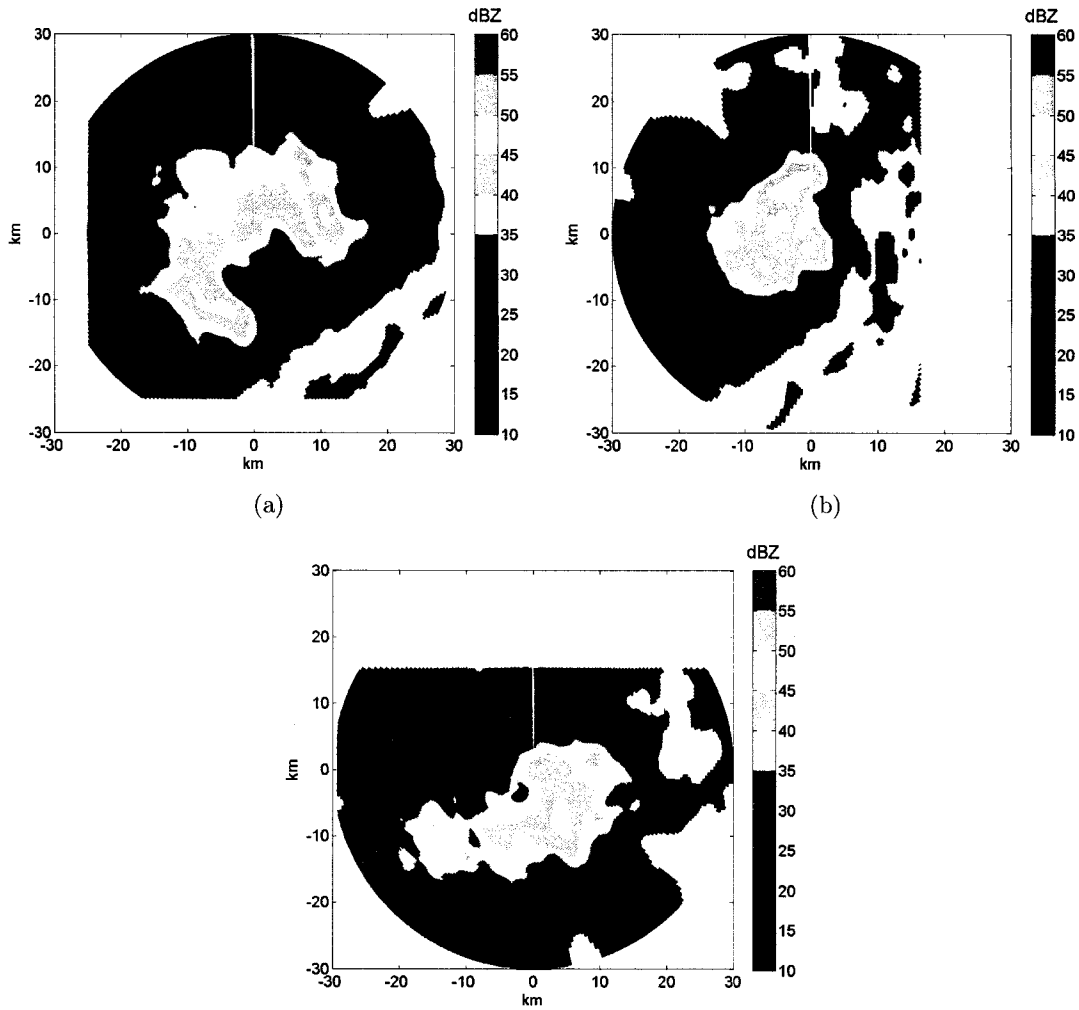

Figure 5.14: Case II: Attenuated reflectivity for radar (a) A, (b) B, and (c) C at X-band.

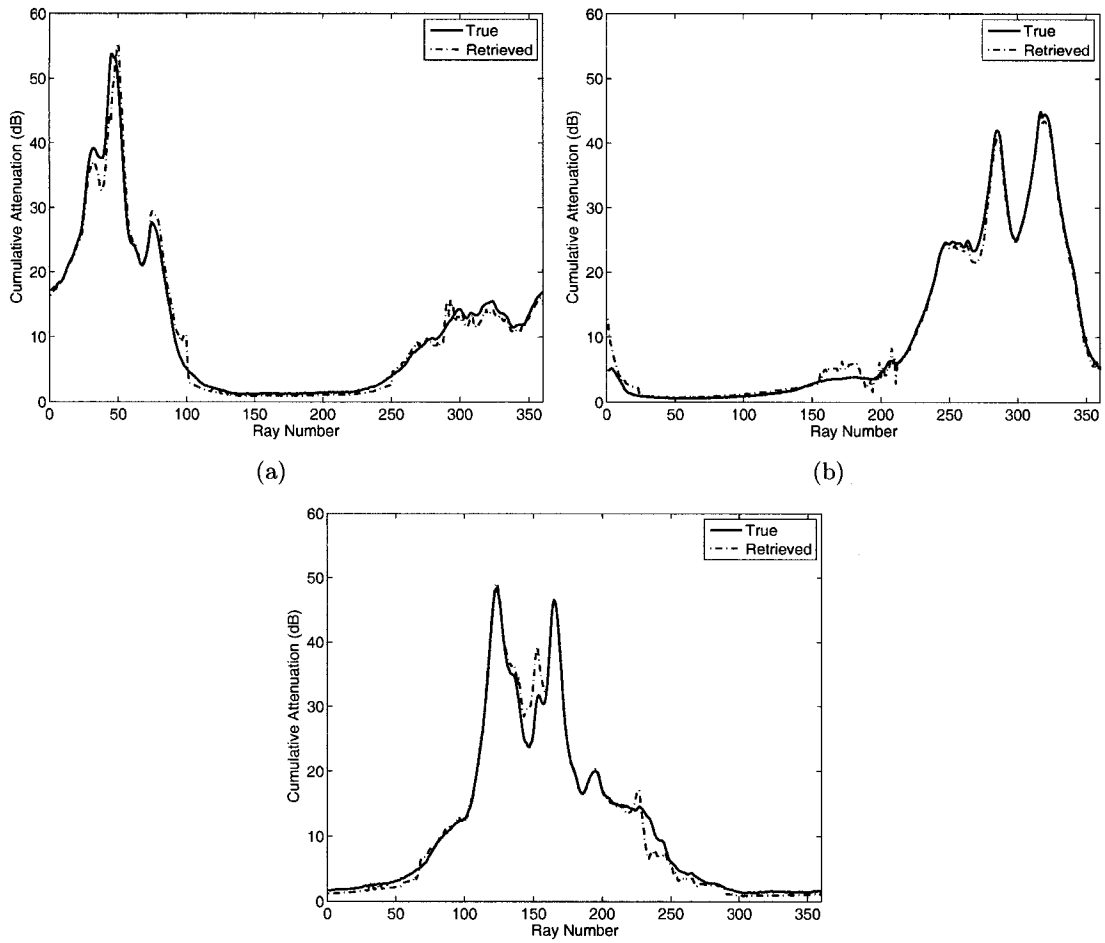

Figure 5.15: Case II: Comparison between intrinsic cumulative attenuation and retrieved cumulative attenuation for radar (a) A, (b) B, and (c) C.

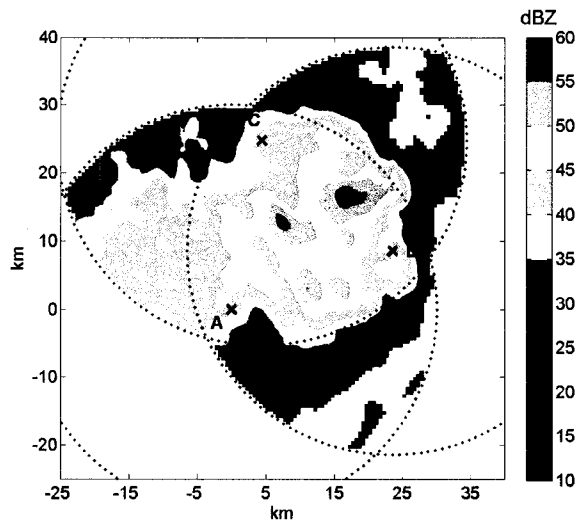

Figure 5.16: Case II: Retrieved reflectivity.

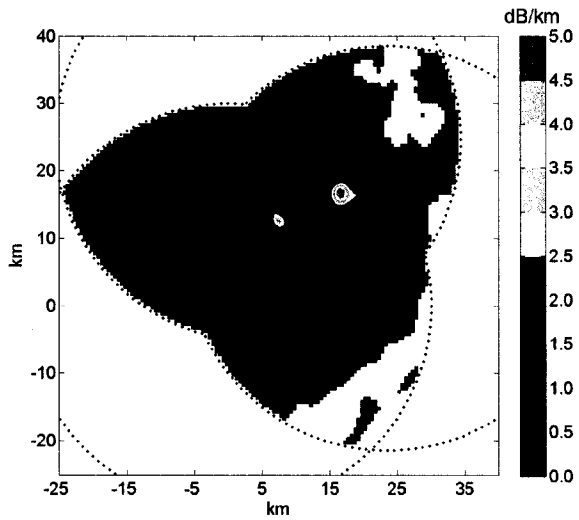

Figure 5.17: Case II: Retrieved specific attenuation.

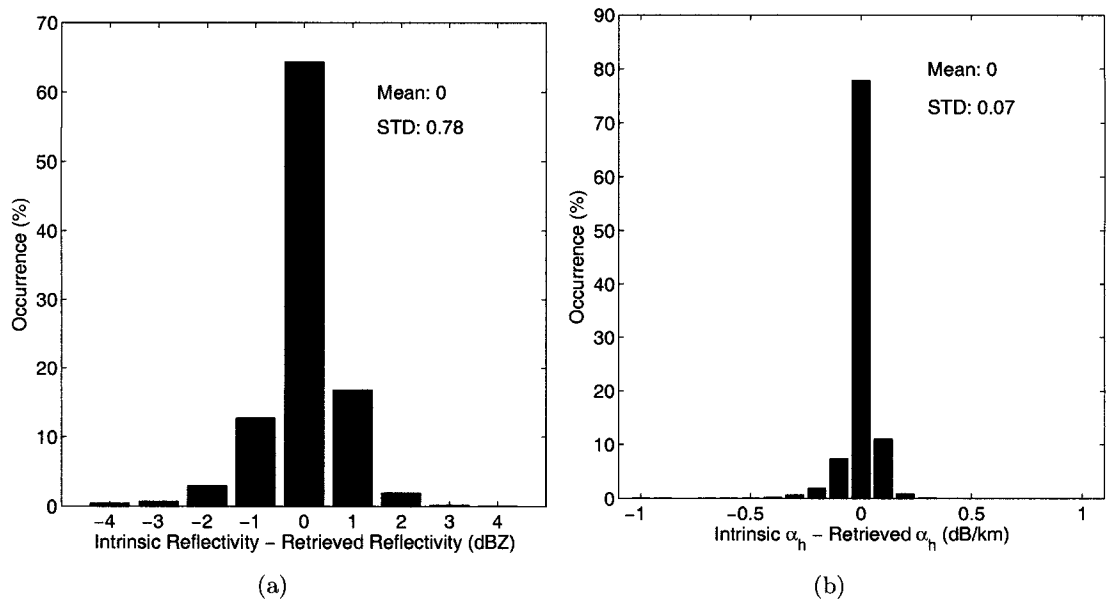

(a) (b)

Figure 5.18: Case II: Distribution of (a) the difference between intrinsic reflectivity and retrieved reflectivity, (b) the difference between intrinsic specific attenuation and retrieved specific attenuation.

5.3.1.3 *Case III: July 23, 2004, 201245-201348 UTC*

Fig. 5.19 shows the intrinsic reflectivity and specific attenuation, while attenuated reflectivities for radars A, B, and C are shown in Fig. 5.20. For comparison of reflectivity retrieval for each radar, intrinsic cumulative attenuation and retrieved cumulative attenuation are shown in Fig. 5.21. Retrieved reflectivity and specific attenuation are shown in Figs. 5.22 and 5.23. For comparison, the distribution of the difference between intrinsic reflectivity and retrieved reflectivity and between intrinsic specific attenuation and retrieved specific attenuation are shown in Fig. 5.24. The standard deviation of the difference between intrinsic reflectivity and retrieved reflectivity is 0.50 dBZ, while the standard deviation of the difference between intrinsic specific attenuation and retrieved specific attenuation is 0.07 dB/km.

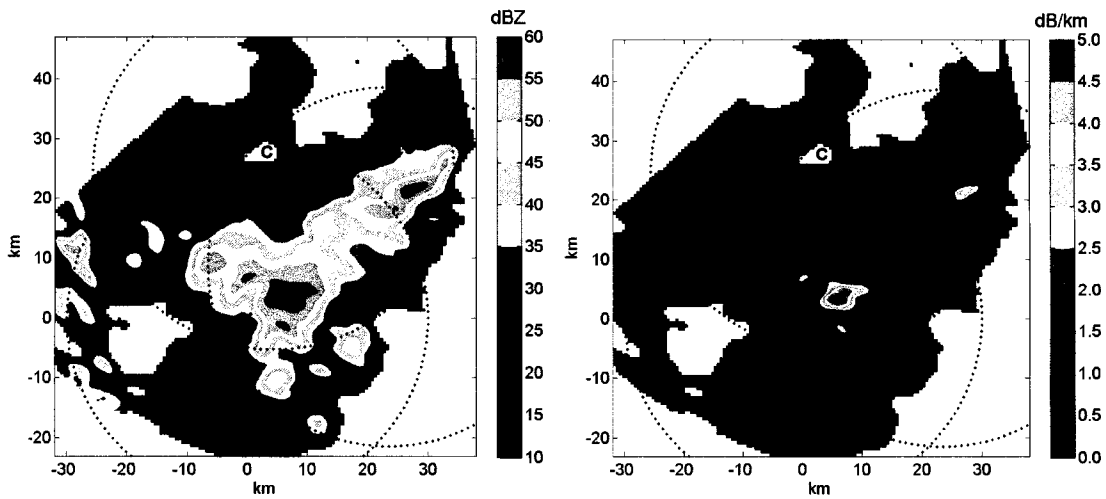

(a) (b)

Figure 5.19: Case III: (a) intrinsic reflectivity and (b) intrinsic specific attenuation at X-band; "x"s indicate the location of radars A, B, and C. The dotted rings are maximum unambiguous range.

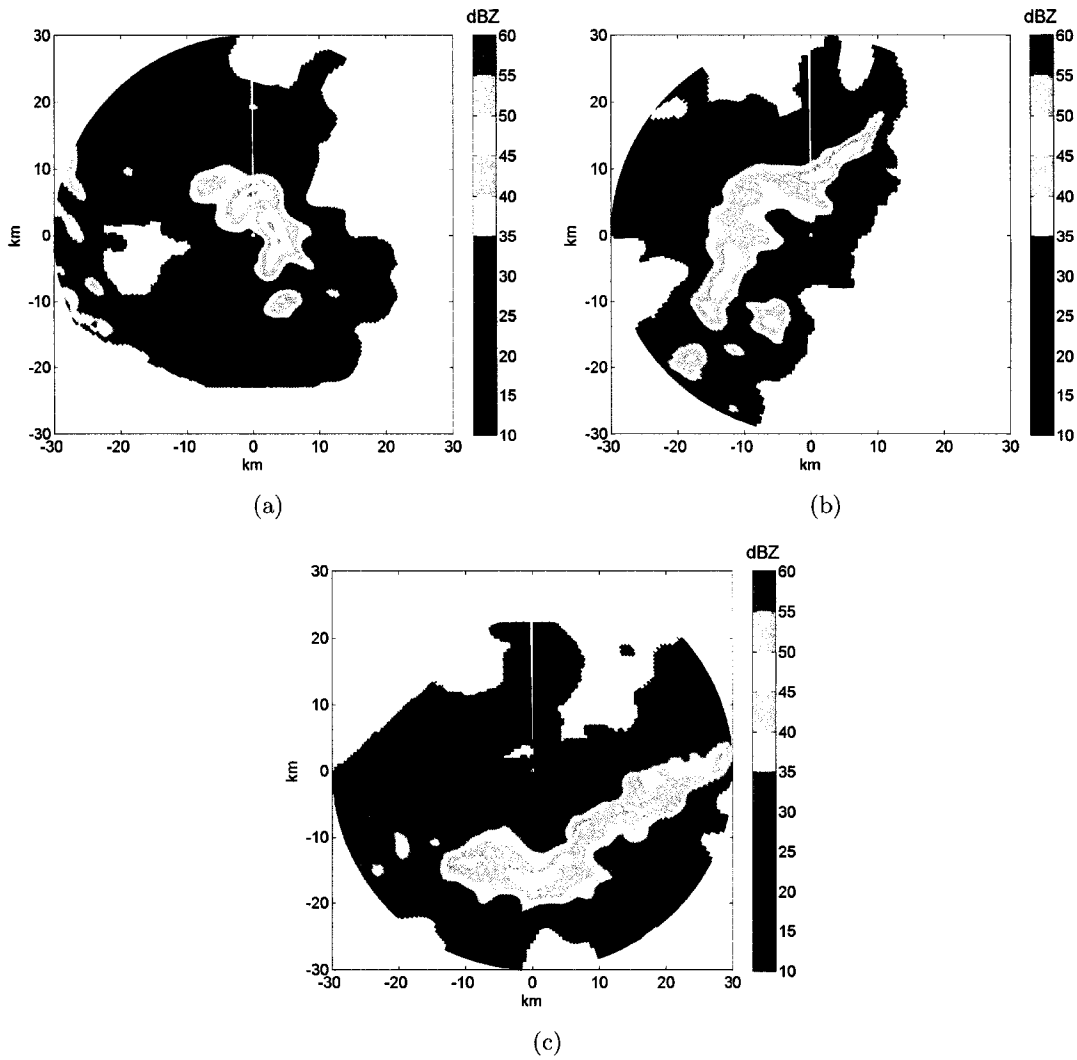

Figure 5.20: Case III: Attenuated reflectivity for radar (a) A, (b) B, and (c) C at X-band.

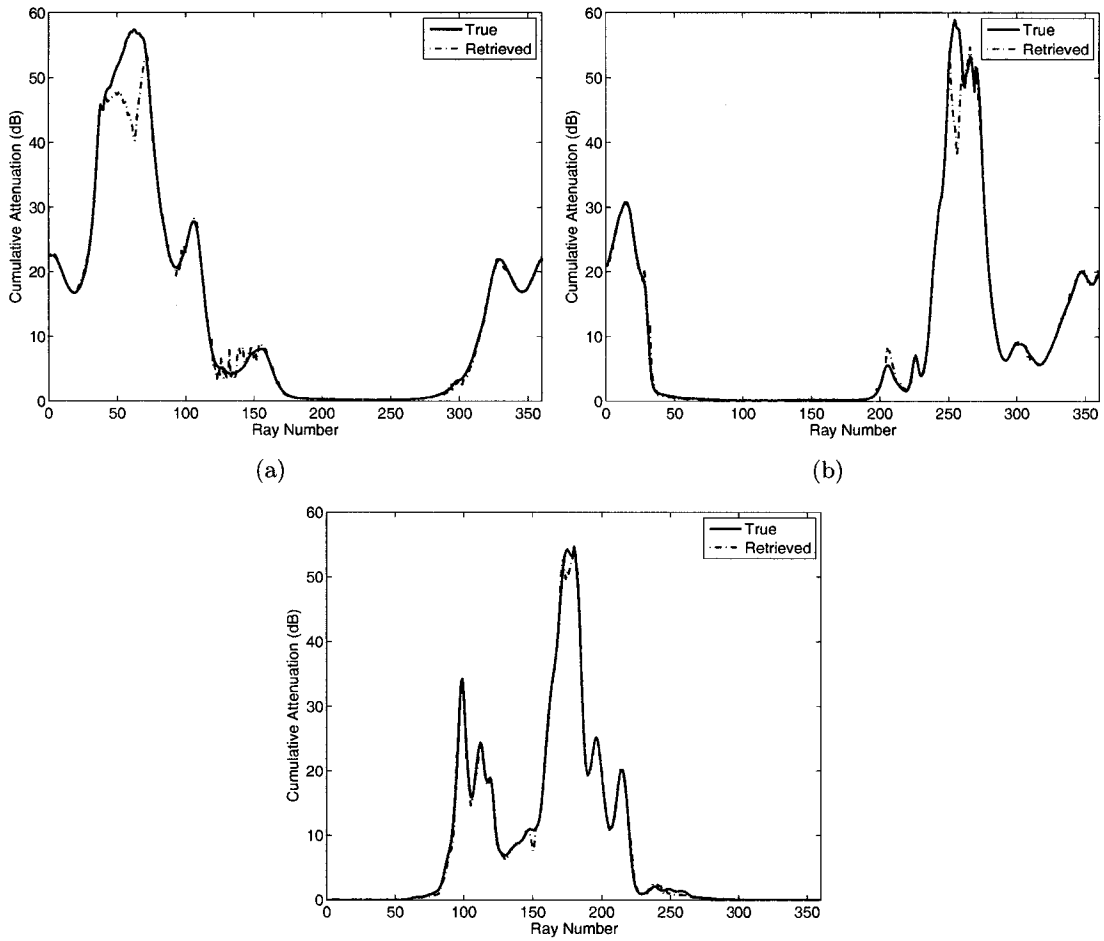

Figure 5.21: Case III: Comparison between intrinsic cumulative attenuation and retrieved cumulative attenuation for radar (a) A, (b) B, and (c) C.

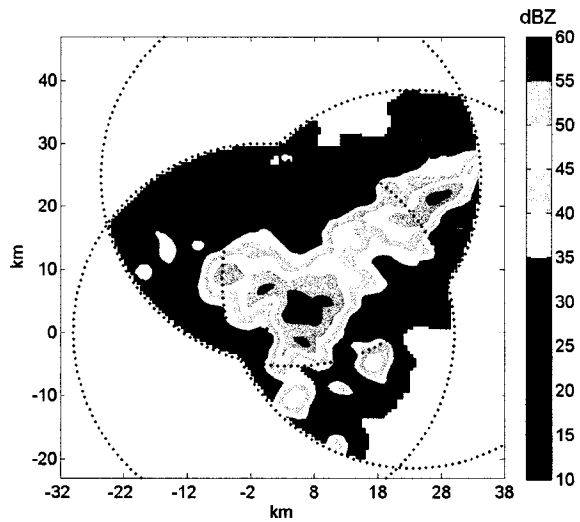

Figure 5.22: Case III: Retrieved reflectivity.

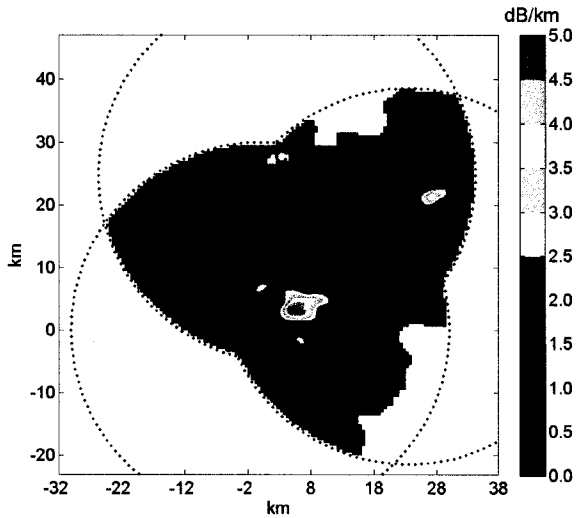

Figure 5.23: Case III: Retrieved specific attenuation.

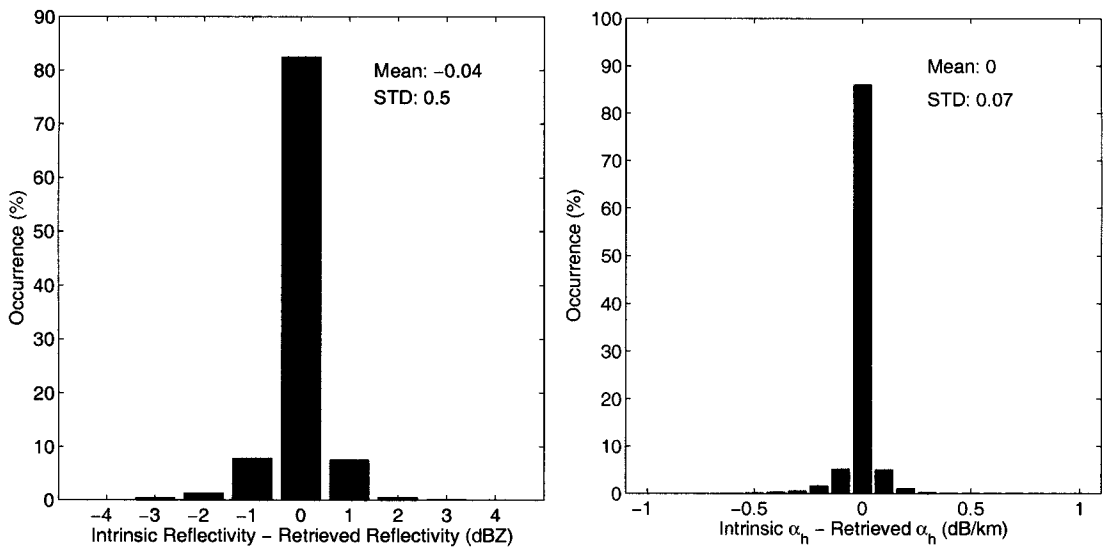

(a) (b)

Figure 5.24: Case III: Distribution of (a) the difference between intrinsic reflectivity and retrieved reflectivity, (b) the difference between intrinsic specific attenuation and retrieved specific attenuation.

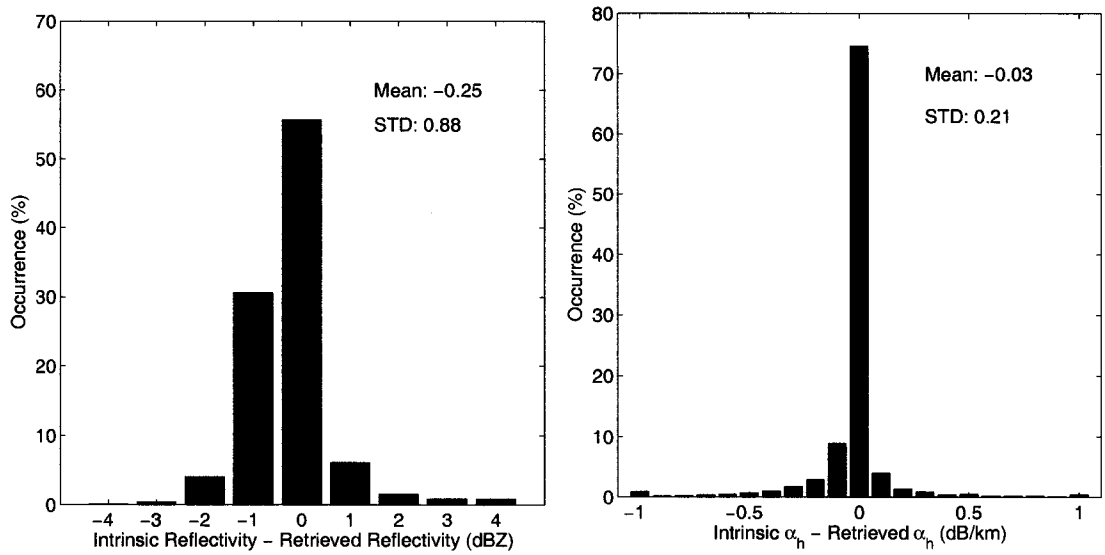

(a) (b)

Figure 5.25: Case I with signal fluctuations: Distribution of (a) the difference between intrinsic reflectivity and retrieved reflectivity and (b) the difference between intrinsic specific attenuation and retrieved specific attenuation. Gaussian random errors are introduced to the measured reflectivity.

5.3.2 Impact of signal fluctuations and bias on the algorithm performance

For the performance evaluation in the presence of signal fluctuation errors, Gaussian random errors with standard deviation of 1 dBZ and zero mean are introduced to the measured reflectivities from each radar for Case I (July 19 2000, 000204-000607 UTC). Fig. 5.25 shows the performance against signal fluctuations for Case I. From the results of Fig. 5.25 we can see that the impact of signal fluctuation on the proposed retrieval algorithm is negligible.

For the performance evaluation in the presence of signal fluctuation errors and system biases, Gaussian random errors and system biases are introduced to the measured reflectivities from each radar for Case I. Various scenarios presented here are supposed to test the performance of the proposed retrieval algorithm with the impact of the system biases. For a scenario of 1 dBZ bias for radar A and no biases for radar B and C, Fig. 5.26 shows the distribution of the difference between intrinsic

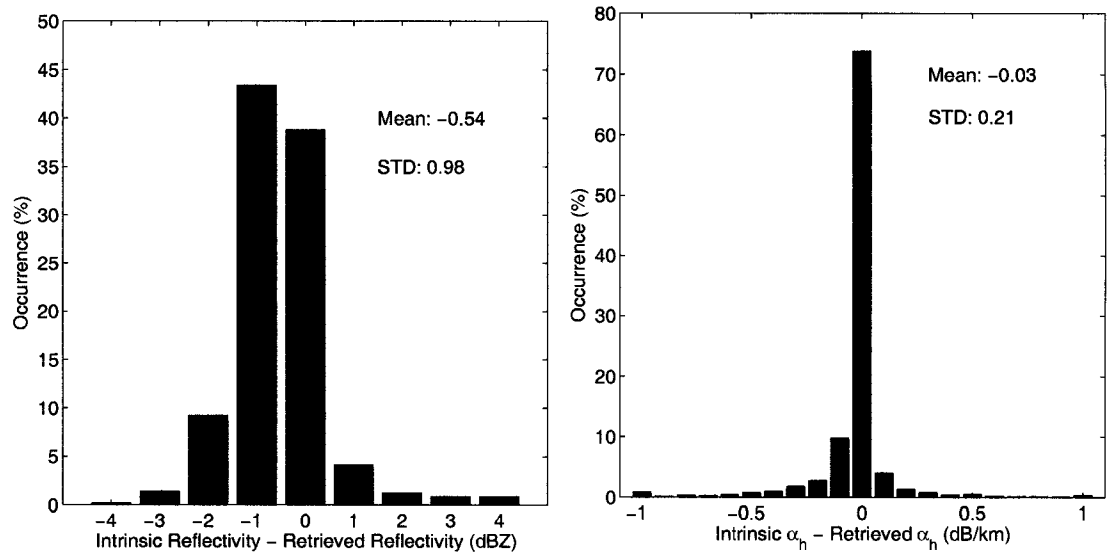

(a) (b)

Figure 5.26: Case I with 1 *dBZ* bias for radar A and no biases for radar B and C: Distribution of (a) the difference between intrinsic reflectivity and retrieved reflectivity and (b) the difference between intrinsic specific attenuation and retrieved specific attenuation. Gaussian random errors are also introduced to the measured reflectivity.

radar observations and retrieved radar observations. The evaluation results for various scenarios of system bias are summarized in Table 5.1. By comparing the results of Table 5.1, we can see that reflectivity retrieval is affected as much as the system bias. However, specific attenuation retrieval is not much affected by system bias.

Table 5.1: Mean bias and standard deviation of the difference between intrinsic radar variables and retrieved radar observations for Case I with introduction of signal fluctuations and system bias.

System Bias (dBZ)			Reflectivity (dBZ)		Specific attenuation (dB/km)	
A	B	C	Bias	STD	Bias	STD
1	0	0	-0.54	0.98	-0.03	0.21
0	1	0	-0.55	1.07	-0.03	0.21
0	0	1	-0.74	0.90	-0.03	0.22
1	1	0	-0.84	1.09	-0.03	0.21
0	1	1	-1.03	0.92	-0.03	0.21
1	0	1	-1.02	0.87	-0.03	0.21
1	1	1	-1.32	0.85	-0.03	0.21
1	1	-1	-0.32	1.45	-0.03	0.22
1	-1	1	-0.71	1.18	-0.03	0.22
-1	1	1	-0.74	1.14	-0.03	0.22
0	-1	-1	0.55	0.97	-0.02	0.21
-1	-1	-1	0.81	0.88	-0.02	0.21

5.4 Summary and Discussion

A new retrieval technique for reflectivity and specific attenuation estimates for a networked radar environment has been presented. The proposed retrieval method simultaneously solves the integral equation for three radars with individual constraints on integrated path attenuation. The optimal reflectivity is obtained with respect to each networked radar by iterating to minimize the cost function. In this chapter, for brevity the solution is presented for a three-radar system. However, this method can easily be applied to two or multiple radars. The presented retrieval algorithm was evaluated with three severe convective rain events. The results of evaluation using the simulated data sets without introduction of signal fluctuations and system bias are summarized in Table 5.2. The standard deviation of the difference between intrinsic reflectivity and retrieved reflectivity is less than 1.0 dBZ with negligible bias, whereas the standard deviation of the difference between intrinsic specific attenuation and retrieved specific attenuation is less than 0.2 dB/km. The proposed retrieval algorithm has also been evaluated for signal fluctuations and system bias with various scenarios. The impact of signal fluctuation on the proposed retrieval algorithm is negligible. The retrieved reflectivity is affected as much as the system bias. However, retrieved specific attenuation is not much affected by system bias. The results from the simulations demonstrate good accuracy of the retrieval method for intrinsic reflectivity.

Table 5.2: Mean bias and standard deviation of the difference between intrinsic radar variables and retrieved radar observations using simulated data sets without introduction of signal fluctuations and system bias.

Case	Reflectivity (dBZ)		Specific attenuation (dB/km)	
	Bias	STD	Bias	STD
Case I	-0.20	0.74	-0.01	0.18
Case II	-0.00	0.78	0.0	0.07
Case III	-0.04	0.50	0.0	0.07

CHAPTER 6

SUMMARY AND FUTURE WORK

6.1 Summary

For targeted applications such as coverage over a city or a small basin, higher-frequency radars such as X-band have been drawing attention for lower cost and more precise radar measurements than S-band radars. However, one of problem at frequencies higher than S-band is significant attenuation effects due to precipitation. For quantitative applications of X-band radar systems, the radar measurements need to be properly compensated for attenuation effects. The principal objective of the research is the development of retrieval algorithms for radar observations in an attenuated environment.

In the development phase of a retrieval algorithm for radar observations, it is useful to have simultaneous radar observations with and without the impact of path attenuation. The retrieval algorithm can be evaluated by the simulated data set with and without the impact of path attenuation. The data set for higher frequencies such as X-band can be obtained from dual-polarization S-band radar measurements negligibly attenuated by precipitation. Methodologies to simulate the realistic range profiles of radar variables have been proposed and compared. First, an empirical conversion method was proposed, which is based on a nearly one-to-one relation of the intrinsic radar variables between S- and X-band. Second, a DSD inversion method was proposed that simulates X-band variables using DSD retrieved from S-band radar measurements. Third, a DSD sampling method that lies between the empirical conversion method and the DSD inversion method was proposed. All the three methods for simulating X-band radar observations were evaluated and compared with each other. Based on exhaustive simulation results, it is observed that all three

methods provide consistent data sets. The simulated range profiles at X-band from all three methods lie in the vicinity of the observed S-band radar measurements with acceptable deviations. The simulated data set with "realistic" dual-polarization radar variables at X-band can be used effectively in the algorithm development phase .

The conventional rain profiling algorithm using the profiles of Z_h and ϕ_{dp} retrieves specific attenuation assuming a constant intercept parameter along a propagation path. A dual polarization rain profiling algorithm based on the profiles of Z_h, Z_{dr} and ϕ_{dp} was suggested. By the introduction of Z_{dr} in retrieval procedure, a solution of specific attenuation can be derived without the assumption of constant N_w along a path in the algorithm formulation. The evaluation of the proposed algorithm was performed with X-band radar observations simulated from data observed by the CSU-CHILL radar. The analysis shows that DRPA can retrieve attenuation better than conventional RPA. From the evaluation results, we can see that the DRPA provides better performance about 13-17% of the attenuation corrected data within 1 dB than RPA in all situations. A new self-consistent method corresponding to the DRPA has also been presented. The SC-DRPA can obtain the optimal value of the coefficients γ and κ simultaneously. The coefficients selected by the proposed method can be more reliable than previous techniques because the coefficients are selected simultaneously and δ impact is also considered in the choice of optimal values of γ and κ. The results of the evaluation show the SC-DRPA technique works well in situations of temperature or drop axis ratio variations. The DRPA and SC-DRPA increase the percentage of attenuation corrected data to satisfy observation requirements for all situations.

A new retrieval algorithm for radar observations was proposed with respect to a networked radar environment. The algorithm retrieves the reflectivity and specific attenuation by integral equation derived in terms of measured reflectivity and cumulative attenuation, in a manner similar to that used with a differential phase constraint.

Using the integral equation, the reflectivity at a common volume of the multiple radar can be obtained by a networked radar approach. The proposed algorithm was evaluated extensively with data sets simulated by the empirical conversion method. The results of the evaluation show that the retrieved radar observations agree well with the intrinsic radar observations. The standard deviation of the difference between intrinsic reflectivity and retrieved reflectivity is less than 1.0 dBZ with negligible bias, whereas the standard deviation of the difference between intrinsic specific attenuation and retrieved specific attenuation is less than 0.2 dB/km without bias.

6.2 Suggestions for future work

The fundamental research for the retrieval algorithms in the networked radar environment has been accomplished. For further research, application-level study is needed. This is the evaluation process of the problems that can happen in the field experiment. For the simulation of X-band rainfall observations from S-band radar data, the proposed methodologies can be verified by comparison with dual-frequency radar measurements or observations of X- and S-band radar operating in the same scanning and location. As an alternative approach, the proposed methods can be evaluated by comparing the measurements of CASA X-band radars and the simulated X-band radar variables from observations of S-band dual polarization National Severe Storms Laboratory (NSSL) KOUN radar during IP1A of CASA project. The first generation network node for the first Integrating Project (IP1) will be deployed in Oklahoma with four sensing nodes. The location of CASA X-band radars and KOUN radar are shown in Fig. 6.1. DRPA and SC-DRPA can be evaluated by comparing the retrieved radar observations for CASA radar and the measurements of KOUN radar. Reflectivity retrieval algorithm in the networked radar systems can also be evaluated by comparing the retrieved radar observations for CASA radar and the measurements of KOUN radar.

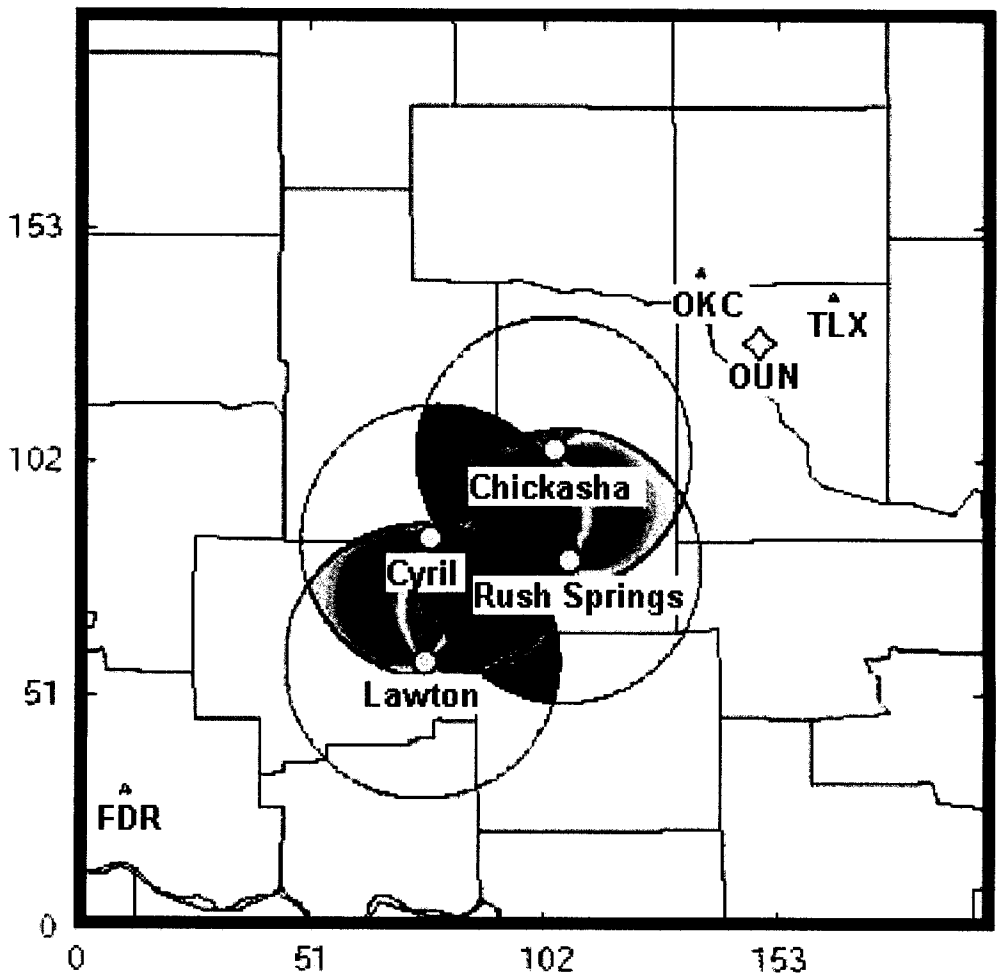

Figure 6.1: Configuration of the IP1 test bed. Four sensing nodes of CASA IP1A will be deployed at Chickasha, Lawton, Rush Springs and Cyril, Oklahoma. The KOUN radar is located in OUN.

APPENDIX A

DERIVATION FOR DRPA

First, the derivation of $\alpha_h(r)$ is presented. The derivation procedure for specific attenuation at horizontal polarization is based on four parameterizations described in (4.9)-(4.12). By imposing (4.12) on (4.9), we can obtain an expression as

$$\begin{aligned}
\alpha_h(r) &= a_1 \frac{[Z'_h(r)]^{b_1}[Z'_{dr}(r)]^{c_1}}{f_h(0;r)f_{dr}(0;r)}; \\
&\left(f_h(0;r) = e^{-0.46b_1\int_0^r \alpha_h(s)ds}; \quad f_{dr}(0;r) = e^{-0.46c_1\int_0^r \alpha_{dp}(s)ds}\right) \\
&= a_1 \frac{[Z'_h(r)]^{b_1}}{f_h(r_0;r)f_{dr}(r_0;r)} \frac{[Z'_{dr}(r)]^{c_1}}{f_h(0;r_0)f_{dr}(0;r_0)}; \\
&\left(f_h(0;r) = f_h(0;r_0)f_h(r_0;r); \quad f_{dr}(0;r) = f_{dr}(0;r_0)f_{dr}(r_0;r)\right).
\end{aligned} \tag{A-1}$$

The differential equation of $f_h(r_0;r)f_{dr}(r_0;r)$ with imposition of (4.11) can be derived as

$$\begin{aligned}
&\frac{d}{dr}\{f_h(r_0;r)f_{dr}(r_0;r)\} \\
&= \frac{d}{dr}\left\{-0.46(b_1\int_{r_0}^r \alpha_h(s)ds + c_1\int_{r_0}^r \alpha_{dp}(s)ds)\right\} e^{\left\{-0.46(b_1\int_{r_0}^r \alpha_h(s)ds + c_1\int_{r_0}^r \alpha_{dp}(s)ds)\right\}} \\
&= \{-0.46(b_1\alpha_h(r) + c_1\alpha_{dp}(r))\}\, f_h(r_0;r)f_{dp}(r_0;r) \\
&= -0.46(b_1 + c_1\kappa)\alpha_h(r)f_h(r_0;r)f_{dp}(r_0;r).
\end{aligned} \tag{A-2}$$

By substituting $\alpha_h(r)$ with (A-1), the above equation can be expressed as

$$\frac{d}{dr}\{f_h(r_0;r)f_{dr}(r_0;r)\} = -0.46a_1(b_1 + c_1\kappa)\frac{[Z'_h(r)]^{b_1}[Z'_{dr}(r)]^{c_1}}{f_h(0;r_0)f_{dr}(0;r_0)}. \tag{A-3}$$

After integrating (A-3) from r_0 to r, the equation results in

$$\{f_h(r_0;r)f_{dr}(r_0;r)\} = \{f_h(r_0;r_0)f_{dr}(r_0;r_0)\} - \frac{0.46a_1(b_1+c_1\kappa)}{f_h(0;r_0)f_{dr}(0;r_0)}\int_{r_0}^{r}[Z'_h(r)]^{b_1}[Z'_{dr}(r)]^{c_1}dr$$

$$(\{f_h(r_0;r_0)f_{dr}(r_0;r_0)\} = 1) \tag{A-4}$$

$$= 1 - \frac{0.46a_1(b_1+c_1\kappa)}{f_h(0;r_0)f_{dr}(0;r_0)}\int_{r_0}^{r}[Z'_h(r)]^{b_1}[Z'_{dr}(r)]^{c_1}dr.$$

By substituting (A-4) to (A-1) we can derive an expression as

$$\alpha_h(r) = \frac{a_1[Z'_h(r)]^{b_1}[Z'_{dr}(r)]^{c_1}}{f_h(0;r_0)f_{dr}(0;r_0) - 0.46a_1(b_1+c_1\kappa)\int_{r_0}^{r}[Z'_h(r)]^{b_1}[Z'_{dr}(r)]^{c_1}dr}. \tag{A-5}$$

From (4.12) at $r = r_0$, $f_h(0;r_0)f_{dr}(0;r_0)$ can be rewritten as

$$f_h(0;r_0)f_{dr}(0;r_0) = \frac{[Z'_h(r_0)]^{b_1}[Z'_{dr}(r_0)]^{c_1}}{[Z_h(r_0)]^{b_1}[Z_{dr}(r_0)]^{c_1}}. \tag{A-6}$$

From $\alpha_h(r_0) = a_1[Z_h(r_0)]^{b_1}[Z_{dr}(r_0)]^{c_1}$, the above equation can be rewritten as

$$f_h(0;r_0)f_{dr}(0;r_0) = \frac{a_1[Z'_h(r_0)]^{b_1}[Z'_{dr}(r_0)]^{c_1}}{\alpha_h(r_0)}. \tag{A-7}$$

From (A-5) and (A-7), an expression of $\alpha_h(r)$ is derived as (note that coefficient a is dropped)

$$\alpha_h(r) = \frac{\alpha_h(r_0)[Z'_h(r)]^{b_1}[Z'_{dr}(r)]^{c_1}}{[Z'_h(r_0)]^{b_1}[Z'_{dr}(r_0)]^{c_1} - \alpha_h(r_0)0.46(b_1+c_1\kappa)\int_{r_0}^{r}[Z'_h(r)]^{b_1}[Z'_{dr}(r)]^{c_1}dr}. \tag{A-8}$$

The second part of derivation of $\alpha_h(r)$ constrains the reference value of $\alpha_h(r_0)$ based on the measured differential propagation phase. To obtain $\alpha_h(r_0)$, start from (4.10) and integrate from r_0 to r_m as

$$\int_{r_0}^{r_m}\alpha_h(s)ds = \gamma\int_{r_0}^{r_m}K_{dp}(s)ds = \frac{\gamma}{2}\Delta\phi_{dp}(r_0;r_m);$$

$$\Delta\phi_{dp}(r_0;r_m) = \phi_{dp}(r_m) - \phi_{dp}(r_0). \tag{A-9}$$

By integrating (A-2) from r_0 to r_m with respect to $\alpha_h(r)$, we can obtain an equation as

$$\int_{r_0}^{r_m} \alpha_h(s)ds = \frac{-1}{0.46(b_1 + c_1\kappa)}\{ln(f_h(r_0;r_m)f_{dr}(r_0;r_m)) - ln(f_h(r_0;r_0)f_{dr}(r_0;r_0))\}$$
$$(ln(f_h(r_0;r_0)f_{dr}(r_0;r_0)) = 0) \tag{A-10}$$
$$= \frac{-1}{0.46(b_1 + c_1\kappa)}\{ln(f_h(r_0;r_m)f_{dr}(r_0;r_m))\}.$$

From (A-9) and (A-10), we can obtain an equation as

$$\begin{aligned} f_h(r_0;r_m)f_{dr}(r_0;r_m) &= e^{-0.23\gamma(b_1+c_1\kappa)\Delta\phi_{dp}(r_0;r_m)} \\ &= 10^{-0.1\gamma(b_1+c_1\kappa)\Delta\phi_{dp}(r_0;r_m)}. \end{aligned} \tag{A-11}$$

By combining (A-4), (A-7) and (A-11) at $r = r_m$, we can derive an equation as

$$\alpha_h(r_0) = \frac{[Z'_h(r_0)]^{b_1}[Z'_{dr}(r_0)]^{c_1}}{0.46(b_1 + c_1\kappa)\int_{r_0}^{r_m}[Z'_h(r)]^{b_1}[Z'_{dr}(r)]^{c_1}dr}(1-10^{-0.1\gamma(b_1+c_1\kappa)\Delta\phi_{dp}(r_0;r_m)}). \tag{A-12}$$

Finally, by synthesizing (A-8), (A-12) and $I(r_0;r) = I(r_0;r_m) - I(r;r_m)$, a solution of $\alpha_h(r)$ can be expressed as

$$\begin{aligned} \alpha_h(r) &= \frac{[Z'_h(r)]^{b_1}[Z'_{dr}(r)]^{c_1}(10^{0.1\gamma(b_1+c_1\kappa)\Delta\phi_{dp}(r_0;r_m)} - 1)}{I_h(r_0;r_m) + (10^{0.1\gamma(b_1+c_1\kappa)\Delta\phi_{dp}(r_0;r_m)} - 1)I_h(r;r_m)} \\ I_h(r_0;r_m) &= 0.46(b_1 + \kappa c_1)\int_{r_0}^{r_m}[Z'_h(r)]^{b_1}[Z'_{dr}(r)]^{c_1}dr. \end{aligned} \tag{A-13}$$

A solution for $\alpha_v(r)$ can be derived similarly as the derivation of $\alpha_h(r)$. By imposing (4.11) on (4.15), the relation of $\alpha_v(r)$ and $\alpha_h(r)$ can be obtained as

$$\alpha_v(r) = (1 - \kappa)\alpha_h(r). \tag{A-14}$$

Using (4.10) and (A-14), the relationship of $\alpha_v(r)$ and $K_{dp}(r)$ can expressed as

$$\alpha_v(r) = \gamma(1 - \kappa)K_{dp}(r). \tag{A-15}$$

We can also obtain the relation of $\alpha_v(r)$ and $\alpha_{dp}(r)$ by imposing (A-14) on (4.11). The relation can be written as

$$\alpha_{dp}(r) = \frac{\kappa}{1-\kappa}\alpha_v(r). \tag{A-16}$$

Following the similar procedure of the solution for $\alpha_h(r)$ with (A-15)- (A-16) and (4.12)-(4.13), a solution of $\alpha_v(r)$ can be obtained as

$$\begin{aligned} \alpha_v(r) &= \frac{[Z'_v(r)]^{b_2}[Z'_{dr}(r)]^{c_2}(10^{0.1\gamma(1-\kappa)(b_2+\frac{\kappa}{1-\kappa}c_2)\Delta\phi_{dp}(r_0;r_m)}-1)}{I_v(r_0;r_m)+(10^{0.1\gamma(1-\kappa)(b_2+\frac{\kappa}{1-\kappa}c_2)\Delta\phi_{dp}(r_0;r_m)}-1)I_v(r;r_m)}; \\ I_v(r_0;r_m) &= 0.46(b_2+\frac{\kappa}{1-\kappa}c_2)\int_{r_0}^{r_m}[Z'_v(r)]^{b_2}[Z'_{dr}(r)]^{c_2}dr. \end{aligned} \tag{A-17}$$

APPENDIX B

DERIVATION FOR RPA USING CUMULATIVE ATTENUATION

The derivation procedure for specific attenuation is based on two parameterizations described in (5.1)-(5.3). By imposing (5.2) on (5.1), we can obtain an expression as

$$\begin{aligned}\alpha_h(r) &= \frac{a[Z'_h(r)]^b}{f_h(0;r)}; \quad (f_h(0;r) = e^{-0.46b\int_0^r \alpha_h(s)ds}); \\ &= \frac{a[Z'_h(r)]^b}{f_h(0;r_0)f_h(r_0;r)}; \quad (f_h(0;r) = f_h(0;r_0)f_h(r_0;r)).\end{aligned} \tag{B-1}$$

The differential equation of $f_h(r_0;r)$ can be derived as

$$\begin{aligned}\frac{d}{dr}\{f_h(r_0;r)\} &= \frac{d}{dr}\left\{-0.46b\int_{r_0}^r \alpha_h(s)ds\right\} e^{\left\{-0.46b\int_{r_0}^r \alpha_h(s)ds\right\}} \\ &= -0.46b\alpha_h(r)f_h(r_0;r).\end{aligned} \tag{B-2}$$

By substituting $\alpha_h(r)$ with (B-1), the above equation can be expressed as

$$\frac{d}{dr}\{f_h(r_0;r)\} = -0.46ab\frac{[Z'_h(r)]^b}{f_h(0;r_0)}. \tag{B-3}$$

After integrating of (B-3) from r_0 to r, the equation results in

$$\begin{aligned}\{f_h(r_0;r)\} &= \{f_h(r_0;r_0)\} - \frac{0.46ab}{f_h(0;r_0)}\int_{r_0}^r [Z'_h(r)]^b dr \\ &(\{f_h(r_0;r_0)\} = 1) \\ &= 1 - \frac{0.46ab}{f_h(0;r_0)}\int_{r_0}^r [Z'_h(r)]^b dr.\end{aligned} \tag{B-4}$$

By substituting (B-4) to (B-1) we can derive an expression as

$$\alpha_h(r) = \frac{a[Z'_h(r)]^b}{f_h(0;r_0) - 0.46ab\int_{r_0}^{r}[Z'_h(r)]^b dr}. \tag{B-5}$$

From (5.2) at $r = r_0$, $f_h(0;r_0)$ can be rewritten as

$$f_h(0;r_0) = \frac{[Z'_h(r_0)]^b}{[Z_h(r_0)]^b}. \tag{B-6}$$

From $\alpha_h(r_0) = a[Z_h(r_0)]^b$, the above equation can be rewritten as

$$f_h(0;r_0) = \frac{a[Z'_h(r_0)]^b}{\alpha_h(r_0)}. \tag{B-7}$$

From (B-5) and (B-7), an expression of $\alpha_h(r)$ is derived as (note that coefficient a is dropped)

$$\alpha_h(r) = \frac{\alpha_h(r_0)[Z'_h(r)]^b}{[Z'_h(r_0)]^b - \alpha_h(r_0)0.46b\int_{r_0}^{r}[Z'_h(r)]^b dr}. \tag{B-8}$$

The second part of derivation of $\alpha_h(r)$ constrains the reference value of $\alpha_h(r_0)$ based on the measured differential propagation phase. To obtain $\alpha_h(r_0)$, start from (5.3)

$$2\int_{r_0}^{r}\alpha_h(s)ds = 10log_{10}(Z_h(r)) - 10log_{10}(Z'_h(r)) = \Delta Z(r_m). \tag{B-9}$$

By integrating (B-2) from r_0 to r_m with respect to $\alpha_h(r)$, we can obtain an equation as

$$\begin{aligned}\int_{r_0}^{r_m}\alpha_h(s)ds &= \frac{-1}{0.46b}\{ln(f_h(r_0;r_m)) - ln(f_h(r_0;r_0))\} \\ &(ln(f_h(r_0;r_0)) = 0) \\ &= \frac{-1}{0.46b}\{ln(f_h(r_0;r_m))\}.\end{aligned} \tag{B-10}$$

From (B-9) and (B-10), we can obtain an equation as

$$\begin{aligned} f_h(r_0; r_m) &= e^{-0.23b\Delta Z(r_m)} \\ &= 10^{-0.1b\Delta Z(r_m)}. \end{aligned} \tag{B-11}$$

By combining (B-4), (B-7) and (B-11) at $r = r_m$, we can derive an equation as

$$\alpha_h(r_0) = \frac{[Z_h'(r_0)]^b}{0.46b \int_{r_0}^{r_m} [Z_h'(r)]^b dr}(1 - 10^{-0.1b\Delta Z(r_m)}). \tag{B-12}$$

Finally, by synthesizing (B-8), (B-12) and $I(r_0; r) = I(r_0; r_m) - I(r; r_m)$, a solution of $\alpha_h(r)$ can be expressed as

$$\begin{aligned} &\Delta Z(r_m) = 10log_{10}(Z_h(r_m)) - 10log_{10}(Z_h'(r_m)); \\ &\hat{\alpha}_h(r) = \frac{[Z_h'(r)]^b(10^{0.1b\Delta Z(r_m)} - 1)}{I(r_0; r_m) + (10^{0.1b\Delta Z(r_m)} - 1)I(r; r_m)}; \\ &I(r_0; r_m) = 0.46b \int_{r_0}^{r_m} [Z_h'(s)]^b ds. \end{aligned} \tag{B-13}$$

Bibliography

Anagnostou, E. N., M. N. Anagnostou, W. F. Krajewski, A. Kruger, and B. J. Miriovsky, 2004: High-resolution rainfall estimation from X-band polarimetric radar measurements. *J. Hydrometeor.*, **5**, 110–128.

Andsager, K., K. V. Beard, and N. F. Laird, 1999: Laboratory measurements of axis ratios for large raindrops. *J. Atmos. Sci.*, **56**, 2673–2683.

Aydin, K., Y. Zhao, and T. A. Seliga, 1989: Rain-induced attenuation effects on C-band dual-polarization meteorological radar. *IEEE Trans. Geosci. Remote Sensing*, **27**, 57–66.

Beard, K. V. and C. Chuang, 1987: A new model for the equilibrium shape of raindrops. *J. Atmos. Sci.*, **44**, 1509–1524.

Bringi, V. N. and V. Chandrasekar, 2001: *Polarimetric doppler weather radar: Principles and applications*. Cambridge University Press, New York, NY.

Bringi, V. N., V. Chandrasekar, N. Balakrishnan, and D. S. Zrnić, 1990: An examination of propagation effects in rainfall on radar measurements at microwave frequencies. *J. Atmos. Oceanic Technol.*, **7**, 829–840.

Bringi, V. N., V. Chandrasekar, J. Hubbert, E. Gorgucci, W. L. Randeu, and M. Schoenhuber, 2003: Raindrop size distribution in different climatic regimes from disdrometer and dual-polarized radar analysis. *J. Atmos. Sci.*, **60**, 354–365.

Bringi, V. N., G. J. Huang, V. Chandrasekar, and E. Gorgucci, 2002: A methodology for estimating the parameters of a gamma raindrop size distribution model from polarimetric radar data: Application to a squall-line event from the TRMM/Brazil campaign. *J. Atmos. Oceanic Technol.*, **19**, 633–645.

Bringi, V. N., T. D. Keenan, and V. Chandrasekar, 2001: Correcting C-band radar reflectivity and differential reflectivity data for rain atenuation: A self-consistent method with constraints. *IEEE Trans. Geosci. Remote Sensing*, **39**, 1906–1915.

Carey, L. D., S. A. Rutledge, D. A. Ahijevych, and T. D. Keenan, 2000: Correcting propagation effects in C-band polarimetric radar observations of tropical convection using differential propagation phase. *J. Appl. Meteor.*, **39**, 1405–1433.

Chandrasekar, V., H. Fukatsu, and K. Mubarak, 2003: Global mapping of attenuation at Ku- and Ka-band. *IEEE Trans. Geosci. Remote Sensing*, **41**, 2166–2176.

Chandrasekar, V., E. Gorgucci, and L. Baldini, 2002: Evaluation of polarimetric radar rainfall algorithms at X-band. *Proceedings. ERAD 2002*, 277–281.

Chandrasekar, V., E. Gorgucci, S. Lim, and L. Baldini, 2004a: Simulation of X-band radar observation of precipitation from S-band measurements. *Proceedings. IGARSS 2004*, Anchorage, Alaska.

Chandrasekar, V. and A. P. Jayasumana, 2001: Radar design and management in a networked environment. *Proceedings. ITCOMM*, 142–147.

Chandrasekar, V., S. Lim, N. Bharadwaj, W. Li, D. McLaughlin, V. N. Bringi, and E. Gorgucci, 2004b: Principles of networked weather radar operation at attenuating frequencies. *Proceedings. ERAD 2004*, 109–114.

Chandrasekar, V., S. Lim, and G. Gorgucci, 2006: Simulation of X-band rainfall observations from S-band radar data. *J. Atmos. Oceanic Technol.*, in press.

Delrieu, G., H. Andrieu, and J. D. Creutin, 2000: Quantification of path integrated attenuation for X and C-band weather radar systems operating in Mediterranean heavy rainfall. *J. Appl. Meteor.*, **39**, 840–850.

Delrieu, G., S. Caoudal, and J. D. Creutin, 1997: Feasibility of using mountain return for the correction of ground-based X-band weather radar. *J. Atmos. Oceanic Technol.*, **14**, 368–385.

Doviak, R. J. and D. S. Zrnić, 1993: *Doppler radar and weather observations*. Academic Press, San Diego, CA, 2nd edition.

Gorgucci, E., V. Chandrasekar, V. Bringi, and G. Scarchilli, 2002: Estimation of raindrop size distribution parameters from polarimetric radar measurements. *J. Atmos. Sci.*, **59**, 2373–2384.

Gorgucci, E., G. Scarchilli, and V. Chandrasekar, 1996: Error structure of radar rainfall measurement at C-band frequencies with dual-polarization algorithm for attenuation correction. *J. Geophys. Res.*, **101**, 26461–26471.

Gorgucci, E., G. Scarchilli, and V. Chandrasekar, 2000: Practical aspects of radar rainfall estimation using specific differential propagation phase. *J. Appl. Meteor.*, **39**, 945–955.

Hildebrand, P. H., 1978: Iterative correction for attenuation of 5 cm radar in rain. *J. Appl. Meteor.*, **17**, 508–514.

Hitschfeld, W. and J. Bordan, 1954: Errors inherent in the radar measurement of rainfall at attenuating wavelengths. *J. Meteor.*, **11**, 58–67.

Hubbert, J. and V. N. Bringi, 1995: An iterative filtering technique for the analysis of copolar differential phase and dual-frequency radar measurements. *J. Atmos. Oceanic Technol.*, **12**, 643–648.

Jameson, A. R., 1992: The effect of temperature on attenuation correction schemes in rain using polariztion propagation differential phase shift. *J. Appl. Meteor.*, **11**, 1106–1118.

Lim, S. and V. Chandrasekar, 2006: A dual-polarization rain profiling algorithm. *IEEE Trans. Geosci. Remote Sensing*, **44**, 1011–1021.

Lim, S., V. Chandrasekar, and D. McLaughlin, 2004: Retrieval of reflectivity in a networked radar environment. *Proceedings. IGARSS 2004*, Anchorage, Alaska.

Marzoug, M. and P. Amayenc, 1994: A class of single- and dual-frequency algorithms for rain-rate profiling from spaceborne radar. *J. Atmos. Oceanic Technol.*, **11**, 1480–1506.

Matrosov, S. Y., D. E. Kingsmill, B. E. Martner, and F. M. Ralph, 2005: The utility of X-band polarimetric radar for quantitative estimates of rainfall parameters. *J. Hydrometeor.*, **6**, 248–262.

McLaughlin, D., 2001: *Presentation to "Weather radar technology-beyond NEXRAD"*. National Academy Press, Washington D.C.

Meneghini, R. and K. Nakamura, 1990: Range profiling of the rain rate by an airborne weather radar. *Remot. Sens. Environ.*, **31**, 193–209.

Park, S. G., V. N. Bringi, V. Chandrasekar, M. Maki, and K. Iwanami, 2005a: Correction of radar reflectivity and differential reflectivity for rain attenuation at X-band. Part I: Theoretical and empirical basis. *J. Atmos. Oceanic Technol.*, **22**, 1621–1632.

Park, S. G., M. Maki, K. Iwanami, V. N. Bringi, and V. Chandrasekar, 2005b: Correction of radar reflectivity and differential reflectivity for rain attenuation at X-band. Part II: Evaluation and application. *J. Atmos. Oceanic Technol.*, **22**, 1633–1655.

Pruppacher, H. R. and K. V. Beard, 1970: A wind tunnel investigation of the internal circulation and shape of water drops falling at terminal velocity in air. *Quart. J. Roy. Meteor. Soc.*, **96**, 247–256.

Scarchilli, G., E. Gorgucci, V. Chandrasekar, and A. Dobaie, 1996: Self-consistency of polarization diversity measurement of rainfall. *IEEE Trans. Geosci. Remote Sensing*, **34**, 22–26.

Sekhon, R. S. and R. C. Srivastava, 1971: Doppler radar observations of drop size distributions in a thunderstorm. *J. Atmos. Sci.*, **28**, 983–994.

Seliga, T. A. and V. N. Bringi, 1976: Potential use of the radar reflectivity at orthogonal polarizations for measuring precipitation. *J. Atmos. Meteor.*, **15**, 69–76.

Smyth, T. J. and A. J. Illingworth, 1998: Correction for attenuation of radar reflectivity using polarization data. *Quart. J. Roy. Meteor. Soc.*, **124**, 2393–2415.

Srivastava, R. C. and L. Tian, 1996: Measurement of attenuation by a dual-radar method: Concept and error analysis. *J. Atmos. Oceanic Technol*, **13**, 937–947.

Tan, J., A. R. Holt, A. Hendry, and D. H. O. Bebbington, 1991: Extracting rainfall rates from X-band CDR radar data by using differential propagation phase shift. *J. Atmos. Oceanic Technol.*, **8**, 790–801.

Testud, J., P. Amayenc, and M. Marzoug, 2000: The rain profiling algorithm applied to polarimetric weather radar. *J. Atmos. Oceanic Technol*, **17**, 322–356.

Testud, J., S. Oury, P. Amayenc, and R. A. Black, 2001: The concept of normalized distributions to describe raindrop spectra: A tool for cloud physic and cloud remote sensing. *J. Atmos. Meteor.*, **40**, 1118–1140.

Tian, L. and R. C. Srivastava, 1997: Measurement of attenuation at C-band in a convective storm by a dual-radar method. *J. Atmos. Oceanic Technol*, **14**, 184–196.

Ulbrich, C. W., 1983: Natural variations in the analytical form of the raindrop-size distribution. *J. Climate Appl. Meteor.*, **22**, 1764–1775.

Willis, P. T., 1984: Functional fits to some observed drop size distributions and parameterization of rain. *J. Atmos. Sci.*, **41**, 1648–1661.